Atomic scale modeling of stress and pairing effects on dopant behavior in silicon

Chihak Ahn

A dissertation submitted in partial fulfillment of
the requirements for the degree of

Doctor of Philosophy

University of Washington

2007

Program Authorized to Offer Degree: Physics

University of Washington
Graduate School

This is to certify that I have examined this copy of a doctoral dissertation by

Chihak Ahn

and have found that it is complete and satisfactory in all respects,
and that any and all revisions required by the final
examining committee have been made.

Chair of the Supervisory Committee:

_____

Scott T. Dunham

Reading Committee:

_____

Scott T. Dunham

_____

Marjorie A. Olmstead

_____

John J. Rehr

Date: _____

In presenting this dissertation in partial fulfillment of the requirements for the doctoral degree at the University of Washington, I agree that the Library shall make its copies freely available for inspection. I further agree that extensive copying of this dissertation is allowable only for scholarly purposes, consistent with "fair use" as prescribed in the U.S. Copyright Law. Requests for copying or reproduction of this dissertation may be referred to Proquest Information and Learning, 300 North Zeeb Road, Ann Arbor, MI 48106-1346, 1-800-521-0600, or to the author.

Signature_____

Date_____

University of Washington

Abstract

Atomic scale modeling of stress and pairing effects on dopant behavior in silicon

Chihak Ahn

Chair of the Supervisory Committee:
Professor Scott T. Dunham
Electrical Engineering

Nanoscale Si device technology faces great challenges in many areas. Due to an ever shrinking design window, a better understanding of the detailed physical mechanisms that occur during fabrication is required. In this dissertation, we studied three main topics to find promising techniques beneficial for ultra shallow junction (USJ) formation. First, we studied stress effects on dopant (As, Sb, P, Ga, and In) diffusion and As activation. Using a combination of density functional theory (DFT) and kinetic lattice Monte Carlo (KLMC) simulations, the effects of stress on dopant diffusivity were predicted and compared with previous experiments. Stress effects were the strongest for P, and P diffusion was anisotropic under biaxial stress. As activation was also studied by considering As_mV clusters concentration at the equilibrium state. Due to the small induced strain, As activation is nearly stress independent, consistent with previous experiments. The second topic is co-doping effects. Donor-acceptor (P-Ga, P-In, As-In, As-Ga, and B-Sb) and acceptor-acceptor (B-Ga and B-In) interactions were studied via *ab-initio* calculations. The dopant-dopant interactions were compared with the Coulomb interaction based on the monopole approximation. A significant binding was observed for donor-acceptor pairs and for some acceptor-acceptor pairs. Based on the formation energies of singly- and multiply-bound dopant complexes, we

calculated the dopant pairing coefficients and resulting enhancements in the solubility limit. The P solubility can be enhanced via pairing with In and Ga. To the contrary, it was found that attractive binding between B and In worsens the B activation due to hole localization. The final topic investigated was B diffusion in SiGe and dopant (B, P and As) segregation at the strained-SiGe/Si interface. We disproved the previously suggested B-Ge binding hypothesis and found that local Ge configurations around B cause significant changes in B migration barriers. Combining local Ge effects with global stress effects, we predicted retarded B diffusion in strained SiGe and compared the results with previous experiments. Finally, considering detailed electronic and mechanical properties of strained SiGe, the segregation ratio for various dopants (B, P and As) was calculated and compared with experimental results.

TABLE OF CONTENTS

LIST OF FIGURES

LIST OF TABLES

GLOSSARY

BZ: Brillouin zone.

CI-NEB: Climbing image nudged elastic band.

CMOS: Complementary metal oxide semiconductor.

DFT: Density functional theory.

DOS: Density of states.

EDS: Effective density of states.

EOR: End of range.

GEA: Gradient expansion approximation.

GGA: Generalized gradient approximation.

HF: Hartree-Fock.

HK: Hohenberg-Kohn.

ITRS: International technology roadmap for semiconductors.

KLMC: Kinetic lattice Monte Carlo.

KMC: Kinetic Monte Carlo.

KS: Kohn-Sham.

LDA: Local density approximation.

MBE: Molecular beam epitaxy

MD: Molecular dynamics.

MEP: Minimum energy path.

MOSFET: Metal oxide semiconductor field effect transistor.

NEB: Nudged elastic band.

NMOS: Negative-channel metal oxide semiconductor.

NMR: Nuclear Magnetic Resonance.

PMOS: Positive-channel metal oxide semiconductor.

PP: Pseudo-potential.

PW91: Perdew-Wang GGA functional.

RTA: Rapid thermal anneal.

SIC: Self interaction correction.

ULSI: Ultra large scale integration.

USJ: Ultra shallow junction.

VASP: Vienna *ab-initio* simulation package.

VLSI: Very large scale integration.

ACKNOWLEDGMENTS

I am very happy to recollect how wonderful people contributed to this dissertation and supported my life during my journey towards becoming a Ph.D.

Most of all, I would like to thank my research advisor Scott Dunham. His guidance and constant support made this dissertation possible. I received great benefits from his deep knowledge of and keen insights into VLSI. He always encourages and supports his students in presenting their work at conferences, and also provides a very comfortable research environment. In addition, he sets aside his time for his students even when he is traveling. This made it possible for me to continue my research without distraction during his sabbatical year in Germany. He is a truly great advisor and I have enjoyed being his student.

I also thank all my committee members: Stephen Ellis, John Rehr, Harth Smith, and Marjorie Olmstead. They never gave me a hard time in scheduling my exams. Their comments in my both exams contributed to making this dissertation more readable. And special thanks to reading committee members, John Rehr and Marjorie Olmstead, for careful reading and valuable comments.

My research was funded by Nanotechnology Center and Semiconductor Research Corporation (SRC). Their financial support allowed me to concentrate on my research without any interruption. I am grateful to Intel and AMD for donating computers used for most of the calculations in this dissertation, and the system administrator, Lee Damon, for maintaining very stable computing clusters.

I have to acknowledge Milan Diebel for his kind help at the initial stage of my research. He transfered his knowledge on *ab-initio* simulation techniques to me, and

thus I could easily catch up on basic skills and produce results quickly. He was a very nice officemate as well. Many thanks to Jason Guo and Bart Trzynadlowski, as officemates and collaborators, for having fruitful discussions about our research, especially to Bart Trzynadlowski for correcting grammatical errors and suggesting better expressions in the text of this dissertation. I express my appreciation to all other group members for cooperating to make for a stress-free office environment and commenting on my practice talks: Chen-luen Shih (specially for funny jokes), Fumin Yang (for the music after lunch time and frequent chatting), Zudian Qin, Jakyoung Song, Joochul Yoon, Ohseob Kwon, Phillip Liu, Shiho Iwanaga, Kjersti Kleven, Andrei Kryjevski, Baruch Feldman, and Rui Deng.

There are many other people outside my current lab worthy of my gratitudes. I would like to thank David Cobden, my previous research advisor in my second year, for the special financial support, and previous labmates, Yael Hanein, David Coffey, Cody Young, and Iuliana Radu, for a cheerful environment.

As to everyone else, there were rises and falls in my family during my 6-year Ph.D. We overcame the ups and downs by sharing our life with many others: Hansang Cho, Joochul Yoon, Hyunsik Chang, Minhyung Kim, Yangmo Yoo, Ju Seong Yeom, Myungsub Song, Justin Doh, Kisung Lee, Jaeyong Lee, and their families. They are truly like my family. I won't forget traveling together, having BBQs and dinner parties, and playing tennis. I give my thanks to Sukjin Yoon and Jongwan Lee, my countrymen in physics department, for sharing common interests and being my frequent lunch mates.

Finally, I thank all my family. My wife, Hyojeong, dedicated her life to my education for last 6 years. My lovely son, Eunbyul, has shown great patience with me, and often took care of his little brother, Jiwon, during my writing for the last month. My mother-in-law also gave us great help in our busy time. Jiwon's birth can be a true

blessing to my family through her aid. What I am today, I owe to my mother. She tried her best and never gave up even in her hopeless circumstances. Remembering her life always refreshes me. Finishing this work would not be possible without their support, and they deserve the dedication.

DEDICATION

To my mother,

Okhee,

my wife,

Hyojeong,

and sons,

Eunbyul and Jiwon

Chapter 1
INTRODUCTION

1.1 Background

Remarkably, Moore's law (Transistor density in a VLSI doubles every 18 months) has remained true for more than 40 years (Fig. 1.1). Today, the feature size of metal oxide semiconductor field effect transistor (MOSFET) is well below 100 nm and the gate length is about 35 nm (Table 1.1). Hence, Si technology is the most significant nanotechnology affecting our everyday life. As the device size moves deeper into the nano-scale, many challenging problems arise: gate oxide leakage, high sheet resistance, lithographical limitation, and short channel effects (SCE). In this dissertation, we investigate various approaches to enhance dopant activation and limit junction depth, thus leading to improvement in SCE and series resistance using *ab-initio* calculations and kinetic lattice Monte Carlo (KLMC) simulations.

The SCE occurs when the channel length becomes comparable to source or drain junction depth, and causes a reduction in the number of charge carriers controlled by the gate and threshold voltages, eventually making the gate lose its switching ability. To avoid SCE, an ultra-shallow junction (USJ) with high activation is required. However, there is a trade-off between junction depth X_j and sheet resistance R_s for a given technology as shown in Fig. 1.2. Therefore, new techniques are required to reduce the junction depth without increasing sheet resistance significantly. Currently various technologies such as low energy clustered-dopant implant, rapid thermal process (RTA), stress engineering, and co-doping, are being developed to achieve this goal. In this dissertation, we will focus on stress effects and pairing effects since they are

Table 1.1: The required characteristic device parameters for past, current and future devices from the 2006 *International Technology Roadmap for Semiconductors* [13]

Year	2005	2007	2010	2013
DRAM 1/2 pitch [nm]	80	65	45	32
MPU printed gate length [nm]	54	42	30	21
MPU physical gate length [nm]	32	25	18	13
S/D extension depth [nm]	11	7.5	6.5	N/A
S/D extension sheet resistance [Ω/sq]	653	640	650	N/A

relatively easy to be tackled using *ab-initio* calculations. We use density functional theory (DFT) as an *ab-initio* method.

During the past decade, application areas of DFT have been widely expanded beyond the traditional fields of applications, physics and chemistry, thanks to the rapid growth of computing power. Now typical DFT codes (see Table 2.1) can quickly calculate the energy of tens of atom supercells, and its applications can be found in many other areas: material research [21, 22], bio-science [23], and even geoscience [24]. DFT based stress energy calculations associated with dopant/defect diffusions also became available in this period.

Stress effects on dopant diffusion and activation have been investigated for more than a decade [25, 26, 27, 28, 29, 30, 31, 32]. However, most of the previous works were based on empirical models, and purely theoretical models based on DFT became available only after the methods to find the minimum energy path (MEP) in reactions were matured [33, 34, 35, 36]. Since the climbing image nudged elastic band (CI-NEB) method [36] was successfully implemented in DFT codes, the transition state (i.e., the saddle point in an energy surface) could be found reliably. Then, Diebel first developed the technique to find the induced strain tensor and stiffness tensor from the energy vs. strain curve [12] for various dopant/defect structures, and this technique was used to predict the stress effects on B diffusion and activation [12].

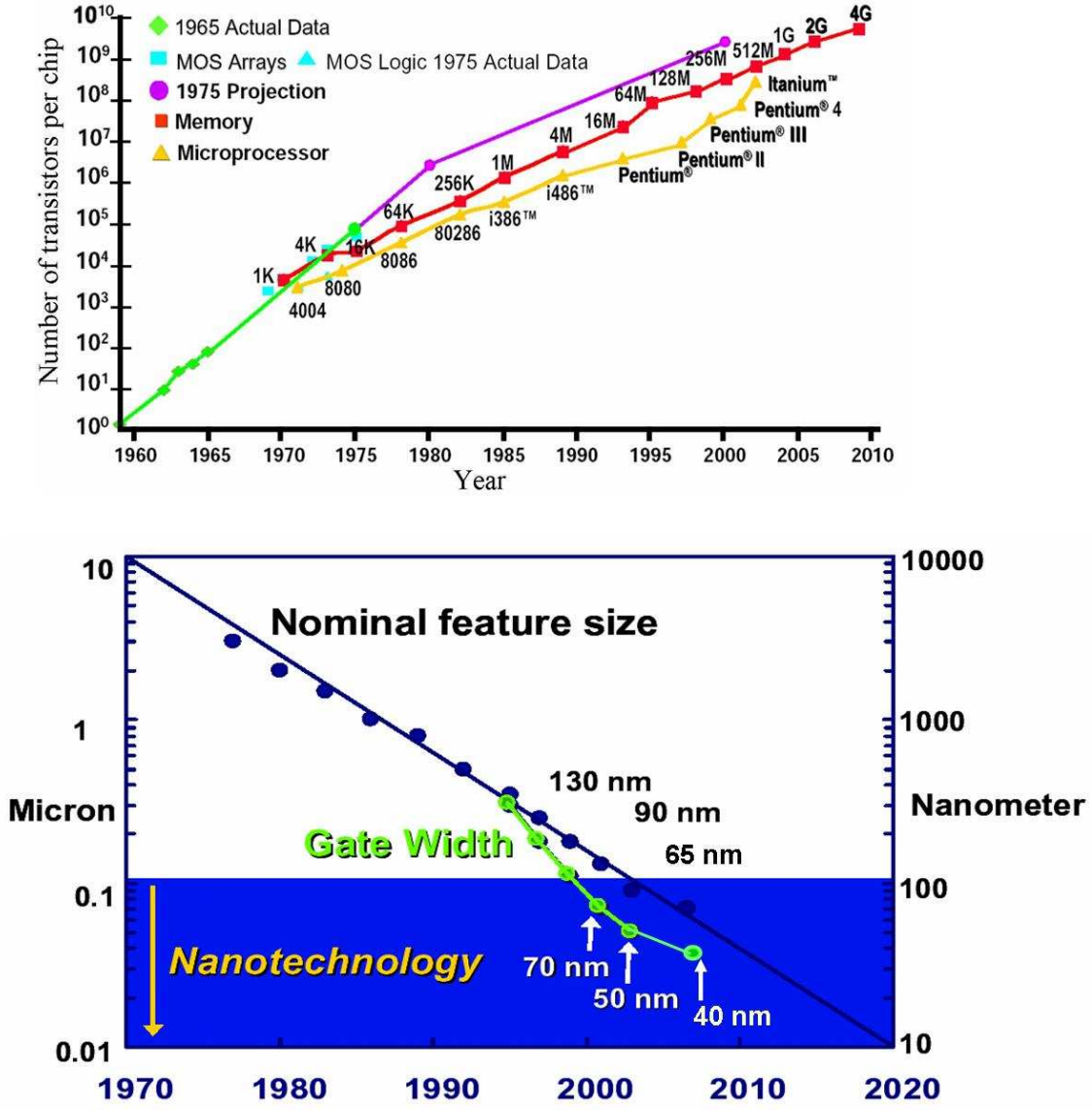

Figure 1.1: Exponential chip density growth in Si technology, also known as Moore's law (top) and nominal feature size of MOSFET (bottom). Source: Gordon Moore's presentation at *International Solid State Circuits Conference* (ISSCC), February 10, 2003

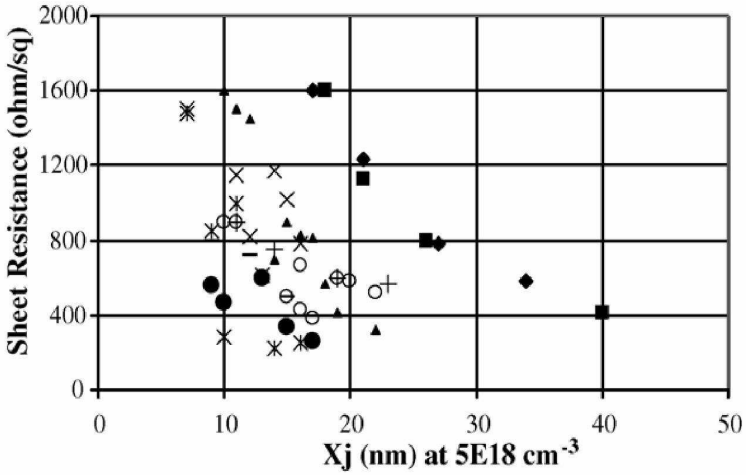

Figure 1.2: Junction depth vs. sheet resistance curve. Different symbols represent different dopant or technology. Legends are omitted for better visibility. Source: Foggiato *et al.* [1]

We apply the technique to many other dopants (P, As, Sb, Ga, and In), and extend it to understand other effects (e.g., local Ge effects on B diffusion). These results can be employed to improve the predictability of modern process simulators such as Sentaurus [37]. Parameter fitting techniques with continuum models can not provide satisfactory descriptions for the dopant/defect behavior in Si lattice any more as the device size approaches the fundamental physical limit.

1.2 Chapter organization

Chapter 2 gives a general overview of the methodology used in this work. Basic principles of DFT, general stress energy model, and kinetic lattice Monte Carlo (KLMC) methods are explained. Determining the induced strain ($\Delta\vec{\epsilon}$), the key factor in studying stress effects, is also explained in Chapter 2.

There are three main topics in this dissertation and the first one is stress effects. Stress effects on dopant diffusion and activation are presented in Chapters 3 and 4.

Stress effects become more important in modern ULSI technology, since they can be employed to improve various material properties. Uniaxial stress has been employed in MOSFET devices since the 90 nm node technology to improve carrier mobility [38]. Anisotropic stress reduces inter-band scattering by lowering the degeneracy of 6-fold conduction band minima and 3-fold valence band maxima and can also reduce the conductivity effective mass of charge carriers in the transport direction (especially for holes), which in turn results in higher carrier mobility. In addition, properly applied stress can suppress dopant diffusion [39] and enhance activation [40]. Therefore, understanding stress effects can provide more room for further MOSFET scaling. Based on the methods addressed in Chapter 2, stress effects on dopant (P, As, Sb, Ga, and In) diffusivity are discussed in Chapter 3 and stress effects on As activation are presented in Chapter 4. When the induced strain at the transition state is asymmetric, KLMC simulations are performed to predict stress effects on dopants diffusivity.

The second topic is pairing effects. Pairing effects between co-dopants can be utilized to achieve USJ with a high active dopant concentration. In modern ULSI technology, heavily co-doped regions frequently occur, and it is observed that counter-doping can be beneficial for reducing junction depth [41, 42, 43]. In addition to strain compensation between large and small atoms, strong binding energy may be beneficial for increasing the dopant solubility limit via multiple binding. Chapter 5 answers this question and also explores the possibility of benefits from pairing effects between similar dopants.

The last topic is dopant diffusion and segregation in SiGe. SiGe can be used as a stress source and affect dopant redistribution during processing because the 4% lattice constant mismatch between Si and Ge can produce substantial stress and change band structure significantly in epitaxially grown $Si_{1-x}Ge_x$ layers [44]. Retarded B diffusion in strained SiGe has been reported by many authors [45, 46, 10, 9]. However, there is no consensus on an explanation of this phenomena. Kuo *et al.* concluded that strain effects are not significant [45] and others found that B-Ge binding is insignificant as

well [47]. We suggest an explanation for retarded B diffusion via DFT in Chapter 6. In Chapter 7, another important phenomena, dopant segregation at the interface of Si/strained-$Si_{1-x}Ge_x$, is discussed. We investigate detailed $Si_{1-x}Ge_x$ band structure and elastic properties. Based on these results, the segregation ratio is predicted as a function of Ge fraction, and the theoretical prediction is compared with experimental observations.

The final chapter summarizes this dissertation and suggests future directions of research.

Chapter 2

METHODS

As the size of ULSI devices reaches the sub-100 nm regime, there has been increasing demand for process modeling based on fundamental physical mechanisms, and a lot of effort has been made to satisfy these demands in conventional continuum process simulators. *Ab-initio* methods have played a critical role in these efforts and achieved great success in finding physical mechanisms of dopant diffusion and deactivation. As the foundation of the modeling hierarchy [12], *ab-initio* calculations provide fundamental parameters such as defect formation energies, dopant migration energy barriers, and volume expansion coefficients due to dopant/defect. However, due to the lack of computing power currently available, there are limitations on the feasibility of using *ab-initio* and molecular dynamics (MD) techniques to simulate atomic transition processes on a practical time scale. Kinetic Monte Carlo (KMC) and kinetic lattice Monte Carlo (KLMC) simulations play the role of bridge between *ab-initio* and continuum model. A more detailed explanation of modeling hierarchy (Fig. 2.1) can be found in Ref. [12].

2.1 Density functional theory

The *ab-initio* method we use is based on density functional theory (DFT). In this section, the basic concepts of DFT are summarized.

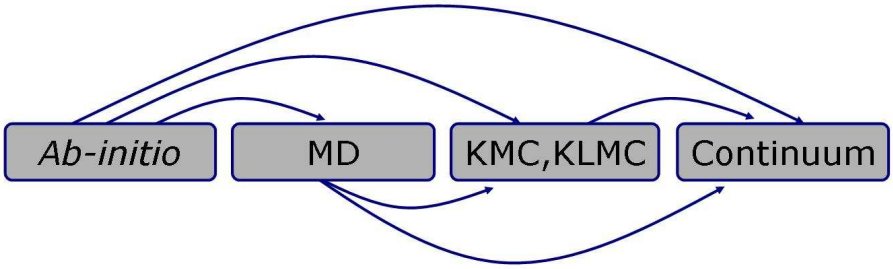

Figure 2.1: Hierarchy of various modeling techniques. *Ab-initio* provides basic parameters to higher level techniques and MD and KMC (or KLMC) bridges the large gap in time scale and system size between *ab-initio* and continuum.

2.1.1 Born-Oppenheimer Approximation

In the nonrelativistic regime, a physical system composed of N atoms with atomic number Z can be described by the Schrödinger equation:

$$\hat{H}_{total}\Psi(\vec{r},\vec{R}) = E_{total}\Psi(\vec{r},\vec{R}) \quad (2.1)$$

$$\hat{H}_{total} = -\sum_{i}^{N}\frac{\nabla_{R_i}^2}{2} - \sum_{i}^{ZN}\frac{\nabla_{r_i}^2}{2} + \sum_{i<j}^{N}\frac{Z^2}{R_{ij}} - \sum_{i}^{ZN}\sum_{j}^{N}\frac{Z}{|\vec{R}_j - \vec{r}_i|} + \sum_{i<j}^{ZN}\frac{1}{r_{ij}}, \quad (2.2)$$

where $\vec{r}$ and $\vec{R}$ are the position of electrons and nuclei, respectively. Solving Eq. 2.1 analytically is almost impossible due to the complexity of the interactions, and even finding a numerical solution for Eq. 2.1 is extremely difficult since the required computing power increases exponentially with the number of particles. Therefore, multiple steps of approximation must be made. The first is the Born-Oppenheimer approximation, by which the electronic wave function is separated from the nuclear wave function:

$$\Psi(\vec{r},\vec{R}) = \psi_I(\vec{R})\Phi_e(\vec{r},\vec{R}). \quad (2.3)$$

This separation is justified by the fact that the electronic motion is much faster than nuclear motion. As a consequence, electronic wave functions depend only on nuclear positions (the nuclei remain at fixed positions), and the nuclei see a smeared-out electron potential. Then, the Schrödinger equation can be separated as

$$\begin{aligned} \hat{H}_e \Phi_e(\vec{r}, \vec{R}) &= E_e \Phi_e(\vec{r}, \vec{R}) \\ \hat{H}_e &= -\sum_i^{ZN} \frac{\nabla_{r_i}^2}{2} - \sum_i^{ZN} \sum_j^{N} \frac{Z}{|\vec{R}_j - \vec{r}_i|} + \sum_{i<j}^{ZN} \frac{1}{r_{ij}} \end{aligned} \tag{2.4}$$

$$\begin{aligned} \hat{H}_I \psi_I(\vec{R}) &= E_I \psi_I(\vec{R}) \\ \hat{H}_I &= \sum_{i<j}^{N} \frac{Z^2}{R_{ij}}. \end{aligned} \tag{2.5}$$

The total energy of the system is the sum of electron and nucleus-nucleus interaction energies, and the latter is simply the Coulomb interaction between nuclei at fixed positions. Therefore, finding the total energy is simplified to solving Eq. 2.4.

2.1.2 Hartree-Fock Approximation

In the Hartree-Fock (HF) approximation, Eq. 2.4 is solved by a self-consistent method with an anti-symmetrized Slater determinant as the initial trial solution, which is given by

$$\Phi_e^{HF} = \frac{1}{\sqrt{(ZN)!}} \begin{vmatrix} \phi_1(\vec{r}_1) & \phi_2(\vec{r}_1) & \dots & \phi_{ZN}(\vec{r}_1) \\ \phi_1(\vec{r}_2) & \phi_2(\vec{r}_2) & \dots & \phi_{ZN}(\vec{r}_2) \\ \vdots & \vdots & \ddots & \vdots \\ \phi_1(\vec{r}_{ZN}) & \phi_2(\vec{r}_{ZN}) & \dots & \phi_{ZN}(\vec{r}_{ZN}) \end{vmatrix} \tag{2.6}$$

Applying the variational principle gives the HF equation:

$$E_e^{HF} = \sum_i^{ZN} H_i + \frac{1}{2}(J_i - K_i) \tag{2.7}$$

where

$$H_i = \int \phi_i^*(\vec{r}) \left[-\frac{\nabla^2}{2} - \underbrace{\sum_j^N \frac{Z}{|\vec{R}_j - \vec{r}|}}_{V_{ext}(\vec{r})} \right] \phi_i(\vec{r}) d\vec{r} \tag{2.8}$$

$$J_i = \sum_j^{ZN} \int\int \phi_i(\vec{r}_1)\phi_i^*(\vec{r}_1)\frac{1}{r_{12}}\phi_j^*(\vec{r}_2)\phi_j(\vec{r}_2)d\vec{r}_1 d\vec{r}_2 \tag{2.9}$$

$$K_i = \sum_j^{ZN} \int\int \phi_i(\vec{r}_1)\phi_j^*(\vec{r}_1)\frac{1}{r_{12}}\phi_i(\vec{r}_2)\phi_j^*(\vec{r}_2)d\vec{r}_1 d\vec{r}_2. \tag{2.10}$$

The K_i term introduces non-locality, which makes the HF approximation a non-linear "self-consistent-field" method. It is more clearly seen when the Coulomb operator $\hat{J}_i$ and the exchange operator $\hat{K}_i$ are defined as

$$\hat{J}_i(\vec{r}_1)f(\vec{r}_1) = \left[\sum_j^{ZN} \int \phi_j(\vec{r}_2)\phi_j^*(\vec{r}_2)\frac{1}{r_{12}}d\vec{r}_2 \right] f(\vec{r}_1) \tag{2.11}$$

$$\hat{K}_i(\vec{r}_1)f(\vec{r}_1) = \left[\sum_j^{ZN} \int \phi_j(\vec{r}_2)f(\vec{r}_2)\frac{1}{r_{12}}d\vec{r}_2 \right] \phi_i(\vec{r}_1). \tag{2.12}$$

In Eq. 2.12, the result of $\hat{K}_i(\vec{r}_1)$ operating on $f(\vec{r}_1)$ can be obtained only when $f(\vec{r})$ is known everywhere.

2.1.3 Kohn-Sham Theory

DFT is based on the Hohenberg-Kohn (HK) theorem of which the basic concept is that the electron density $\rho(\vec{r})$ is uniquely determined for a given external potential.

$$V_{ext}(\vec{r}) \rightarrow \rho(\vec{r}) \rightarrow \Phi(\vec{r}) \tag{2.13}$$

The HK theorem also states that "There exists an energy functional of electron density that is minimal for the ground state energy." The energy functional is given by

$$E[\rho(\vec{r})] = \int V_{ext}\rho(\vec{r})d\vec{r} + F[\rho(\vec{r})] \tag{2.14}$$

$$F[\rho(\vec{r})] = T[\rho(\vec{r})] + V_{ee}[\rho(\vec{r})], \tag{2.15}$$

where $T[\rho(\vec{r})]$ is the kinetic energy and $V_{ee}[\rho(\vec{r})]$ is the electron-electron interaction energy including electron-electron repulsion and all other quantum effects. The functional $F[\rho(\vec{r})]$ is universal since it doesn't depend on external potential. Therefore, if the exact functional $F[\rho(\vec{r})]$ is found, the HK theorem can describe the system exactly. Unfortunately, there is no known way to find the exact functional. Kohn and Sham cleverly introduced a fictitious non-interacting electron system giving the same ground state electron density as the true physical system. Introducing the fictitious system leads to the Kohn-Sham equation:

$$\left(-\frac{1}{2}\vec{\nabla}^2 + v_{\mathit{eff}}(\vec{r})\right)\phi_i(\vec{r}) = \epsilon_i\phi_i(\vec{r}) \tag{2.16}$$

$$v_{\mathit{eff}}(\vec{r}) = -V_{ext}(\vec{r}) + \int \frac{\rho(\vec{r'})}{|\vec{r'} - \vec{r}|}d\vec{r'} + v_{xc}(\vec{r}) \tag{2.17}$$

where

$$\rho(\vec{r}) = \sum_{i}^{ZN} |\phi_i(\vec{r})|^2 \tag{2.18}$$

$$v_{xc}(\vec{r}) = \frac{\delta E_{xc}[\rho(\vec{r})]}{\delta\rho(\vec{r})} \tag{2.19}$$

The exchange-correlation energy $E_{xc}[\rho(\vec{r})]$ is the key in DFT and links the non-interacting electron system to the physical system.

$$E_{xc} = T[\rho(\vec{r})] - T_s[\rho(\vec{r})] + V_{ee}[\rho(\vec{r})] - U[\rho(\vec{r})] \tag{2.20}$$

$$T_s[\rho(\vec{r})] = \sum_i^{ZN} \int \phi_i^*(\vec{r}) \left(-\frac{\nabla^2}{2}\right) \phi_i(\vec{r}) d\vec{r}. \quad (2.21)$$

$$U[\rho(\vec{r})] = \frac{1}{2} \int \int \frac{\rho(\vec{r'})\rho(\vec{r})}{|\vec{r'} - \vec{r}|} d\vec{r'} d\vec{r} \quad (2.22)$$

where $T_s[\rho(\vec{r})]$ is the kinetic energy of the non-interacting system and $U[\rho(\vec{r})]$ is the repulsion energy between electrons. The great advantage of DFT over the HF method is in the locality of the DFT functional.

The total energy of the system can now be written in terms of the sum of KS eigenvalues:

$$E_e = \sum_i^{ZN} \epsilon_i - U[\rho(\vec{r})] + E_{xc}[\rho(\vec{r})] - \int v_{xc}(\vec{r})\rho(\vec{r}) d\vec{r} \quad (2.23)$$

$$E_{total} = \sum_{i<j}^{N} \frac{Z^2}{R_{ij}} + E_e. \quad (2.24)$$

While the non-interacting model simplifies the equation set to be solved, it results in a loss of physical meaning of a single orbital: The wave function $\phi_i(\vec{r})$ doesn't represent the orbital of a single electron in the physical system and the physical meaning of single particle energy is not clear. In addition, DFT cannot predict excited states even when it predicts the correct ground state of a given system. That is why DFT is known as a 'ground state theory.'

2.1.4 Variations of DFT

Since DFT was established, a lot of effort has been made to find an improved $E_{xc}[\rho(\vec{r})]$ and many varieties of DFT have been developed. A detailed history of functional development is given in Appendix A. The simplest one is the local density approximation (LDA) where $E_{xc}[\rho(\vec{r})]$ is approximated as the exchange functional of a homogeneous non-interacting electron gas [48]. LDA can be extended to account for the difference between spin-up and spin-down electron densities to give the local spin density ap-

proximation (LSDA). While the assumption of homogeneous electron density gives a simple form of $E_{xc}[\rho(\vec{r})]$, it sets a limit in describing physical systems with varying electron density in space. Additionally, in spite of great success in many calculations, LDA was not popular in quantum chemistry because it couldn't achieve the so-called 'chemical accuracy' (1 kcal/mole$\approx$0.0434 eV/particle). Thus there has been much effort to improve LDA by reflecting spatial variation in the electron density and other factors. The initial attempt was the so-called 'gradient-expansion approximation' (GEA) in which the lowest-order gradient term was added to LDA $E_{xc}[\rho(\vec{r})]$. However, this correction rarely improves the LDA and is generally worse. Higher-order gradient correction was realized in the generalized gradient approximation (GGA) [49]. The GGA exchange-correlation functional $E_{xc}[\rho(\vec{r})]$ is a general function of $\rho(\vec{r})$ and $\nabla\rho(\vec{r})$:

$$E_{xc}^{GGA}[\rho(\vec{r})] = \int f(\rho(\vec{r}), \nabla\rho(\vec{r}))d\vec{r}. \tag{2.25}$$

Unlike LDA, there are many flavors of GGA depending on the method used to construct a function $f(\rho(\vec{r}), \nabla\rho(\vec{r}))$. Among the many GGA functionals, PBE [50], PW91 [51], and BLYP [52, 53] are widely-used. GEA and GGA exchange-correlation functionals are semi-local potentials in that the density value near local point is considered due to the $\nabla\rho(\vec{r})$ term. GGA functionals are further improved in meta-GGA where Kohn-Sham kinetic energy density is considered, and in hybrid functionals such as B3LYP [54] (combination of LYP [52] and B3 [55]) and PBE0 [56], where the Hartree-Fock exchange term is combined with the standard DFT functional. The hybrid functionals and meta-GGA functionals are also called orbital functionals due to the dependence on kinetic energy density and a combination of orbital functionals. The self-interaction correction (SIC) is another important orbital functional developed to remove self-interaction energy for a single electron system [57]. It can be combined with any type of GGA functional. Fig. 2.2 shows the hierarchy of DFT

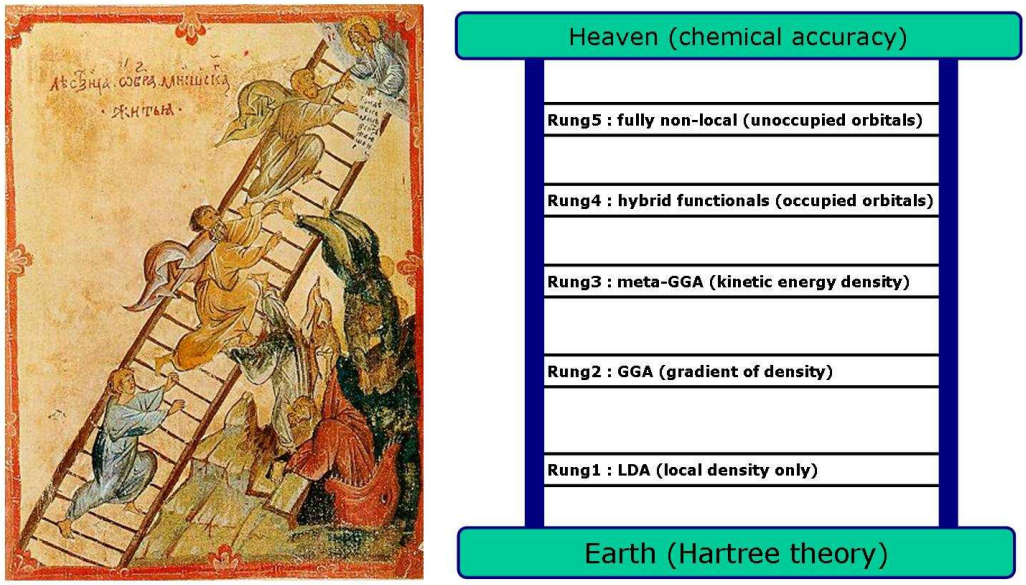

Figure 2.2: Left: "Ladder to Paradise" by St. John Climacus (15th century, Lenin Library, Moscow). Right: Heirarchy of DFT functionals based on John Perdew's presentation at DFT symposium in Menton, France.

functionals. There is still a lot of ongoing effort to reach 'Heaven'.

2.1.5 Implementation of DFT in VASP

In DFT, Eq. 2.16 should be solved self-consistently to get total energy of a system. Therefore, DFT is inherently a numerical method and thus many approximations are involved in its implentation. There are many different DFT codes depending on the basis sets used to describe electronic wave functions and the approximation method of the potential (Table 2.1), and they fall into two major groups: plane-wave basis sets and local basis sets. Fig. 2.3 shows the basic algorithm of a typical plane-wave basis code, VASP (Vienna *Ab-initio* Simulation Package) [58, 59, 60]. With local orbital basis sets, calculations can be done with relatively small number of basis functions, and it is possible to implement linear-scaling DFT methods in which the required

Table 2.1: Various DFT codes. They can be classified as two major groups depending on the employed basis sets: local orbital basis codes, plane-wave basis codes. (Source: Ref [14]). PAW=projector-augmented wave method [15], LAPW=linearized augmented plane-wave method [16].

Name	Basis Set	Potential	Web Site
Plane Wave PP codes			
ABINIT	Plane wave	PP, PAW	www.abinit.org
CASTEP	Plane wave	PP	www.tcm.phy.cam.ac.uk/castep/
CPMD	Plane wave	PP	www.cpmd.org/
Cacapo	Plane wave	PP	dcwww.camp.dtu.dk/campos/Dacapo/
FHImd	Plane wave	PP	www.fhi-berlin.mpg.de/th/fhimd/
PWscf	Plane wave	PP	www.pwscf.org/
VASP	Plane wave	PP, PAW	cms.mpi.univie.ac.at/vasp
PP Codes with Other Basis Set			
Quickstep	Gaussian+ plane wave	PP	cp2k.berlios.de/quickstep.html
SIESTA	Local/numericl	PP	www.uam.es/departamentos/ciencias/ fismateriac/siesta
All-Electron Codes			
CRYSTAL	Local	all-electron	www.crystal.unit.it
FPLO	Local	all-electron	www.ifw-dresden.de/agtheo/FPLO
Gaussian03	Local	all-electron	www.gaussian.com
ADF	Local	all-electron	www.scm.com
DMol	Local/numerical	all-electron	people.web.psi.ch/delley/dmol3.html
FLAIR	LAPW	all-electron	www.uwm.edu/ weinert/flair.html
QMD-FLAPW	LAPW	all-electron	flapw.com
WIEN2K	LAPW	all-electron	www.wien2k.at

computing resource is linearly scaling to the number of atoms [14]. On the other hand, in plane-wave basis calculations, the atomic relaxation is straightforward with the Hellmann-Feynman theorem [61, 62], and the calculated forces and stresses are quite accurate. Thus we used the plane-wave basis code, VASP, in our calculations where the induced strain is the critical parameter (see Section 2.2). In plane-wave

basis calculations, the core electrons are treated as a part of an ion to achieve basis set convergence with a practical number of basis functions, and the electron-ion interactions are described with pseudo-potentials (PPs).

When performing practical calculations, we should carefully choose the parameters to achieve a suitable compromise between accuracy and speed of calculations due to a trade-off between accuracy of the calculation result and numerical efficiency. Hence, a convergence test for major parameters is required to justify the results. In our calculations, the three major parameters affecting convergence are energy cut-off, $\vec{k}$-point sampling, and supercell size.

(a) Energy cut-off

In plane-wave basis DFT code, electronic wave functions are expanded by a linear combination of plane waves. As with Fourier expansions of a function, the more plane waves that are included, the more accurate the acquired result is. However, since only a limited number of plane waves can be included in practical calculations due to the limitations of computing resources, finding minimum number of plance-waves basis set simultaneously satisfying convergence requirement is important for efficient calculations. In VASP, the number of plane waves is determined by the energy cut-off. We use a relatively large energy cut-off since stress energy is a major factor in our DFT calculations and the error tolerance must be much smaller than the typical stress energy. A slightly larger value than 1.3×ENMAX, as suggested for stress calculations by VASP [60], is used. Whenever B is involved in formation energy calculation, all energy terms in the equation are obtained with a 340 eV energy cut-off. Otherwise, 250 eV was used. The convergence test for this choice of energy cut-off was reported in Ref. [12].

(b) $\vec{k}$-point sampling.

In DFT free energy calculations, we frequently encounter integration of a func-

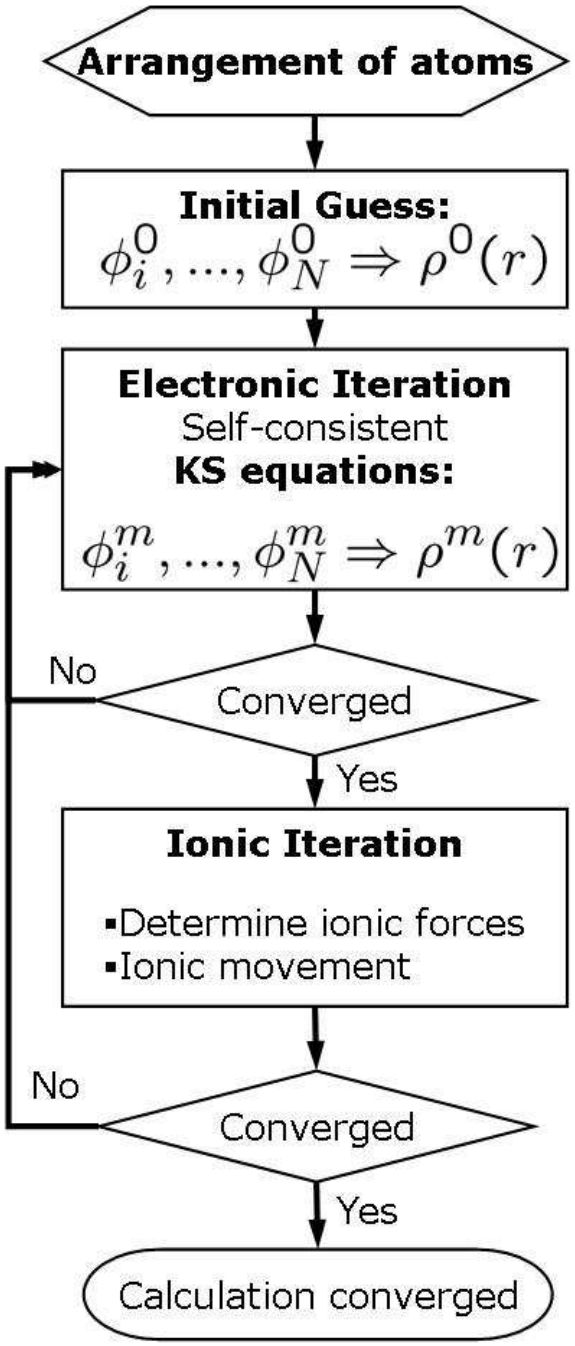

Figure 2.3: Basic algorithm of the DFT code VASP. There are two different kinds of iteration loops: electronic iteration and ionic iteration. Each iteration ends when convergence conditions set by the user are satisfied.

tion over the first Brillouin zone (BZ), and this integration is approximated as a summation over the specifically chosen discrete $\vec{k}$-points. Finer $\vec{k}$-point grids can reduce numerical error, but consume more computing resources. Since the volume of the first BZ is inversely proportional to that of the supercell, the $\vec{k}$-point mesh and supercell size should be considered simultaneously for the convergence test. In 64 atom supercells based on Si, 2^3 Monkhorst-Pack [63, 64, 65] $\vec{k}$-point sampling shows good convergence behavior (Ref. [12]).

(c) Supercell size

In addition to $\vec{k}$-point-related size effects, the supercell size also contributes to finite size effects. Due to the constraints of periodic boundary conditions, the lattice structure of a small supercell with a point defect may not be fully relaxed within the supercell, resulting in a different equilibrium lattice constant. As shown in Table 2.2, the 216-atom supercell gives a different lattice constant, but the induced strain due to point defects is the same in both 64 and 216-atom supercells (216-atom calculations are done with gamma point sampling due to limitation of computing resource). Hence we use a 64-atom supercell throughout this dissertation. Since we carefully factored out the stress energy term in binding energy calculation, finite size effects are further reduced. We also applied the Madelung energy correction [66] for a charged supercell to reduce finite size effects.

In addition to a large energy cut-off, we use the reciprocal space projection scheme and a very strict force convergence limit of 0.005 eV/Åto achieve the high accuracy required for stress calculations [60]. We also avoid the well known underestimated band gap problem of Si in DFT [67] by using the charged supercells as references so that no energy level is filled above the valence band maximum and thus the band gap energy does not enter into the formation energy (see Chapter 5).

Table 2.2: Equilibrium lattice constant and corresponding normalized induced strain for different supercell sizes. 216-atom supercell calculations are done only with Γ point. The numbers in parenthesis are normalized induced strain. Though the equilibrium lattice constants of Si in different size supercells are slightly different, the relative change in lattice constant (induced strain) is almost the same in both supercells.

	64 atom 2^3 $\vec{k}$-points	216 atom Γ point
Si	5.4566 (0)	5.4583 (0)
B	5.4306 (0.302)	5.4505 (0.311)
P	5.4497 (0.080)	5.4563 (0.081)

2.2 General stress energy model

2.2.1 Stress energy

Within the linear elastic limit of a material, the total free energy of a supercell can be written as

$$E = E^0 + \frac{V}{2}\sum_{ijkl}\epsilon_{ij}C_{ijkl}\epsilon_{kl}, \tag{2.26}$$

where E^0 is the minimum energy, V is supercell volume, ϵ_{ij} is the applied strain, and C_{ijkl} is the elastic stiffness tensor. When only normal stress and strain are considered, it is convenient to represent Eq. 2.26 as a vector equation:

$$E = E^0 + \frac{V}{2}\vec{\epsilon}\cdot\mathbf{C}\cdot\vec{\epsilon}. \tag{2.27}$$

Due to the symmetry of the Si crystal structure, $\mathbf{C}$ has only two independent components:

$$\mathbf{C}^{Si} = \begin{pmatrix} C_{11} & C_{12} & C_{12} \\ C_{12} & C_{11} & C_{12} \\ C_{12} & C_{12} & C_{11} \end{pmatrix} \tag{2.28}$$

Introducing a dopant/defect into the silicon lattice shifts the minimum energy lattice constant as shown in Fig. 2.4. We define this shift as the normalized induced strain $\Delta\vec{\epsilon}$. In a 64-atom supercell, it is defined as

$$\Delta\vec{\epsilon}_A = \frac{\vec{a}_{Si_{64-M}A_M} - \vec{a}_{Si}}{a_{Si}} \times \frac{64}{M}, \tag{2.29}$$

where $\vec{a}_{Si_{64-M}A_M}$ is the lattice constant of fully relaxed $\mathrm{Si}_{64-M}\mathrm{A}_M$ in three dimensions. Then the Eq. 2.27 becomes

$$E = E^0 + \frac{V}{2}(\vec{\epsilon} - x\Delta\vec{\epsilon}) \cdot (\mathbf{C} + x\Delta\mathbf{C}) \cdot (\vec{\epsilon} - x\Delta\vec{\epsilon}), \tag{2.30}$$

where x is the dopant/defect concentration ($M/64$) and $\Delta\mathbf{C}$ is the change in elastic stiffness tensor due to the dopant/defect. We ignore this term throughout this dissertation, since it is much smaller than the other terms in Eq. 2.30 as well as the thermal energy at process temperatures.

In Eq. 2.30, the quadratic term in $\vec{\epsilon}$ is the stress energy applied to a pure Si lattice without any dopant/defect, which is always cancelled out when the formation/migration energy is calculated; the quadratic term of $\Delta\vec{\epsilon}$ is the stress energy due to the dopant/defect without applied stress, which is small even at the equilibrium solubility limit and can be ignored in most cases. The most important term is the cross term of $\vec{\epsilon}$ and $\Delta\vec{\epsilon}$, which is the change in stress energy due to a dopant/defect under applied stress. For example, in our DFT calculations with a 64-atom supercell,

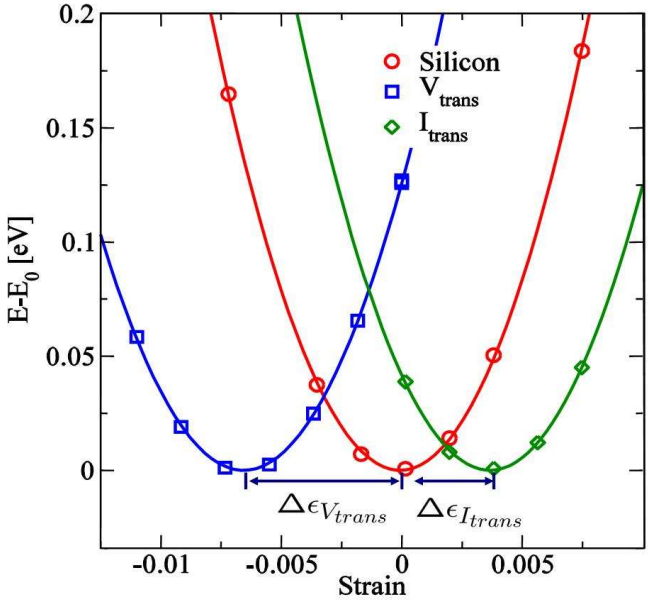

Figure 2.4: Definition of induced strain. Induced strain can be extracted from energy vs. strain curve. Change in relaxed lattice constant relative to reference lattice constant divided by reference lattice constant is defined as induced strain.

the formation energy of AB is calculated as

$$
\begin{aligned}
E^f_{AB}(\vec{\epsilon}) &= E_{Si_{62}AB}(\vec{\epsilon}) - E_{Si_{63}A}(\vec{\epsilon}) - E_{Si_{63}B}(\vec{\epsilon}) + E_{Si_{64}}(\vec{\epsilon}) && (2.31)\\
&= \underbrace{E^0_{Si_{62}AB} - E^0_{Si_{63}A} - E^0_{Si_{63}B} + E^0_{Si_{64}}}_{E^{binding}_{AB}} \\
&\quad + \underbrace{\frac{V}{2}x^2\left(\Delta\vec{\epsilon}_{AB}\cdot\mathbf{C}\cdot\Delta\vec{\epsilon}_{AB} - \Delta\vec{\epsilon}_{A}\cdot\mathbf{C}\cdot\Delta\vec{\epsilon}_{A} - \Delta\vec{\epsilon}_{B}\cdot\mathbf{C}\cdot\Delta\vec{\epsilon}_{B}\right)}_{E^{stress}_{AB}(0)} \\
&\quad \underbrace{-Vx\left(\Delta\vec{\epsilon}_{AB} - \Delta\vec{\epsilon}_{A} - \Delta\vec{\epsilon}_{B}\right)\cdot\mathbf{C}\cdot\vec{\epsilon}}_{\Delta E^f_{AB}(\vec{\epsilon})} && (2.32)\\
&= E^f_{AB}(0) + \Delta E^f_{AB}(\vec{\epsilon}). && (2.33)
\end{aligned}
$$

In Eq. 2.32, the first term is binding energy, and the last term is stress energy due to

applied stress. Both terms are independent of supercell size. The second term is also stress energy due to the dopant/defect, but it depends on supercell size. Although this term is usually small in a reasonably large supercell and thus ignorable, it may cause the finite size effect when volume expansion/contraction due to the dopant/defect is large. We treated this term carefully when it is not negligible throughout this dissertation work. The last term in Eq. 2.32 can be rewritten by using a lattice site volume V_0 instead of supercell volume, V.

$$\Delta E^f_{AB}(\vec{\epsilon}) = -V_0 \left(\Delta\vec{\epsilon}_{AB} - \Delta\vec{\epsilon}_A - \Delta\vec{\epsilon}_B\right) \cdot \mathbf{C} \cdot \vec{\epsilon}, \tag{2.34}$$

The normalized induced strain is the volume expansion coefficient β times the Si lattice concentration, and is independent of dopant concentration and cell size. $\Delta E^f_{AB}(\vec{\epsilon})$ is the key term when analyzing stress effects on the formation of AB complexes.

2.2.2 Stress effects on dopant diffusivity

It is believed that dopants in a crystalline solid diffuse via the formation of interstitial or vacancy complexes [68]. The total effective diffusivity of A is

$$D^{eff}_A = D_{AI} + D_{AV} = d_{AI}\frac{C_{AI}}{C_A} + d_{AV}\frac{C_{AV}}{C_A}, \tag{2.35}$$

where d_{AI} (d_{AV}) is the microscopic diffusivity of an AI (AV) complexes, C_{AI} (C_{AV}) is the concentration of AI (AV) complex, and C_A is the concentration of dopant A. Unless there is a reservoir or a sink for dopant A, C_A is a constant throughout the diffusion process. d_{AI} is governed by the migration energy barrier, E^m, as shown in Fig. 2.5. The stress effect on the migration barrier is given by

$$\begin{aligned} \frac{d_{AI}(\vec{\epsilon})}{d_{AI}(0)} &= \exp\left(-\frac{\Delta E^m(\vec{\epsilon})}{kT}\right) \\ &= \exp\left(-\frac{\Delta E^f_{AI^T}(\vec{\epsilon}) - \Delta E^f_{AI}(\vec{\epsilon})}{kT}\right) \end{aligned}$$

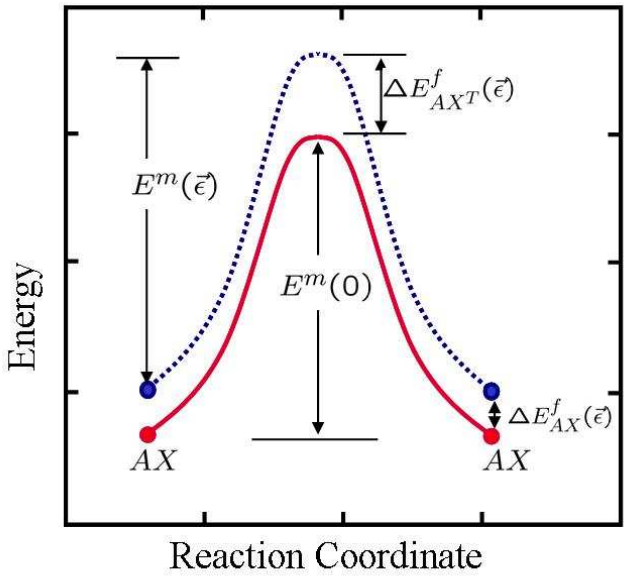

Figure 2.5: Schematic diagram for stress dependent migration energy barrier, E^m, and transition state formation energy, $E^f_{AX^T}$. AX represents dopant-defect pair. When stress is applied, both E^f_{AX} and $E^f_{AX^T}$ are changed. While the stress effect on microscopic diffusivity is determined by the change in migration energy barrier, $\Delta E^m(\vec{\epsilon})$, the stress effect on effective diffusivity is determined by the change in transition state formation energy, $\Delta E^f_{AX^T}(\vec{\epsilon})$.

$$= \exp\left(-\frac{-V_0(\Delta\vec{\epsilon}_{AI^T} - \Delta\vec{\epsilon}_{AI})\cdot\mathbf{C}\cdot\vec{\epsilon}}{kT}\right) \tag{2.36}$$

$$= \exp\left(-\frac{-V_0(\Delta\vec{\epsilon}_{AI^T} - \Delta\vec{\epsilon}_{AI})\cdot\vec{\sigma}}{kT}\right), \tag{2.37}$$

where $\Delta E^f_{AI^T}$ is the formation energy change at the transition state. The formation of an AI complex is also a function of stress:

$$\frac{C_{AI}(\vec{\epsilon})}{C_{AI}(0)} = \exp\left(-\frac{\Delta E^f_{AI}(\vec{\epsilon})}{kT}\right). \tag{2.38}$$

The stress dependence of effective diffusivity is obtained by combining Eqs. 2.35, 2.37, and 2.38.

$$\begin{aligned}\frac{D_{AI}(\vec{\epsilon})}{D_{AI}(0)} &= \frac{d_{AI}(\vec{\epsilon})C_{AI}(\vec{\epsilon})}{d_{AI}(0)C_{AI}(0)} \\ &= \exp\left(-\frac{\Delta E^f_{AI^T}(\vec{\epsilon})}{kT}\right) \\ &= \exp\left(-\frac{V_0(\Delta\vec{\epsilon}_{AI^T} - \Delta\vec{\epsilon}_A)\cdot\mathbf{C}\cdot\vec{\epsilon}}{kT}\right) \\ &= \exp\left(-\frac{V_0(\Delta\vec{\epsilon}_{AI^T} - \Delta\vec{\epsilon}_A)\cdot\vec{\sigma}}{kT}\right). \end{aligned} \tag{2.39}$$

Therefore, the stress effect on dopant diffusivity is determined by the change in transition state formation energy. The same analysis is applicable to dopant-vacancy complexes.

$$\begin{aligned}\frac{D_{AV}(\vec{\epsilon})}{D_{AV}(0)} &= \frac{d_{AV}(\vec{\epsilon})C_{AV}(\vec{\epsilon})}{d_{AV}(0)C_{AV}(0)} \\ &= \exp\left(-\frac{\Delta E^f_{AV^T}(\vec{\epsilon})}{kT}\right) \\ &= \exp\left(-\frac{V_0(\Delta\vec{\epsilon}_{AV^T} - \Delta\vec{\epsilon}_A)\cdot\mathbf{C}\cdot\vec{\epsilon}}{kT}\right) \\ &= \exp\left(-\frac{V_0(\Delta\vec{\epsilon}_{AV^T} - \Delta\vec{\epsilon}_A)\cdot\vec{\sigma}}{kT}\right) \end{aligned} \tag{2.40}$$

2.2.3 Stress effects on dopant solubility

When the concentration of dopant A becomes high enough, precipitates begin to form and the concentration of isolated A is limited by the solid solubility. The solid solubility is given by

$$C_A^{ss} = C_s \exp\left(-\frac{\Delta S}{k}\right)\exp\left(\frac{\Delta E^f_{A\to p}}{kT}\right), \tag{2.41}$$

where C_s is the lattice concentration, and ΔS ($\Delta E^f_{A\to p}$) is the change in formation and configuration entropy (formation enthalpy) per atom during the transition from the dissolved phase to the precipitate phase. When external stress is applied, Eq. 2.41 becomes

$$\frac{C^{ss}_A(\vec{\epsilon})}{C^{ss}_A(0)} = \exp\left(-\frac{\Delta S(\vec{\epsilon}) - \Delta S(0)}{k}\right)\exp\left(\frac{\Delta E^f_{A\to p}(\vec{\epsilon}) - \Delta E(0)^f_{A\to p}}{kT}\right) \tag{2.42}$$

Since the entropy term is usually much smaller than the enthalpy term, and the formation enthalpy of a precipitate has a much weaker stress dependence than that of an isolated solute, Eq. 2.42 is further simplified.

$$C^{ss}_A(\vec{\epsilon}) = C^{ss}_A(0)\exp\left(-\Delta E^f_A(\vec{\epsilon})/kT\right) \tag{2.43}$$

$$\Delta E^f_A(\vec{\epsilon}) = -V_0\Delta\vec{\epsilon}_A\cdot\mathbf{C}\cdot\vec{\epsilon} = -V_0\Delta\vec{\epsilon}_A\cdot\vec{\sigma} \tag{2.44}$$

Eq. 2.43 predicts a solubility enhancement for small atoms (e.g., B and P) and reduction for large atoms (e.g., Ga, In, and Sb) under compressive stress (vice versa under tensile stress).

2.3 Kinetic lattice Monte Carlo Simulation

Molecular dynamics (MD) simulations are a powerful tool for investigating atomic level interactions. However, with current technology, there is a large gap between the time scales that MD can simulate and the time scales in which practical diffusion processes occur [12]. In kinetic Monte Carlo (KMC) simulations, this limit is removed by ignoring atomic vibrations, and the diffusion process can be treated as a stochastic process because the fast atomic vibrations fully equilibrate the lattice before another transition occurs. Therefore, dopant/defect diffusion can be linked to a random walk process and it can be simulated with a macroscopic system size and process time scale via KMC method. Kinetic lattice Monte Carlo (KLMC) is a variation of KMC that

uses the actual discrete lattice structure.

According to harmonic transition state theory (hTST), the atomic transition rate is an exponential function of the migration energy barrier, E^m. When a dopant/defect in a lattice site migrates into another lattice site by overcoming a migration barrier, the transition rate is given by

$$\nu_j = \nu_0 \exp\left(-\frac{E_j^m}{kT}\right), \tag{2.45}$$

where ν_0 is the attempt frequency. When more than one transition path exists, the total transition rate at a given lattice site is the sum of all possible transition rates:

$$\nu = \sum_j^K \nu_j \tag{2.46}$$

The average time for a transition at a given lattice site is the inverse of this transition rate:

$$< \Delta t >= \frac{1}{\nu} = \frac{1}{\sum_j^K \nu_0 \exp\left(-\frac{E_j^m}{kT}\right)}. \tag{2.47}$$

Assuming an N-step random walk process, then the diffusivity tensor d_{pq} is related to t and Δx as:

$$d_{pq} = \frac{< \Delta x_p \Delta x_q >}{2 < t >} \tag{2.48}$$

$$= \frac{< \Delta x_p \Delta x_q >}{2\left\langle \sum_i^N \sum_j^K \left[\nu_0 \exp\left(-\frac{E_{ij}^m}{kT}\right)\right]^{-1}\right\rangle} \qquad (p, q = 1, 2, 3), \tag{2.49}$$

where $t = \sum_j^N \Delta t_j$.

The effective diffusivity tensor, D_{pq}, can be obtained by combining Eqs. 2.38 and 2.49:

$$D_{pq} = \frac{< \Delta x_p \Delta x_q >}{2 \left\langle \sum_i^N \sum_j^K \left[\nu_0 \exp\left(-\frac{E^f_{T_{ij}}}{kT} \right) \right]^{-1} \right\rangle}, \tag{2.50}$$

where $E^f_{T_{ij}}$ is the transition state formation energy for the j^{th} hopping path at the i^{th} step. In our research, we are mainly interested in the change in diffusivity due to stress.

$$\frac{D_{pq}(\vec{\epsilon})}{D_{pq}(0)} = \frac{< \Delta x_p \Delta x_q >_{\vec{\epsilon}}}{< \Delta x_p \Delta x_q >_0} \frac{\left\langle \sum_i^N \sum_j^K \left[\nu_0 \exp\left(-\frac{E^f_{T_{ij}}(0)}{kT} \right) \right]^{-1} \right\rangle}{\left\langle \sum_i^N \sum_j^K \left[\nu_0 \exp\left(-\frac{E^f_{T_{ij}}(\vec{\epsilon})}{kT} \right) \right]^{-1} \right\rangle}. \tag{2.51}$$

Here we assumed that the attempt frequency ν_0 doesn't change under stressed conditions. We use this formalism in Chapter 3 to predict stress effects on dopant (P, Ga, and In) diffusivity.

2.4 Summary

In this chapter, we reviewed the basic theory behind the modeling techniques used in this dissertation. Starting from the Born-Oppenheimer approximation, the fictitious single-electron Schrödinger equation was derived using the Kohn-Hohenberg and Kohn-Sham theorems. In spite of some known drawbacks of DFT (underestimated band gap, ground state theory), DFT is still a powerful tool which serves as the foundation of the modeling hierarchy and to explore fundamental parameters (e.g., defect formation energies, dopant/defect binding energies, induced strains due to dopants/defects, and migration energy barriers). The predictive capability of DFT can be extended up to the device level in combination with higher level modeling techniques such as MD, KMC/KLMC, and continuum simulations.

Chapter 3

STRESS EFFECTS ON DOPANT (As, P, Sb, Ga, AND In) DIFFUSION

Understanding stress effects on dopant redistribution is critical due to both intentional (mobility enhancement) and unintentional (thin films, impurity gradients) incorporation of high stress levels in nanoscale devices. In this chapter, point-defect-mediated diffusion mechanisms and stress effects on diffusivity for various dopants are investigated.

3.1 Overview

Although the formation enthalpy of point defects is positive, point defects always exists in crystalline material at finite temperatures since the entropy of mixing reduces the overall free energy of the crystal. There are two types of simple point defects: interstitials (additional atoms in the lattice) and vacancies (empty sites in the lattice). These point defects play a key role in dopant diffusion in crystalline material and cause two distinct types of diffusion: interstitial- (I-) mediated diffusion and vacancy- (V-) mediated diffusion.

In point-defect-mediated diffusion mechanisms, an immobile dopant atom A at a substitutional lattice site can become mobile via the formation of a dopant-defect AX (AI or AV) pair. In case of the interstitial mechanism, an interstitial atom kicks out a substitutional dopant atom and the kicked-out atom continues to diffuse away by forming AI pairs with other Si atoms at the nearest neighbor sites until the pair breaks apart. Since there are many different AI structures (see Appendix C), finding the minimum energy AI structure is the first step in studying stress effects on I-mediated

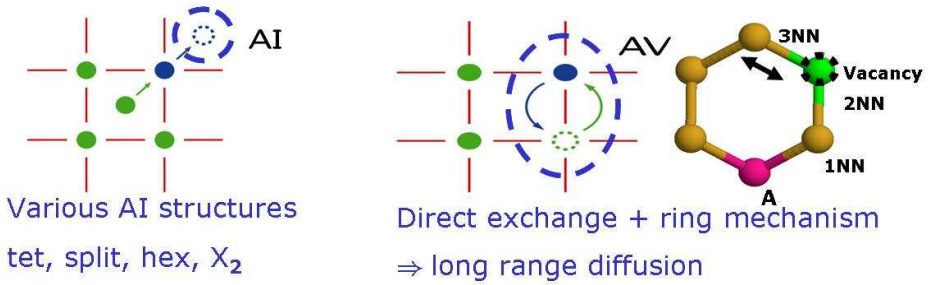

Figure 3.1: Schematic diagram of interstitial-mediated diffusion mechanism (left) and vacancy-mediated diffusion mechanism (right).

dopant diffusivity. The lowest energy AI structure have a wide variety of structures, including <110> split, <100> split, tetrahedral, hexagonal, bond-centered, and X_2 (named by Liu *et al.* [11]). On the other hand, PV pairs have the lowest energy at first nearest neighbor (1NN) spacing.

The next step is finding the AX migration path using the DFT nudged elastic band (NEB) method [33, 35, 36]. Care should be taken to check if the found migration path allows long range diffusion. Sometimes, AI pairs require multi-step migration paths for long range. For example, P diffusion occurs via inter-ring migration and intra-ring migration (see Section 3.3). In the case of a vacancy mechanism, direct exchange and the ring mechanism are required for long range diffusion. While most AV pairs (e.g., V, AsV, and SbV) have the transition state with V between 2NN and 3NN, the PV transition state is midpoint of P/V exchange [11].

Once the minimum energy AX structure and migration path are known, the induced strain due to the substitutional dopant and AX pair at transition state can be determined by plotting energy vs. strain curves using DFT. Then, the stress effects on dopant diffusivity can be predicted by analytic calculations or with KLMC simulations, as explained in Chapter 2. Fig. 3.2 summarizes the general methodology of modeling the stress effects on dopant diffusivity.

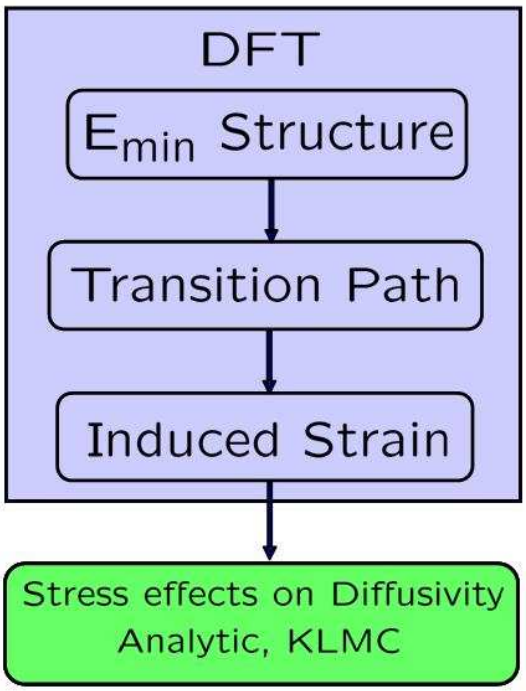

Figure 3.2: Modeling scheme of stress effects on dopant diffusivity. The first three steps are done with DFT calculations and the last step is done analytically or with KLMC.

3.2 As diffusion

As diffuses via both interstitial and vacancy mechanisms, and it is generally accepted that the vacancy mechanism is stronger than the interstitial mechanism [69, 70]. However, unlike other elements (e.g., B or P), pinning down the fractional diffusion coefficients is difficult because there exist unexpected effects such as high concentrations of As_mV_n clusters [71, 72, 73] in highly As-doped Si. In this section, the stress dependence of As diffusivity is investigated based on the fractional coefficients, f_I (0.4) and f_V (0.6), extracted by Ural *et al.* [69].

Table 3.1: Formation energies for various interstitial configurations. <110> split has the lowest formation energy. The transition state of AsI at a hex site has a 0.5 eV higher energy than the <110> split and forms a migration barrier.

	<110> split	<100> split	tet	hex
E^f (eV)	3.1	4.0	4.3	3.6

Table 3.2: Binding energies for various AsV configurations. Binding energies are calculated with an unrelaxed supercell with a lattice parameter of 5.4566 Å. Therefore, global stress effects contribute about 0.1 eV to the binding energy.

	AsV 1NN	AsV 2NN	AsV 3NN
E^b (eV)	-1.22	-0.51	-0.43

The total diffusivity of As in strained silicon is:

$$\begin{aligned} D_{total}(\vec{\epsilon}) &= D_{AsI}(\vec{\epsilon}) + D_{AsV}(\vec{\epsilon}) \\ &= D_{AsI}(0)\exp\left(-\frac{\Delta E^f_{AsI^T}(\vec{\epsilon})}{kT}\right) + D_{AsV}(0)\exp\left(-\frac{\Delta E^f_{AsV^T}(\vec{\epsilon})}{kT}\right), \end{aligned} \quad (3.1)$$

where $D_{AsI}(\vec{\epsilon})$ and $D_{AsV}(\vec{\epsilon})$ are As diffusivity by interstitial and vacancy mechanisms, respectively, and $\Delta E^f_{AsI^T}$ and $\Delta E^f_{AsV^T}$ are changes in formation energies of transition states due to stress. Since As has a similar atomic radius to silicon, the fractional contributions of both mechanisms are expected to be comparable to that for self-diffusion. The fractional contribution $f_I = D_I/D_{total}$ is given as:

$$f_I(\vec{\epsilon}) = \frac{f^0_I \exp\left(-\Delta E^f_{AsI^T}(\vec{\epsilon})/kT\right)}{f^0_I \exp\left(-\Delta E^f_{AsI^T}(\vec{\epsilon})/kT\right) + f^0_V \exp\left(-\Delta E^f_{AsV^T}(\vec{\epsilon})/kT\right)}, \quad (3.2)$$

where f^0_I is the fractional contribution of interstitial diffusion at zero strain, and $f^0_V = 1 - f^0_I$. In our calculation, 0.4 was used as a value of f^0_I [69]. The change in the

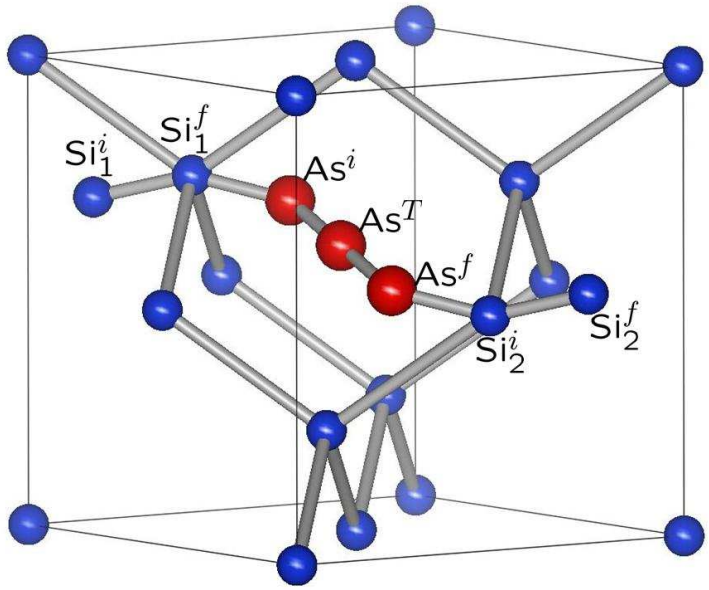

Figure 3.3: 3D view of AsI migration. $\mathrm{AsI}_{<110>split} \rightarrow \mathrm{As}_{hex} \rightarrow \mathrm{AsI}_{<110>split}$. While As migrates from a split position (As_i site) to another split position(As^f site) via a transition state (As^T site), the initial pair (As^i-Si_1^i) breaks apart and the As pairs up with one of six Si atoms in the hex ring. The As^i-Si_1^i pair is shared by two hex rings in the figure.

formation energy of transition state due to strain is

$$\Delta E^f_{AsI^T,AsV^T}(\vec{\epsilon}) = -V_0(\Delta\vec{\epsilon}_{AsI^T,AsV^T} - \Delta\vec{\epsilon}_{As}) \cdot C^{\mathrm{Si}} \cdot \vec{\epsilon}, \tag{3.3}$$

where V_0 is volume per lattice site, $\Delta\vec{\epsilon}$ is the induced strain vector, C is elastic stiffness tensor, and $\vec{\epsilon}$ is the applied strain vector.

Among many possible As interstitial configurations, the <110> split interstitial has the lowest formation energy and the hexagonal interstitial is the transition state. Table 3.1 lists the formation energies of various As interstitials. Because the interstitial configuration we used to find migration path is shared by two hexagonal rings,

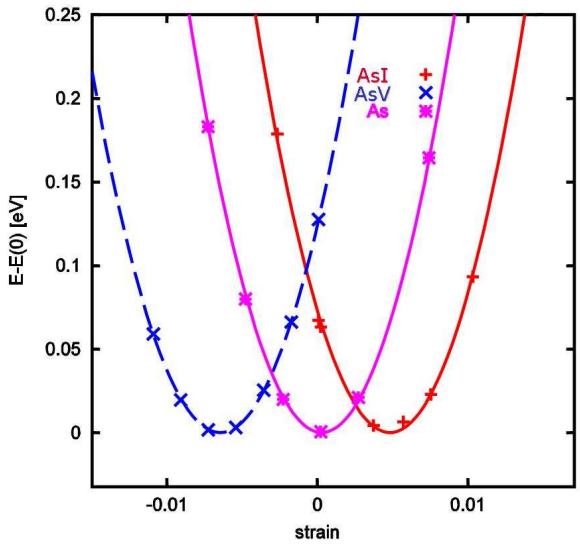

Figure 3.4: Strain dependence of free energy for a 64-atom supercell. The magnitude of induced strain for an As vacancy pair is slightly larger than that for an As interstitial pair. Therefore, the diffusivity enhancement/retardation is larger for vacancy mechanism. Energies are reported in reference to the minimum energy of each structure (energy in a fully relaxed lattice). Strains are reported in reference to the GGA Si equilibrium lattice parameter of 5.4566 Å.

Table 3.3: Induced strains of transition states and substitutional As. Induced strains are reported for one defect per atomic volume.

structure	AsI_{trans}	AsV_{trans}	As
$\Delta\epsilon$	0.309	-0.414	0.0185

As can continuously migrate from one ring to another without an additional barrier after passing through the transition state.

Therefore, the energy difference between a <110> split and hex structure determines the migration barrier. The induced strain of interstitial transition state was obtained by applying hydrostatic strain by changing lattice parameter of the supercell. Due to the symmetry of the hex site, a hydrostatic strain calculation is sufficient to obtain

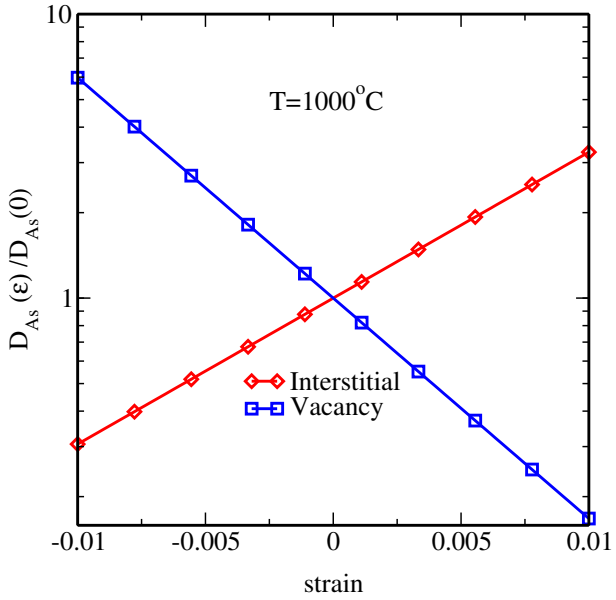

Figure 3.5: Strain dependence of diffusivity. Vacancy diffusivity increases under compressive biaxial stress and decreases under tensile biaxial stress, and it is the opposite to interstitial diffusivity. Vacancies show slightly stronger strain dependence than interstitials due to a larger induced strain.

the induced strain. Table 3.3 lists induced strains of transition states. As expected and reported previously [70], f_I increases under tensile strain and decreases under compressive strain (Fig. 3.6).

The vacancy transition state is located between 2NN and 3NN [74]. Table 3.2 shows binding energies of AsV at 1NN, 2NN and 3NN sites. The difference in binding energy between 2NN and 3NN is less than 0.1 eV, which suggests binding is not due to local binding but rather to a Coulombic interaction and global strain compensation. Therefore, the AsV transition state is equivalent to a vacancy transition state in self-diffusion, and the transition state can be treated as symmetric, allowing the induced strain to be determined from a hydrostatic strain calculation.

As seen in Table 3.3, the magnitude of the induced strain of a vacancy transition state is larger than that of an interstitial transition state. Combined, the larger

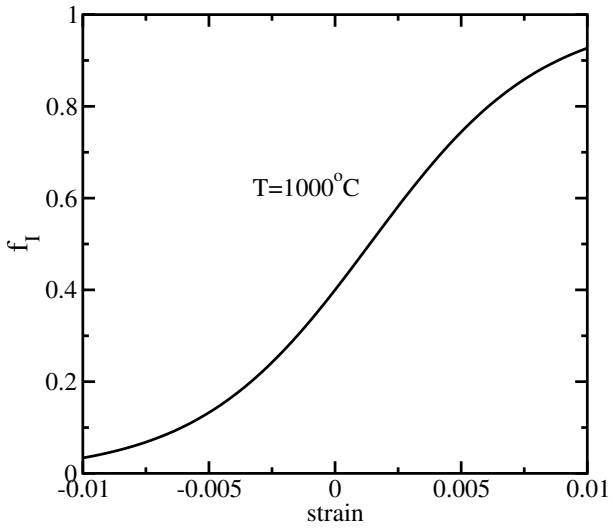

Figure 3.6: Calculated strain dependence (biaxial) of the fractional contribution to As diffusion due to interstitials. Diffusion via the interstitial mechanism is enhanced under tensile strains.

fractional coefficient of vacancy diffusion at zero strain and the stronger stress effect on the vacancy mechanism result in a total diffusivity enhancement under compressive strain and little change under tensile strain, which is consistent with experimental observations [75, 76]. However, Uppal *et al.* reported that As diffusivity in strained $Si_{0.9}Ge_{0.1}$ is lower than that in relaxed $Si_{0.9}Ge_{0.1}$ [77]. The difference in diffusivity between strained $Si_{0.9}Ge_{0.1}$ and relaxed $Si_{0.9}Ge_{0.1}$ is expected to come primarily from strain effects because the chemical effects due to the presence of Ge are the same in both cases. Based on the consensus that the diffusion mechanisms are similar in both Si and SiGe at low Ge concentration, this opposite strain dependence to that of As diffusivity in SiGe appears unusual. Because the vacancy mechanism is expected to be stronger when Ge is added [78], this behavior is surprising and requires further study.

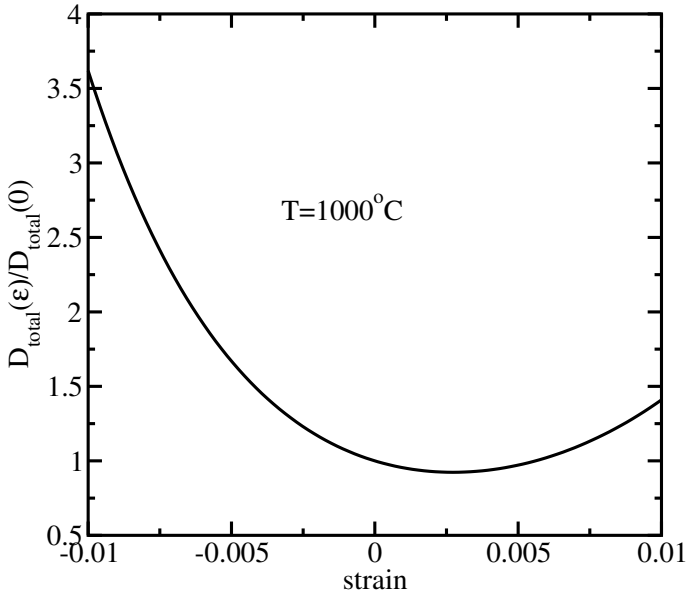

Figure 3.7: Calculated strain dependence (biaxial) of total diffusivity of As. Diffusion is predicted to increase strongly for compressive strain, but compensation of I and V mechanisms gives little change for tensile strain.

3.3 P diffusion

3.3.1 PI diffusion path

In contrast to a previous report citing PI_{hex} as the transition state of neutral PI migration with a 0.7 eV energy barrier [11], we found a new migration path with a much lower energy barrier. Liu et al. reported that dumb-bell-like <110> split interstitial and X_2 (Fig. 3.8(b)) structures have the same energy. In our calculations, however, X_2 becomes the lowest energy structure, about 0.2 eV less than the <110> split interstitial. The formation energies for various PI structures are listed in Table 3.4. As shown in Fig. 3.8, the interstitial P atom in the X_2 structure is located on a line connecting the bond-center between two substitutional sites and a hex site. The migration energy barrier to neighboring X_2 sites inside the hexagonal ring is about 0.2 eV. The induced strain due to this transition state is highly asymmetric with a large

Table 3.4: Formation energies for various interstitial configurations. X_2 (Fig. 3.8(b)) has the lowest formation energy.

	X_2	<110> split	<100> split	hex	tet
E^f (eV)	2.73	2.90	3.46	3.08	3.74

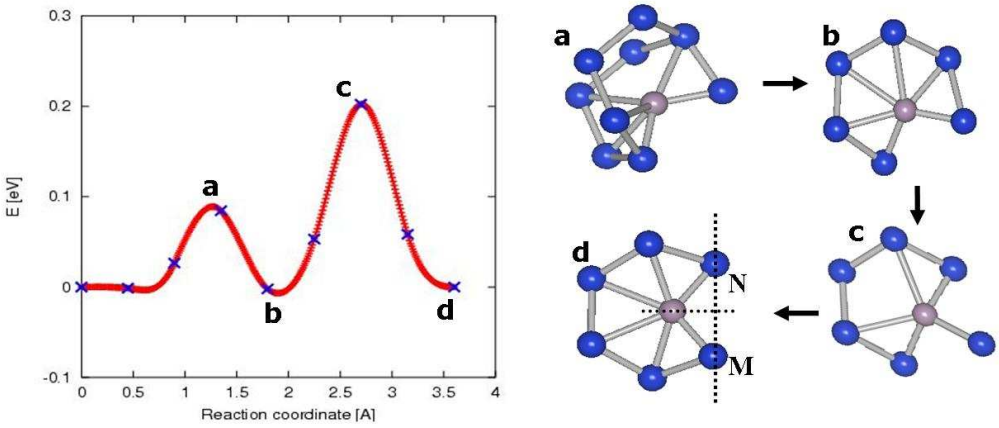

Figure 3.8: PI migration path and corresponding structures. Structure (a) is the inter-ring transition state from one hexagonal ring to another and structure (c) is the intra-ring transition state from one X_2 (b) to another X_2 (d). With these two transitions, long range diffusion is possible.

expansion in the direction perpendicular to migration and a small contraction along the migration direction (Fig. 3.8(c)).

For long range diffusion to be possible, an additional migration path between different hexagonal rings is required since the above-mentioned migration path is limited to a single hexagonal ring. In a diamond structure, a bond is shared by six hexagonal rings, thus there are six hex sites and X_2 sites every 60^o around the M-N bond in Fig. 3.8(d). The migration energy barrier to the neighboring hexagonal ring is 0.1 eV and the transition state structure is shown in Fig. 3.8(a). The induced strain due to the inter-ring transition state is almost symmetric.

Table 3.5: Induced strain for various P and PI structures. PI^1_{trans} is the intra-ring transition state and PI^2_{trans} is the inter-ring transition state. While intra-ring transitions produce strongly anisotropic induced strain, inter-ring transitions produce nearly isotropic induced strain.

	P	PI (X_2)	PI^1_{trans}	PI^2_{trans}
$\Delta\vec{\epsilon}$	$-(0.08, 0.08, 0.08)$	$(0, 0.36, 0.36)$	$(-0.05, -0.05, 0.96)$	$(0.27, 0.27, 0.25)$

3.3.2 Stress effect on P diffusivity

The energy difference between an intra-ring barrier and inter-ring barrier is comparable to thermal energy at the diffusion temperature. Therefore, both transition mechanisms were included in our KLMC simulations. The hopping network used in KLMC is shown in Fig. 3.9, where the nested hexagonal ring inside the Si hexagonal

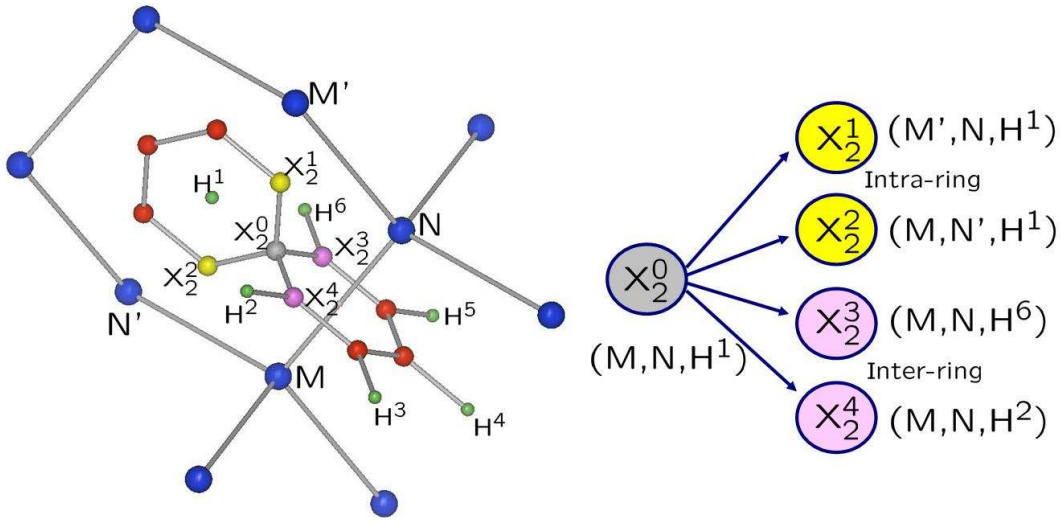

Figure 3.9: PI hopping network (color online). The large blue spheres are Si, the six small green spheres are six hex sites around M-N line, and all others are possible X_2 positions. For a given X_2^0, there are two intra-ring hopping sites (X_2^1 and X_2^2) and also two inter-ring hopping sites (X_2^3 and X_2^4).

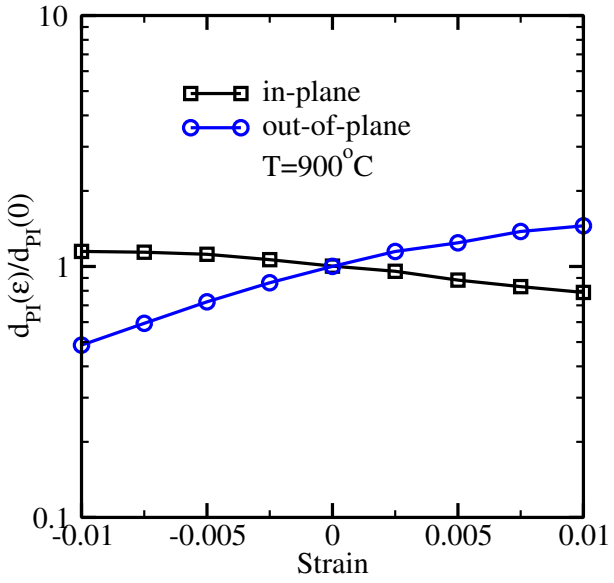

Figure 3.10: Microscopic PI diffusivity change as a function of strain under biaxial stress. While strain has negligible impact on in-plane diffusivity, out-of-plane diffusivity is a modest function of strain.

ring is the intra-ring transition network, and the other ring around M-N is the inter-ring transition network. The position of an X_2 structure can be uniquely defined by two Si lattice sites and a hex site. For example, X_2^0 can be defined by (M,N,H) in Fig. 3.9. In the KLMC simulation, these three lattice positions are updated for every hop, and the diffusivity is calculated based on Eq. 2.50.

As shown in Fig. 3.10, stress affects microscopic PI diffusivity d_{PI} only in the out-of-plane direction. However, the apparent P diffusivity, the product of d_{PI} and C_{PI} (Fig. 3.11), is retarded under compressive stress and enhanced under tensile stress in both the in- and out-of-plane directions. We compared our prediction of the effect of stress on P diffusivity via interstitials to measurements of diffusion in strained SiGe from Christensen *et al.* [2]. KLMC predictions show stronger stress effects than experimental observations (Fig. 3.13). The weaker stress effects in experiments may arise from the fractional contribution of vacancy-mediated diffusion. It is known that

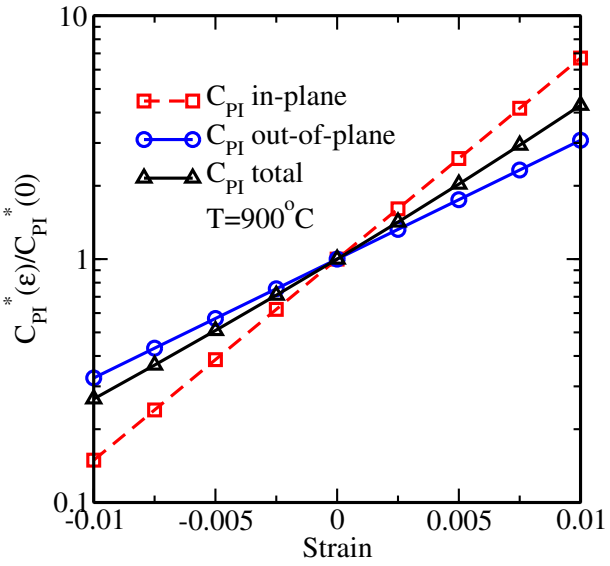

Figure 3.11: PI pair concentration change as a function of strain under biaxial stress. The in-plane concentration has a stronger strain dependence than the out-of-plane concentration.

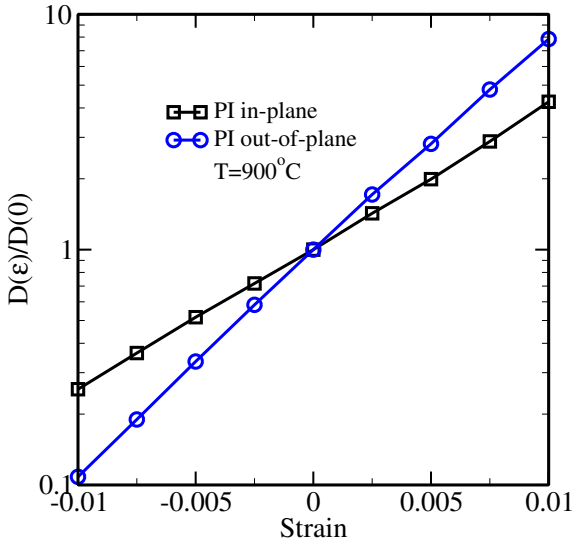

Figure 3.12: P diffusivity change as a function of strain under biaxial stress. Diffusivity is strongly affected by strain, and its impact on out-of-plane diffusivity is stronger than the in-plane diffusivity.

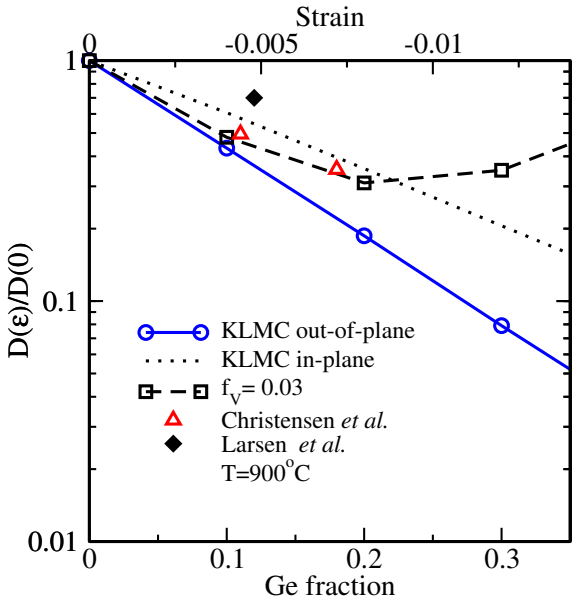

Figure 3.13: Calculated change in P diffusivity as a function of strain under biaxial stress, and comparison to experimental values from Christensen *et al.* [2] for P diffusion in strained SiGe. Inclusion of f_V=0.03 gives predictions which are consistent with experiments.

PV pair formation energy is reduced by about 0.1 eV when Ge is nearby [79] and thus vacancy-assisted diffusion is enhanced in Ge-rich Si. To understand the experiments, we performed DFT calculations on PV diffusion similar to those on AsV pair.

Unlike usual dopant-vacancy pairs, the migration energy barrier in a PV direct exchange is higher than that in a PV ring-around mechanism [11]. However, the induced strain of a PV transition state is similar to that of a V transition state. Hence, the effect of stress on PV diffusivity is nearly the same as for other dopant-vacancy pairs. Vacancy-assisted diffusion has the opposite stress dependence to that of interstitial-assisted diffusion, so that D_{PV} increases in compressively strained SiGe. When $f_V = (1 - f_I) = D_{PV}/D_P$ =0.03 is included [69], the total diffusivity becomes much flatter than D_{PI} (Fig. 3.13) and closer to Christensen *et al.*

3.4 Sb diffusion

Sb diffuses primarily via a vacancy-assisted diffusion mechanism [80, 81]. Stress effects on diffusivity of the vacancy-assisted diffusers can be easily calculated analytically due to the symmetry of the induced strain at the transition state. The transition state is located between 2NN and 3NN (Fig. 3.14). The symmetry of the induced strain at the transition state also results in isotropic stress effects under all types of normal stress (hydrostatic, uniaxial, and biaxial). As shown in Fig. 3.15, Sb diffusion is enhanced under compressive stress and retarded under tensile stress. One interesting fact is that all the dopant-vacancy data falls on a common line coinciding with self-diffusion via V. This is because the induced strains are additive (Table 3.6). When the induced strain is additive,

$$\Delta\vec{\epsilon}_{AV^T} \approx \Delta\vec{\epsilon}_{V^T} + \Delta\vec{\epsilon}_A. \tag{3.4}$$

Then, Eq. 2.40 can be approximated as

$$\begin{aligned} \frac{D_{AV}(\vec{\epsilon})}{D_{AV}(0)} &= \exp\left(-\frac{V_0(\Delta\vec{\epsilon}_{AV^T} - \Delta\vec{\epsilon}_A)\cdot\mathbf{C}\cdot\vec{\epsilon}}{kT}\right) && (3.5)\\ &\approx \exp\left(-\frac{V_0\Delta\vec{\epsilon}_{V^T}\cdot\mathbf{C}\cdot\vec{\epsilon}}{kT}\right) && (3.6)\\ &= \frac{D_{SiV}(\vec{\epsilon})}{D_{SiV}(0)}. && (3.7) \end{aligned}$$

Therefore, all the dopant-vacancy pairs we considered show the universal stress dependence on diffusivity.

Sb is overwhelmingly a vacancy diffuser in Si, and thus the vacancy-mediated diffusivity approximates the total diffusivity. We compared the change in our theoretical D_{SbV} with the change in total diffusivity versus strain for Sb measured by Larsen *et al.* [3]. We extracted the tensile stress effects from Larsen's data by taking the ratio of Sb diffusivity in tensile-strained Si to the diffusivity in relaxed Si. The compressive stress effect was calculated using the same method in SiGe. Because adding Ge in Si

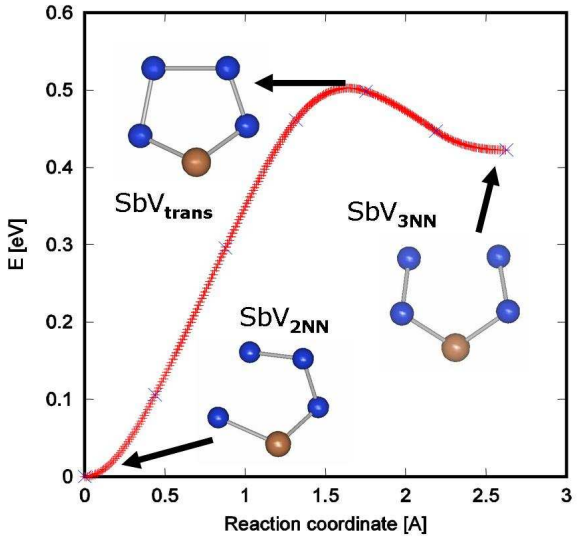

Figure 3.14: Nudged elastic band calculations of transition state for V-mediated Sb diffusion which involves V migration from 2NN to 3NN site.

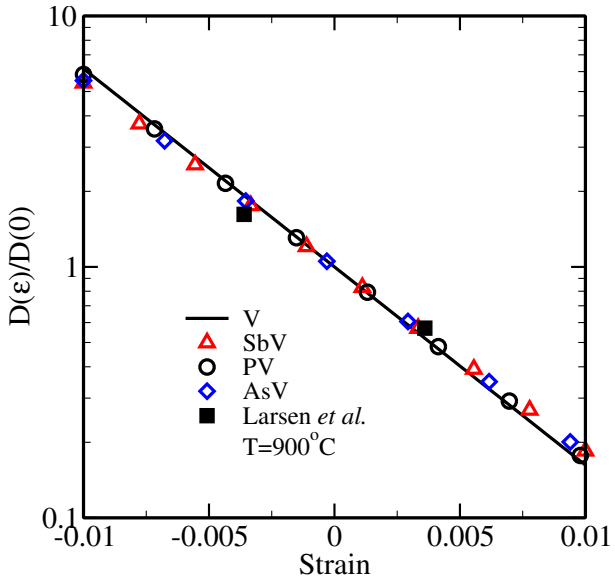

Figure 3.15: Vacancy-mediated diffusivity vs. strain for various elements under biaxial stress. For all dopants, the curves overlap with the V-mediated self-diffusion curve. Also shown is experimental data for Sb from Larsen *et al.* [3], which is accurately predicted.

Table 3.6: Induced strains of dopant-vacancy pairs at transition state. The numbers in parentheses are the induced strains of substitutional dopant. Note that the difference between two numbers are similar for all cases. Since induced strain vectors have three equal components, only a single component is presented.

	V	P	As	Sb
$\Delta\epsilon_{AV^T}$ ($\Delta\epsilon_A$)	-0.415 (0)	-0.416 (-0.08)	-0.382 (0.018)	-0.229 (0.16)

Table 3.7: Formation energies for various GaI and InI structures. In the tet_1 structure, the dopant is at a substitutional site and Si is at a tetrahedral site of the dopant (e.g., GaI^{tet}). In the tet_2 structure, they are switched (e.g., Ga_i^{tet}). Ga_{tet} (Fig. 3.16 (a)) and InI_{tet} (Fig. 3.16 (c)) structures are the minimum energy interstitial structures.

E^f eV	<110> split	<100> split	hex	tet_1	tet_2
GaI	2.72	3.72	2.99	2.47	2.11
InI	2.76	3.92	3.95	2.57	3.01

usually boosts the fractional contribution of vacancy-mediated diffusion, Sb diffusion remains mediated by vacancies in SiGe and D_{SbV} approximates the total diffusivity. The predicted values show an excellent agreement with experiments.

3.5 Ga and In diffusion

It is believed that Ga and In both diffuse via interstitial mechanism [81, 82]. As previously reported, we found Ga_{tet} and InI_{tet} to be the lowest energy interstitial structures for Ga and In, respectively [83, 84]. The formation energies of various interstitial structures are summarized in Table 3.7.

The diffusion paths for both dopants were found using DFT NEB methods [33, 35, 36]. Fig. 3.17 illustrates the GaI transition path and hopping network. GaI migration occurs via a two-step process: $Ga_i^{tet} \rightarrow GaI^{tet} \rightarrow Ga_i^{tet}$. In each step, the transition state is $GaI_{<110>}$. At the first step, Ga_{tet} migrates into one of four neighboring substitutional sites to make GaI_{tet} via $GaI_{<110>}$. The orientation of $GaI_{<110>}$ is aligned

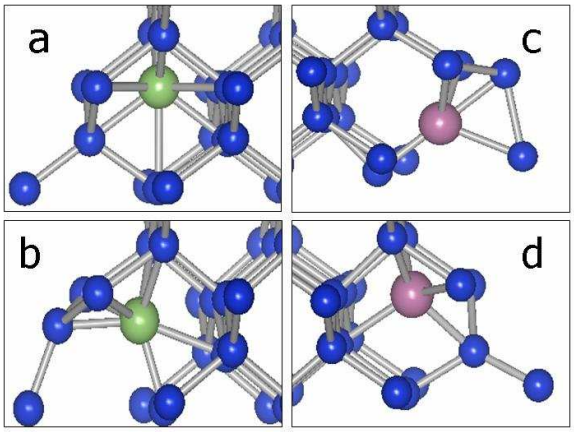

Figure 3.16: The lowest energy interstitial structures (a and c) and transition states (b and d) for Ga (left) and In (right). GaI transition state is <110> split interstitial and InI transition state is similar to In_{tet} structure.

Table 3.8: Induced strains for substitutional Ga and In, and their interstitial transition states. While Ga and GaI produce less strain than In and InI, the difference between induced strain of transition state and that of substitutional state are similar in both cases. Hence the stress effects on diffusivity are nearly the same (Fig 3.18).

	Ga	GaI_{trans}	In	InI_{trans}
$\Delta\vec{\epsilon}$	$(0.064, 0.064, 0.064)$	$(0.20, 0.20, 0.26)$	$(0.21, 0.21, 0.21)$	$(0.33, 0.33, 0.46)$

with the line connecting the initial Ga_{tet} and the Si_{tet} at the intermediate state. Therefore, three distinct orientations are possible with 1/3 of $GaI_{<110>}$ in-plane and 2/3 of $GaI_{<110>}$ out-of-plane under biaxial stress. In Fig. 3.17, T_1 and T_2 are out-of-plane transition states and T_3 is the in-plane transition states. There are a total of 12 possible transition paths in this step. The second step is the reverse of the first step. The InI migration path is the same as the GaI migration except the fact that the initial position starts from InI_{tet}. The transition state is similar to the InI^{tet} structure as shown in Fig. 3.16.

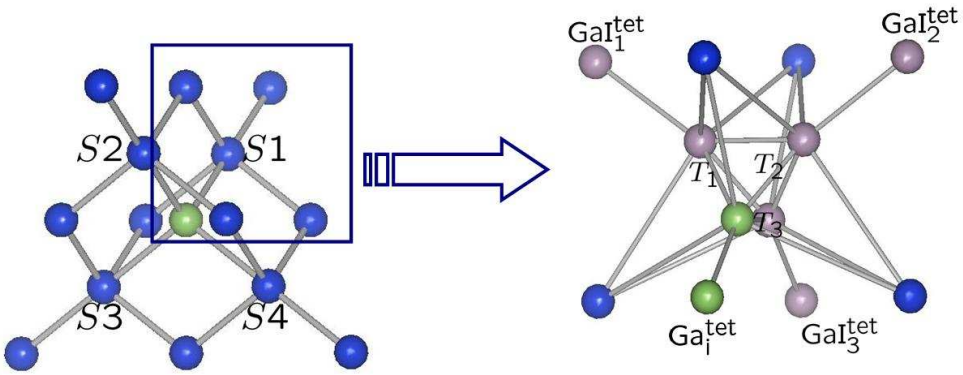

$$Ga_i^{tet} \rightarrow \begin{bmatrix} S1 \rightarrow \begin{bmatrix} T1 \rightarrow GaI_1^{tet} \\ T2 \rightarrow GaI_2^{tet} \\ T3 \rightarrow GaI_3^{tet} \end{bmatrix} \\ S2 \\ S3 \\ S4 \end{bmatrix}$$

(c)

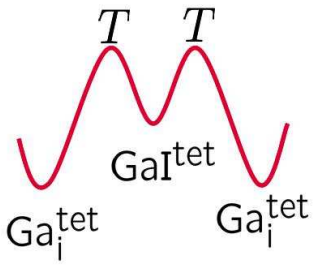

(d)

Figure 3.17: GaI hopping network for KLMC and corresponding structures. There are four neighboring substitutional sites for a given Ga_i^{tet} (a) and three available transition states for each substitutional site (b). Therefore, 12 transition paths are possible in the KLMC hopping network for half of the full transition (c). The other half of the transition is the reverse process of the first half. So there are 144 distinct transition paths for a hop. The corresponding energy is shown in (d).

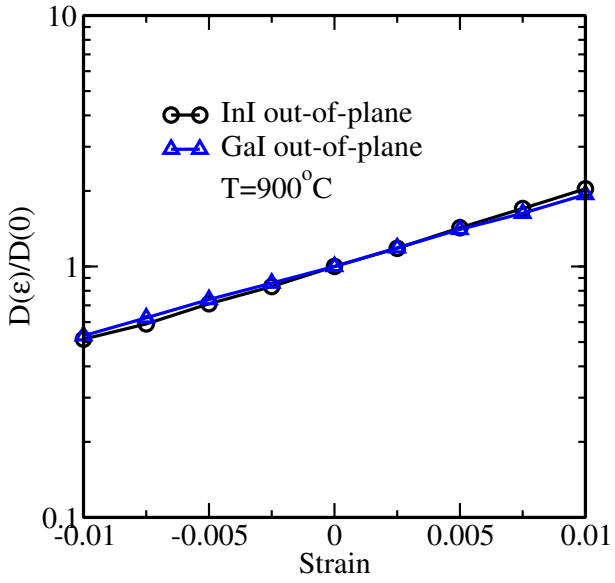

Figure 3.18: Change in Ga and In diffusivity as a function of biaxial stress. In-plane diffusivity was not plotted since it overlaps with out-of-plane diffusivity.

The KLMC results of stress effects on Ga and In diffusivity are plotted in Fig. 3.18. Due to a small difference between the in-plane component of the induced strain and the out-of-plane component of the induced strain at the transition state, stress effects are isotropic for both atoms. In addition, Ga and In have almost the same dependence of diffusivity on stress.

3.6 Summary

In this chapter, stress effects on diffusion was studied for a wide range of dopants (As, P, Sb, Ga, and In) via a combination of DFT and KLMC. Fig. 3.19 summarizes the results for all dopants studied in this chapter. Diffusion paths and induced strain tensors were found via first principles calculations, and the results were used to perform kinetic lattice Monte Carlo (KLMC) simulations when the transition state produced asymmetric induced strain.

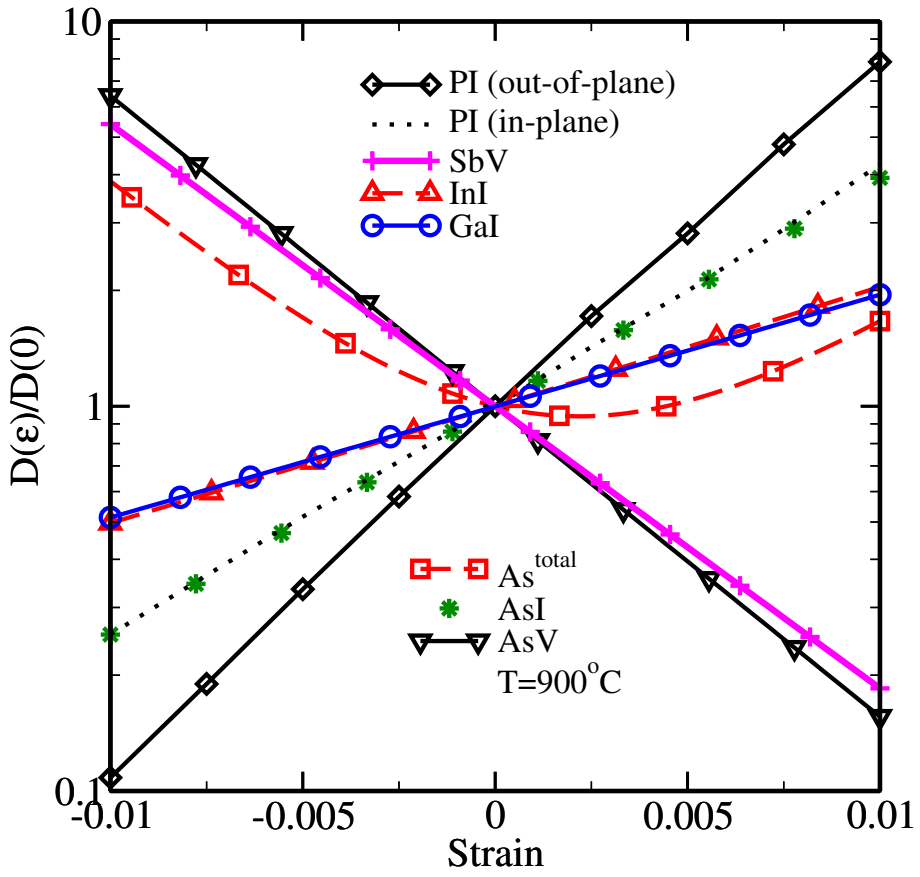

Figure 3.19: Stress effects on dopant diffusivity.

Biaxial compressive stress makes vacancy-mediated As diffusion dominant and results in an enhancement of total As diffusivity. Under biaxial tensile stress, the vacancy mechanism and interstitial mechanism compete against each other and the total diffusivity undergoes little change. A new PI diffusion path with a low energy barrier (0.2 eV) was found, and the resulting stress effects on both microscopic and effective diffusivity were calculated. Strongly anisotropic P diffusivity is predicted due to the asymmetric induced strain of the PI transition state. For Ga and In, we confirmed the previously reported interstitial diffusion path and found stress effects to be weaker and isotropic. We also found that stress effects on Sb diffusion via

Sb-vacancy pairing are similar to self-diffusion via vacancy, as well as to V-mediated diffusion of As and P.

Chapter 4

STRESS EFFECTS ON As ACTIVATION

In this chapter, we investigate stress effects on As activation in silicon using density functional theory. With particular attention to the lattice expansion coefficient, we calculated the formation energy change due to applied stress and plotted the stress dependence of the As_mV concentration. We found that biaxial stress results in minimal impact on As activation, which is consistent with experimental observations by Sugii et al. [76], who found no change in the As activation under tensile stress.

4.1 Background

The formation energy is a function of induced strain when stress is applied. Hence the induced strain is the key factor to study stress effects on As activation. The induced strain is generally a rank two tensor, but substitutional dopants produce isotropic lattice distortion, so induced strain due to a substitutional dopant becomes scalar. Cargill *et al.* observed lattice contraction at high active As concentration and attributed it to free electrons at the conduction band edge [18]. However, density functional theory (DFT) predicts that electrons result in lattice expansion (Table 4.3). To resolve this contradiction, we carefully examined the detailed local structure around As atoms in Si matrix using DFT, and determined induced strain. Based on calculated induced strains, stress effects on the active As concentration relative to the total chemical As concentration were predicted.

4.2 As deactivation kinetics

As deactivation is governed by As_mV_n cluster formation, and clusters with m=1-4 and n=1 are considered as the dominant species in deactivation kinetics [72]. Under equilibrium conditions, the concentrations of these clusters are determined by the free As and V concentrations and cluster formation energies. In the dilute limit, the concentration of As_mV is given by the mass action law:

$$C_{As_mV} = \theta_{As_mV} \frac{C_{As}^m}{C_s} \exp\left(-\frac{E_{As_mV}^f}{kT}\right), \tag{4.1}$$

where θ_{As_mV} is the number of possible distinct configurations of As_mV, C_s is lattice site concentration ($5 \times 10^{22}\text{cm}^{-3}$), and $E_{As_mV}^f$ is the formation energy of As_mV in reference to substitutional As and pure Si. The total chemical As concentration is given by

$$C_{As}^{total} = C_{As} + \sum_{m=1}^{4} mC_{As_mV}. \tag{4.2}$$

Table 4.1 lists the formation energies of As_mV complexes. Each time an As atom is added to a vacancy, the formation energy is lowered by about 1.5 eV, and thus a larger complex is more stable than a smaller one. We calculated the As_mV concentrations based on the formation energies listed in Table 4.1 and Eq. 4.1. Since DFT GGA underestimates the vacancy formation energy by about 1 eV [85], we also applied a correction for the As_mV formation energies using experimental values [17]. As_4V has the lowest formation energy and becomes the dominant cluster under equilibrium conditions. The As_4V structure is shown in Fig. 4.1. Smaller clusters can be formed during epitaxial As-doped Si growth and early stages of annealing, and can dominate before full equilibration is reached [86, 5], but we restrict our analysis to equilibrium conditions.

Fig. 4.2 shows the isolated As concentration as a function of the total As concen-

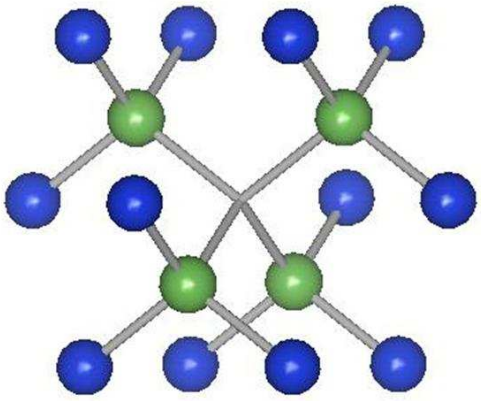

Figure 4.1: Strucuture of As_4V complex. A lattice vacancy is surrounded by 4 As atoms. Each As atom provides two electrons not involved in Si-As bond to make As_4V stable.

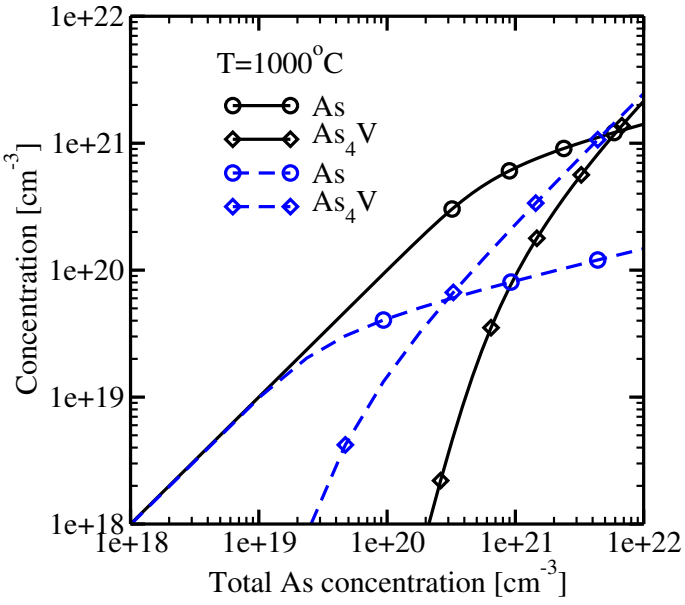

Figure 4.2: Equilibrium As concentration and As_4V concentration as a function of the total chemical As concentration. Solid lines are plotted with correction for vacancy formation energy and broken lines are plotted with DFT formation energies. Smaller clusters don't appear due to low concentration.

Table 4.1: Formation energy of As_mV clusters. When the experimental vacancy formation energy is used (4.60 eV [17]), formation energies increase by about 1 eV. The experimental value of the V formation energy was calculated by subtracting the migration barrier (0.26 eV, DFT value) from the activation enthalpy (4.86 eV [17]). In the second row, the first value is based on the DFT result, and the second is based on the experimental V formation energy.

	V	AsV	As_2V	As_3V	As_4V
E^f (eV)	3.59	2.15	0.68	-0.66	-2.22
	4.60	3.16	1.69	0.35	-1.21

tration. As the number of As forming As_4V increases to become a significant fraction of free As, the free As concentration starts deviating from the total chemical As concentration, which is consistent with previous reports [87, 5]. We should note that the As_4V formation energy is actually Fermi level dependent due to a charge transfer from the Fermi level to the cluster when As_4V forms. A higher Fermi level results in lower cluster formation energies, and thus the As_4V (As) curve becomes steeper (flatter) when the Fermi level dependent formation energy is used.

4.3 Stress effects on As activation

In equilibrium, the change in concentration of a defect X (As, V or As_mV) due to stress is given by

$$\frac{C_X(\vec{\epsilon})}{C_X(0)} \approx \exp\left(-\frac{\Delta E_X^f(\vec{\epsilon})}{kT}\right), \tag{4.3}$$

where $\Delta E_X^f(\vec{\epsilon})$ is the change in the formation energy of X due to stress. In the case of the As_mV cluster, it is given by

$$\Delta E_X^f(\vec{\epsilon}) = -V_0(\Delta\vec{\epsilon}_{As_mV} - m\Delta\vec{\epsilon}_{As}) \cdot \mathbf{C} \cdot \vec{\epsilon}, \tag{4.4}$$

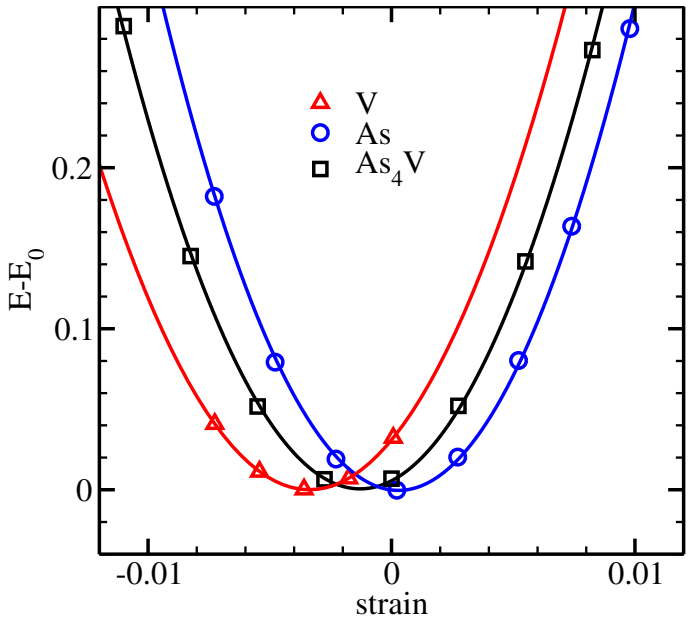

Figure 4.3: Energy vs. strain for As, V, and As_4V.

Table 4.2: Induced strain for As and As_mV complexes. As produces small lattice expansion and As_mV complexes result in lattice contraction.

	As	V	AsV	As_2V	As_3V	As_4V
$\Delta\epsilon$	0.018	-0.25	-0.21	-0.22	-0.11	-0.08

where V_0 is the volume of a lattice, $\Delta\vec{\epsilon}_{As_mV}$ ($\Delta\vec{\epsilon}_{As}$) is the induced strain due to As_mV (As), $\mathbf{C}$ is the elastic stiffness tensor of Si, and $\vec{\epsilon}$ is applied strain. The induced strain can be determined from the energy vs. strain curve. A detailed explanation can be found in Ref. [12]. To extract the energy vs. strain curve (Fig. 4.3), we calculated the total free energy of 64-atom (or 63-atom, with vacancy) super-cells using the DFT code VASP [58, 59, 60] with PW91 GGA potential [51]. All calculations were done at a 250 eV energy cut-off with 2^3 Monkhorst-Pack $\mathbf{k}$-point sampling [63, 64, 65]. The results are summarized in Table 4.2.

Several authors have observed lattice contractions in heavily As-doped Si and they

Table 4.3: Induced strain due to As, As^+, and free electrons and holes. The numbers in parenthesis are extracted from Cargill *et al.* [18]. Note that in spite of longer As-Si bond length in $Si_{63}As^+$ supercell (Table 4.4), the lattice undergoes contraction.

	As^0	As^+	e^-	h^+
$\Delta\epsilon$	0.018 (-0.019)	-0.22 (0.07)	0.22 (-0.09)	-0.26

Table 4.4: Local lattice structure around an As atom in the Si lattice compared to atomic spacing in pure Si. Lattice distortion due to As is limited to within 3NN, and removing an electron reduces the As-Si bond length and the average Si-Si bond length.

	Si	As^0	As^+	As (exp)[88]
1NN	2.36	2.45	2.43	2.43
2NN	3.86	3.87	3.86	3.87
3NN	4.53	4.53	4.52	4.53

attributed it to free electrons in the conduction band [18, 89, 90]. In contrast to their conclusion, DFT calculations predict a lattice expansion due to free electrons in the conduction band. In Cargill *et al.*, the total induced strain ($\Delta\epsilon_{As} = \beta_{\text{total}} N_{As}$) is assumed to be given by the sum of the induced strain due to ions ($\Delta\epsilon_{As^+} = \beta_{\text{size}} N_{As}$) and free electrons ($\Delta\epsilon_e = \beta_e N_{As}$). As shown in Table 4.3, in spite of the opposite sign of the induced strain due to As^o, the absolute difference is small and thus its impact on stress effects is minimal. However, the reasoning is very different in each case, and it raises a fundamental question about the role of electrons: Do electrons cause expansion or contraction in the lattice? To answer this question, we performed extensive DFT calculations to find equilibrium lattice constants of charged supercells. From the charge concentration vs. change in lattice constant (Fig. 4.4), we conclude that electrons expand the lattice while holes cause lattice contraction.

The lattice expansion due to electrons raises another question about the relation between Si-As bond length and the lattice parameter. We looked into the local

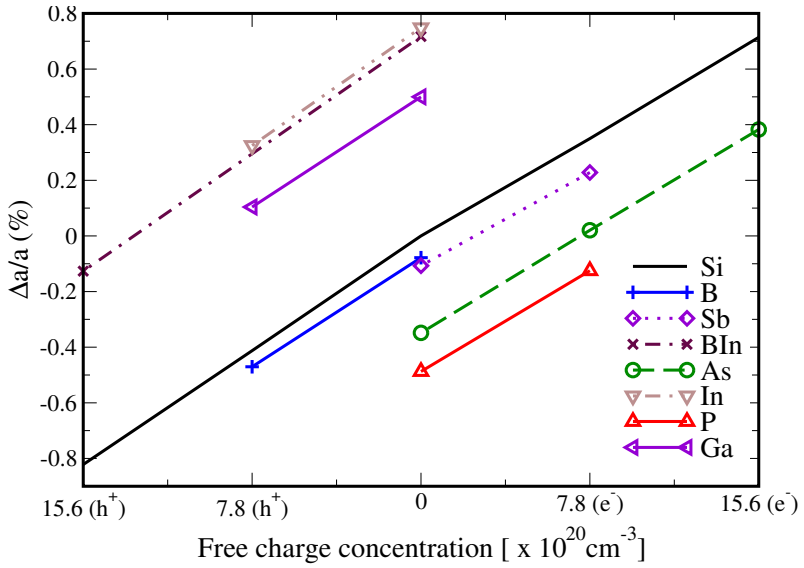

Figure 4.4: Change in lattice constant due to free charge carriers. The lattice undergoes expansion (contraction) as free electrons (holes) are added. Induced strains are obtained by finding equilibrium lattice constant of charged supercell with various dopants. One electron in a 64-atom supercell corresponds to $7.8 \times 10^{20}\text{cm}^{-3}$.

structure around As in Si matrix to answer this question. As listed in Table 4.4, DFT calculations agree with experimental measurement up to the 3NN distance and predict a local volume expansion around As [88, 91, 87]. However, this expansion is attenuated as distances increase and As-Si 3NN spacing is very similar to Si-Si 3NN distance. Therefore, changes in the 1NN bond length are not directly linked to a change in the lattice parameter, and care should be taken when linking short range atomic spacing to lattice constant. In fact, As^+ produces a lattice contraction ($\Delta\epsilon = -0.22$) in spite of longer As-Si bond length, and a free electron in the conduction/impurity band overcompensates this contraction, thus neutral As results in an overall tiny expansion ($\Delta\epsilon = 0.018$).

Based on the our analysis, it is likely that experimentally observed lattice contractions originate from reasons other than free electrons. We attribute them to high

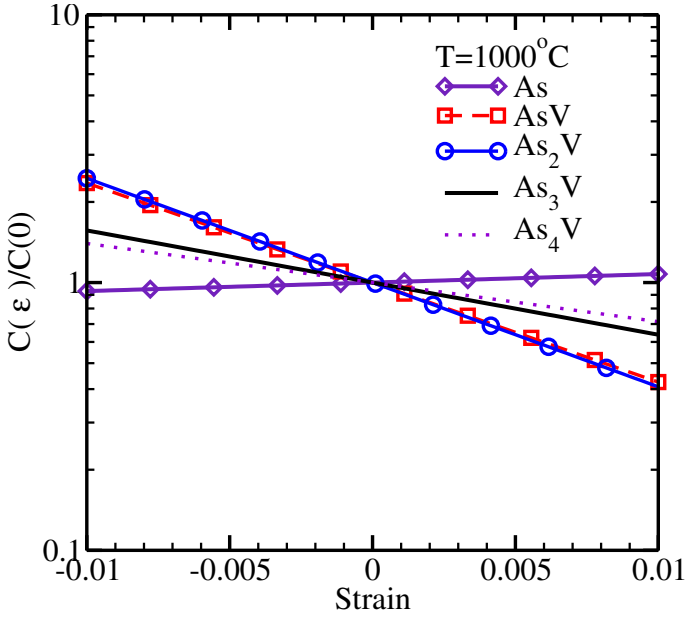

Figure 4.5: Stress effects on As and As_mV cluster concentration under biaxial stress. Note that the two dominant complexes, As and As_4V, have minimal stress effects.

concentrations of vacancies in the form of As_mV_n clusters, and find that a vacancy concentration of about 15% of the As concentration can reproduce the lattice contraction observed by Cargill et al. [18]. Even lower vacancy concentrations (8%) relative to As give the same effects when 3^3 **k**-point sampling is used. This level of vacancy concentration was reported based on *ab-initio* calculations by Berding et al. [72].

Effects of stress on As and As_mV concentrations are plotted in Fig. 4.5 based on Eqs. 4.3 and 4.4. The concentrations of the two dominant configurations, As and As_4V, undergo changes in opposite directions under biaxial stress, but the magnitude is minimal due to the small induced strain. Finally, the free As concentration as a function of the total As concentration is plotted in Fig. 4.6. At a given total As concentration, compressive biaxial stress enhances As_mV formation, and thus the number of active As decreases. However, stress effects are minimal due to the small induced strains of dominant structures, in accordance with Sugii et al. [76], who found

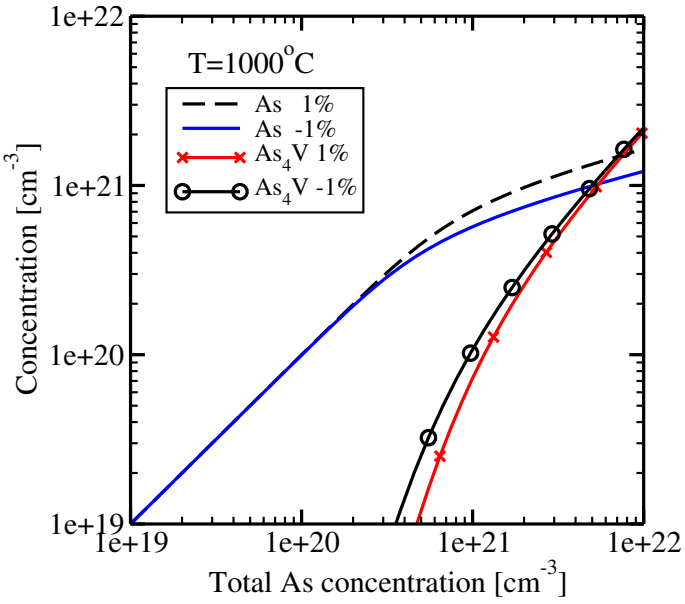

Figure 4.6: Stress effects on As and As_mV cluster concentration under biaxial stress. Note that two dominant complexes, As and As_4V, have minimal stress effects.

active As concentration to be equivalent in both 1.2 % biaxial tensile strained and unstrained Si.

4.4 Summary

By performing DFT calculations of the local structure around As in the silicon lattice, we found that lattice expansion due to the larger size of an As atom is limited to within 3NN distances. The lattice contraction in highly As-doped Si can be explained by As_mV cluster formation. As_4V formation is dominant in As deactivation at the equilibrium state. The small induced strain due to both isolated As and As_4V results in negligible stress effects on the carrier concentration, in accordance with experimental observation by Sugii et al. [76]

Chapter 5

CO-DOPING EFFECTS BETWEEN COMBINATIONS OF DONORS (P/As/Sb) AND ACCEPTORS (B/Ga/In)

In this chapter, co-doping effects in silicon are discussed with particular attention given to charge compensation, Coulomb interactions, and strain compensation. We find that for B-doped systems, As or Sb counter-doping reduces the maximum hole concentration, but that due to the strong binding of multiple P atoms, Ga or In counter-doping can increase electron density in heavily P doped material. For acceptor-acceptor pairing, we find the B-B interaction to be repulsive as expected due to Coulombic effects, but calculations show a surprisingly significant attractive binding between B and In, which we attribute to hole localization. However, B-In binding is not promising for enhancing hole concentrations since B-In pairs are deep acceptors. Both donor-acceptor and acceptor-acceptor pairing can be helpful in reducing dopant diffusion leading to more abrupt junctions.

5.1 Background

At the cutting edge of silicon technology, understanding interactions between multiple dopants is required to continue MOSFET scaling. In modern ULSI technology, heavily co-doped regions frequently occur, and it is observed that counter-doping can be beneficial to reduce the junction depth [41, 42, 43]. There are two primary factors we consider for co-doping effects: global strain compensation and local binding energy. Strain compensation between a small atom and a large atom can enhance the dopant solubility and reduce diffusivity [40, 39, 92], and local binding between donors and acceptors also produces similar effects [43, 93, 94, 95]. In co-doping, a major

component of local binding is the Coulomb interaction.

Co-doping can increase the chemical concentration of dopants and retard dopant diffusion as experimentally observed [43, 93, 96]. However, it is hard to separate out the effects of strain, electrostatics, and local chemical bonding from the other dopant/defect interactions by experiment, since in many experimental setups there is no simple way to control individual effects. In our *ab-initio* study, we separate strain energy and binding energy within the linear elasticity limit and investigate strain compensation and local binding individually.

5.2 Pairing Coefficient

5.2.1 Formation energy and stress energy

When donors and acceptors coexist in the silicon matrix, charge transfer occurs and bandgap crossing should be taken into account in calculating the formation energy of donor-acceptor pairs in reference to neutral donors and acceptors. However, it is known that DFT is inaccurate in calculating bandgaps [67]. To avoid this bandgap crossing, we used charged donors and acceptors as reference states. For acceptor-acceptor pairs (e.g., BIn) neutral supercells were used as a reference, because there is no bandgap crossing. The formation energy of a donor-acceptor pair can be given as,

$$E^f_{MN} = E_{Si_{62}MN} - E_{Si_{63}M^+} - E_{Si_{63}N^-} + E_{Si_{64}}. \tag{5.1}$$

Table 5.2 lists the calculated formation energies. Since DFT underestimates the free energy of charged supercells [66], the lowest order correction was applied ($q^2\alpha/2\epsilon L \sim$ 0.16 eV). For comparison, the two primary components of the formation energy, electrostatic energy and stress energy, are also listed in Table 5.2. E^C is calculated by monopole approximation, assuming fully ionized donor and acceptor.

Within the elastic limit of a material, the free energy of supercell is represented

Table 5.1: Induced strain due to group III/V elements. The values are reported in reference to the GGA Si equilibrium lattice parameter of 5.4566Å.

	B	As	Sb	P	Ga	In
$\Delta\epsilon$	-0.30	0.018	0.18	-0.078	0.066	0.21

as

$$E = E_0 + \frac{V}{2}(\vec{\epsilon} - x\Delta\vec{\epsilon})\mathbf{C}(\vec{\epsilon} - x\Delta\vec{\epsilon}), \tag{5.2}$$

where E_0 is the minimum energy at the relaxed lattice constant, V is the volume of the supercell, ϵ is applied strain, $\Delta\epsilon$ is the induced strain, and x is the atomic concentration of the dopant/defect. The induced strain $\Delta\vec{\epsilon} = (\Delta\epsilon, \Delta\epsilon, \Delta\epsilon)$ due to a single dopant is listed in Table 5.1. The binding energy is calculated by factoring out the stress energy from the formation energy using Eq. 5.1 and 5.2, and listed in Table 5.2.

The free energies were calculated using the density functional theory (DFT) code VASP [58, 59, 60] with the generalized gradient approximation (GGA) and ultrasoft Vanderbilt type pseudopotentials [97]. All B-related calculations were done with a 340 eV cut-off and P-related calculations were done with a 250 eV cut-off. 2^3 Monkhorst-Pack $\vec{k}$-point sampling [63, 64, 65] was used.

5.2.2 Pairing coefficient

The binding energy of a donor-acceptor pair can increase solubility and retard diffusion as reported previously [93, 43, 98, 99]. To estimate the impact of ion pairing on charge carrier density, we calculated the pairing ratio between the primary dopant and counter dopant due to binding. For the dopants considered, we find the impact of global strain compensation on solubility to be much smaller than the effect of

binding even at a high counter-dopant concentration. The pairing coefficient, the ratio between the total number of paired primary dopant atoms (e.g., B or P) and the total number of counter-dopant atoms, is given by

$$P = \frac{N^{\text{paired}}_{\text{primary}}}{N^{\text{total}}_{\text{counter}}} = \frac{\sum_{i,m} i \times C_{im}}{\sum_{i,m} C_{im}} \quad , \tag{5.3}$$

where C_{im} is the pair concentration containing i primary atoms and one counter atom. The index m is used to account for multiple combinations among 1NN, 2NN and 3NN binding for the same i. Using the mass action law at equilibrium, C_{im} is given by

$$C_{im} = \Theta_{im} C_0 (\frac{C^{free}}{C_s})^i \exp\left(-E^b_{im}/kT\right), \tag{5.4}$$

where Θ_{im} is the configurational entropy factor, C^{free} and C_s are the free primary dopant concentration and silicon lattice concentration, respectively, and E^b_{im} is the binding energy of the given configuration.

Eqs. 5.3 and 5.4 are generally applicable to binding beyond the first nearest neighbor (1NN), but we have included only 1NN multiple binding in pairing calculations reported below. It may result in a slightly weaker pairing coefficient, but it is a reasonable choice since much stronger binding at 1NN overwhelms the effect from a larger number of neighbors at 2NN and 3NN, even at high temperature. In addition, screening effects reduce the indirect binding energy beyond 1NN and at high doping concentrations, the screening length approaches the interatomic distance [100]. Under this restriction, C_{im} can be simplified to C_i (the concentration of pairs with i primary dopant atoms at 1NN). Then Eq. 5.4 can be expressed as

$$C_i = \frac{4!}{(4-i)!(i)!} \left(\frac{C^{free}}{C_s}\right)^i C_0 \exp\left(-E^b_i/kT\right) \quad (i = 0 - 4). \tag{5.5}$$

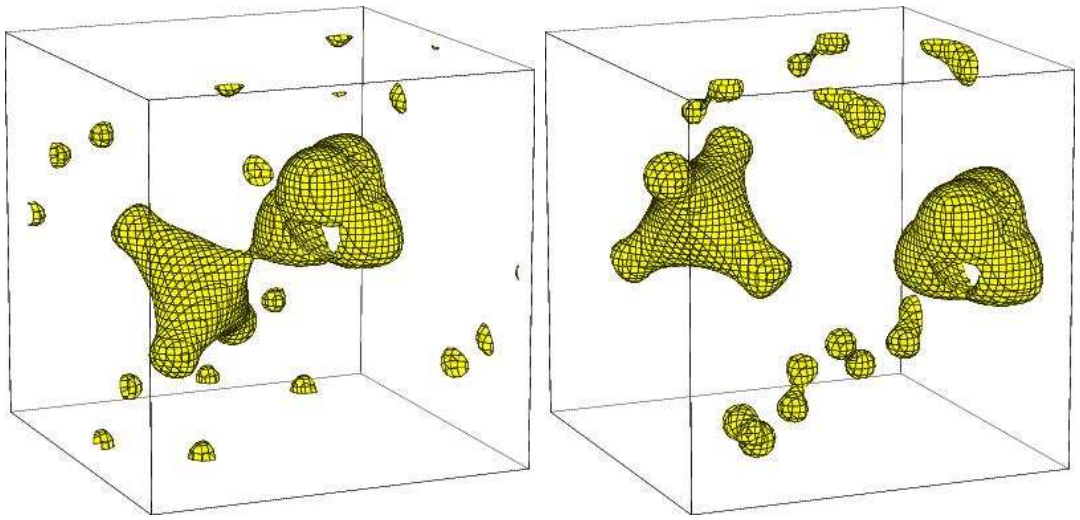

(a) BAs 1NN (b) BAs 2NN

Figure 5.1: Charge distribution of BAs at 1NN and 2NN. B is located on the left and As is on the right. Electrons around As are distributed approximately symmetrically in both cases. Their distribution around B is skewed away from the As ion at 1NN, but is nearly symmetric at 2NN. The isosurfaces were plotted at the same density ($\rho = 5.5 \times 10^{23} e/\mathrm{cm}^{-3}$).

5.3 Co-doping effects on charge carrier density

The total charge density is given by

$$n(p) = C^{\mathrm{free}}_{\mathrm{primary}} + (P-1)C^{\mathrm{total}}_{\mathrm{counter}}, \tag{5.6}$$

where $C^{\mathrm{free}}_{\mathrm{primary}}$ and $C^{\mathrm{total}}_{\mathrm{counter}}$ are the free primary dopant concentration and total counter-dopant concentration, respectively.

Using Eqs. 5.3, 5.5, and 5.6, we plotted the differential carrier density per co-dopant as a function of the concentration of free primary dopant (Fig. 5.4).

Table 5.2: Net formation energy of various ion pairs. Except for 1NN, the sums of approximate Coulomb energy (E^C) and strain compensation energy (E^S) are within 0.15 eV of E^f. BAs/InP 1NN shows weaker/stronger binding than Coulomb interaction.

eV	E^f	E^S	E^C
Si_{62}BAs 1NN	-0.34	-0.02	-0.55
2NN	-0.36	-0.02	-0.32
3NN	-0.32	-0.02	-0.27
Si_{62}BSb 1NN	-0.46	-0.08	-0.52
2NN	-0.32	-0.08	-0.32
3NN	-0.22	-0.08	-0.27
Si_{62}GaP 1NN	-0.66	-0.008	-0.50
2NN	-0.29	-0.003	-0.32
3NN	-0.21	0.0	-0.27
Si_{62}InP 1NN	-0.88	-0.02	-0.48
2NN	-0.38	-0.02	-0.31
3NN	-0.28	-0.02	-0.27

5.3.1 Donor-acceptor pairs

As listed in Table 5.2, all the donor-acceptor pairs except pairs at first nearest neighbor (1NN) show binding which is closely approximated by the sum of stress energy and Coulombic interactions. A portion of the modest difference between E^f and sum of E^C and E^S (less than 0.15 eV) may arise from the inaccuracy of the point charge approximation for the charged ions. We attribute the large energy discrepancy for donor-acceptor pairs at 1NN to direct local binding and higher order multipole interactions. Fig. 5.1 shows the highly asymmetric charge distribution for B-As at 1NN. Thus, the monopole approximation is not sufficient to accurately estimate Coulomb energy.

Table 5.3 shows the formation energy of B_nSb does not monotonically increase as B is added to Sb. This is because the small B atom produces a large strain energy. Once strain energy (the third column in Table 5.3) is factored out, the binding energy monotonically increases for all multiple binding species. Fig. 5.3 shows a monotonic

Table 5.3: Formation energy and binding energy of donor-acceptor pairs with multiple binding. In contrast to B-Sb multiple binding, In-P multiple binding produces a large negative formation energy beyond the Coulomb interaction. Fig. 5.2 shows In-related acceptor level lowering as multiple P atoms are bound to In.

eV	E^f	E^S	E^b	eV	E^f	E^S	E^b
BSb	-0.46	-0.09	-0.37	InP	-0.88	-0.02	-0.86
B_2Sb	-0.62	-0.06	-0.56	InP_2	-1.36	-0.04	-1.32
B_3Sb	-0.67	0.11	-0.78	InP_3	-1.77	-0.05	-1.72
B_4Sb	-0.62	0.41	-1.03	InP_4	-2.19	-0.05	-2.14
GaP	-0.66	-0.01	-0.65	InAs	-0.82	0.006	-0.83
GaP_2	-1.01	-0.01	-1	$InAs_2$	-1.2	0.013	-1.21
GaP_3	-1.29	0	-1.29	$InAs_3$	-1.5	0.02	-1.52
GaP_4	-1.48	0.02	-1.5	$InAs_4$	-1.68	0.027	-1.71

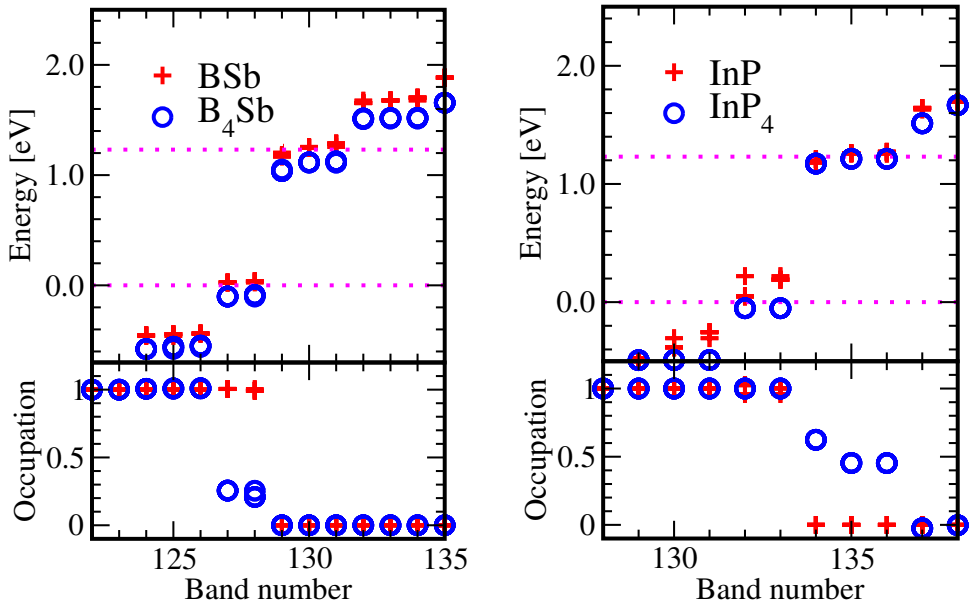

(a) B-Sb pair

(b) In-P pair

Figure 5.2: Density of states of donor-acceptor pairs with multiple binding. In contrast to B-Sb pairs, the energy levels associated with In near the top of the valence band are lowered significantly with the addition of P. The large binding energy of InP_n is attributed to this energy level lowering.

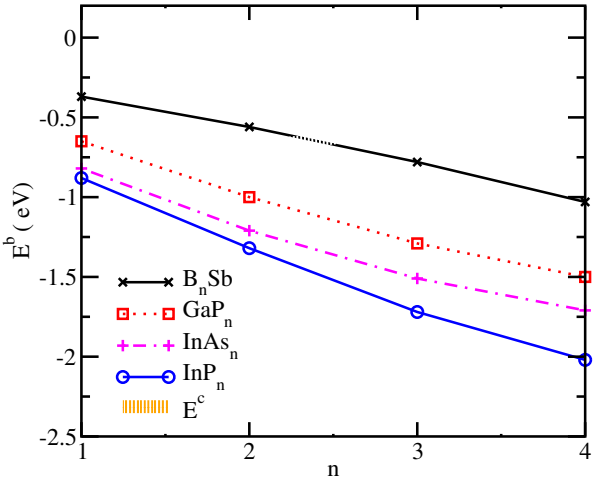

Figure 5.3: Binding energy for multiple binding. The thick orange line represents the monopole Coulomb approximation.

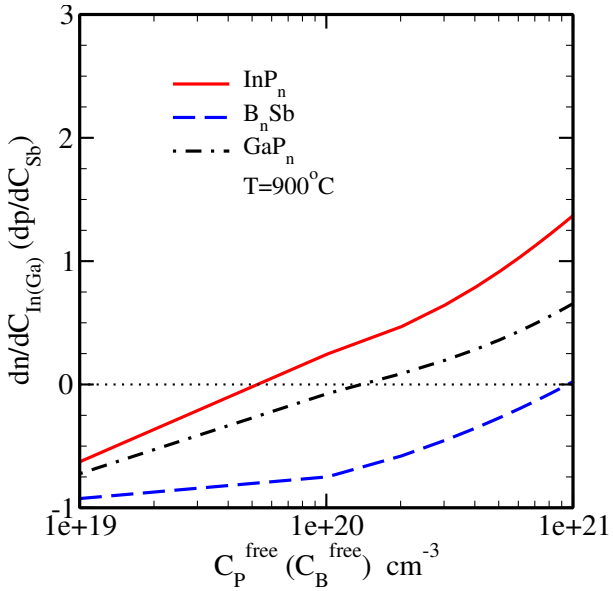

Figure 5.4: Differential free charge concentration per co-dopant atom as a function of the concentration of free primary dopants. The number of paired B atom per Sb is less than 1, which means BSb binding energy is not large enough to overcome charge compensation. However, strong multiple binding between In and P may be beneficial to increase electron charge density.

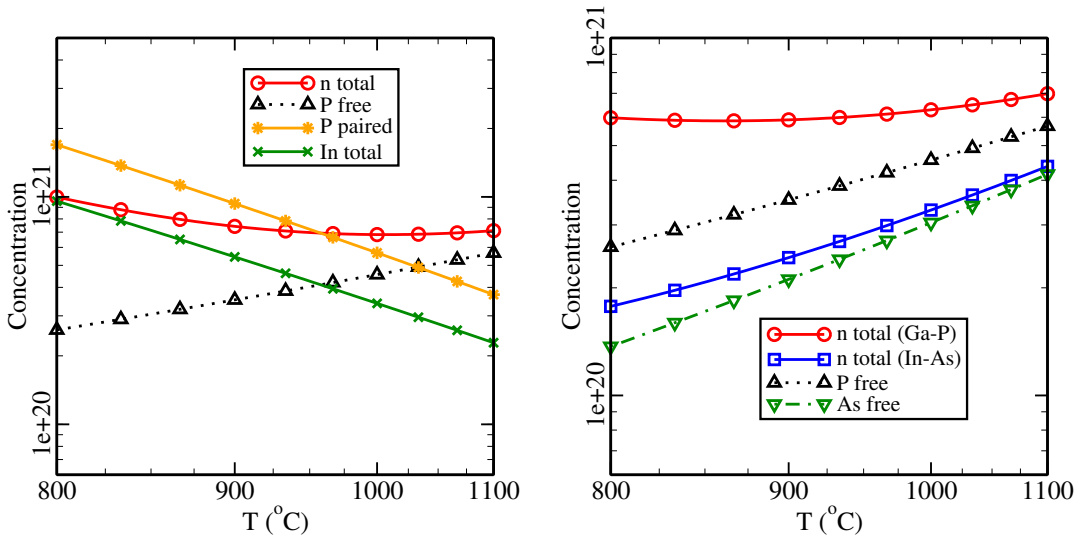

(a) In-P pairing

(b) In-As, Ga-P paring

Figure 5.5: Total charge density as a function of temperature. Despite large As chemical solubility, pairing effects are minimal due to smaller As electrical solubility compared to P. Electrical solubility of P and As was taken from Solmi *et. al.* [4] and Derdour *et. al.* [5], respectively.

increase in binding strength as more dopants are bound to a counter-dopant, which implies that the monopole Coulomb approximation clearly fails at 1NN. It is notable that the binding energy of InP_n is quite large, while that of B_nSb is much smaller. We believe that the strong binding between In and P is related to the lowering of the initially deep In acceptor energy level when P binds to it (Fig. 5.2). Atoro *et al.* has suggested making In shallow acceptors via trimer with P (In-P-In) [101].

Based on multiple binding between donors and acceptors, the differential carrier density (Fig. 5.4) and total carrier density (Fig. 5.5) due to counter-doping were calculated. Fig. 5.4 shows the change in carrier density as a function of free primary dopant (P or B). The negative value for B_nSb up to well above equilibrium B solubility implies that binding is not strong enough to overcome charge compensation between

donors and acceptors for this combination. Consistent with this prediction, Solmi *et al.* reported a reduction in carrier densities due to B-Sb pairing [43]. For the case of InP_n, dn/dC_{In} becomes positive well below P solubility. Although In solubility is low ($1.8 \times 10^{18}cm^{-3}$ [102]) in pure silicon, pairing with P substantially increases In solubility well above the normal value (Fig. 5.5(a)). Ga-P pairing is also predicted to give substantial activation enhancement, but due to smaller As electrical solubility compared to P, In-As pairing doesn't increase the total electron density significantly. Fig. 5.5 was plotted assuming the same free primary dopant concentration as its equilibrium solid solubility in Si. Counter-doping and associated pairing can also be beneficial in the formation of abrupt junctions by suppressing dopant diffusion [93, 43, 96].

5.3.2 Acceptor-acceptor pairs

When two acceptors are closely spaced, Coulomb repulsion is expected. Although this is true for two B atoms, as listed in Table 5.4, B-Ga binding is weakly attractive, and B-In has a substantial binding energy. We believe that the holes associated with B are delocalized and thus ionized B atoms repel each other. However, in conjunction with the larger ionization energy, holes associated with In atoms (and to a lesser extent Ga) are more localized, and the localization is enhanced by the presence of an additional acceptor. Localized holes then stabilize the formation of B-In (and B-Ga) pairs. Fig. 5.6 shows a comparison of hole distribution around B, In, and BIn. This mechanism is supported by the fact that removing the holes by considering negatively charged cells leads to the elimination of B-In binding (Table 5.5).

Unlike donor-acceptor pairing, no charge compensation is involved, so acceptor-acceptor binding might be expected to lead to enhanced hole concentrations. Unfortunately, our calculations indicate that the BIn pair is a deep acceptor as shown in Fig. 5.7(b), with both acceptor levels located well within the gap. This prediction is supported by the experimental results of Scalese *et al.* [96], who found that

Table 5.4: Formation energy of acceptor-acceptor pairs. B-B interaction is repulsive, while BIn shows strong attractive binding.

	B_2	BGa			BIn		
eV	1NN	1NN	2NN	3NN	1NN	2NN	3NN
E^f	0.93	-0.06	-0.10	-0.08	-0.41	-0.29	-0.20
E^S	0.28		-0.03			-0.10	
E^b	0.65	-0.03	-0.07	0.05	-0.31	-0.19	-0.10

Table 5.5: Formation energy of BIn for various charge states. When holes are removed, BIn interaction goes from attractive to repulsive.

eV	BIn	BIn^-	BIn^{2-}
E^f	-0.41	-0.21	0.12

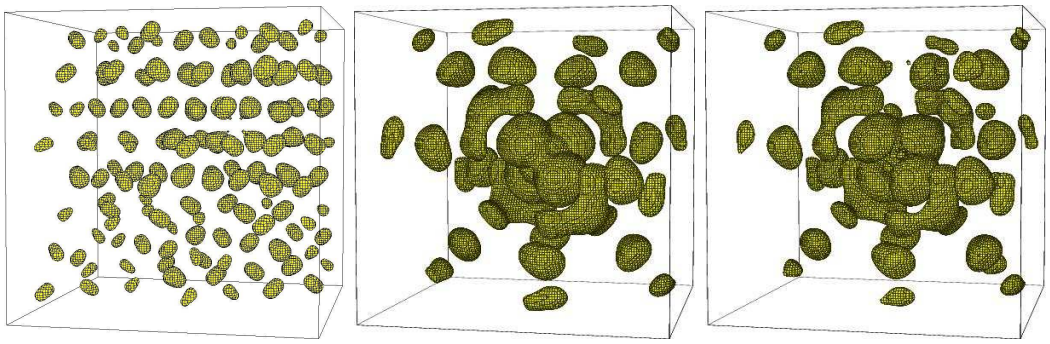

(a) B (b) In (c) BIn

Figure 5.6: Hole density of (a) B, (b) In, and (c) B-In pair calculated by taking the difference in charge density between a singly charged cell and a neutral cell. All isosurfaces were plotted at the same density ($\Delta\rho = 2.15 \times 10^{21} e/\mathrm{cm}^{-3}$).

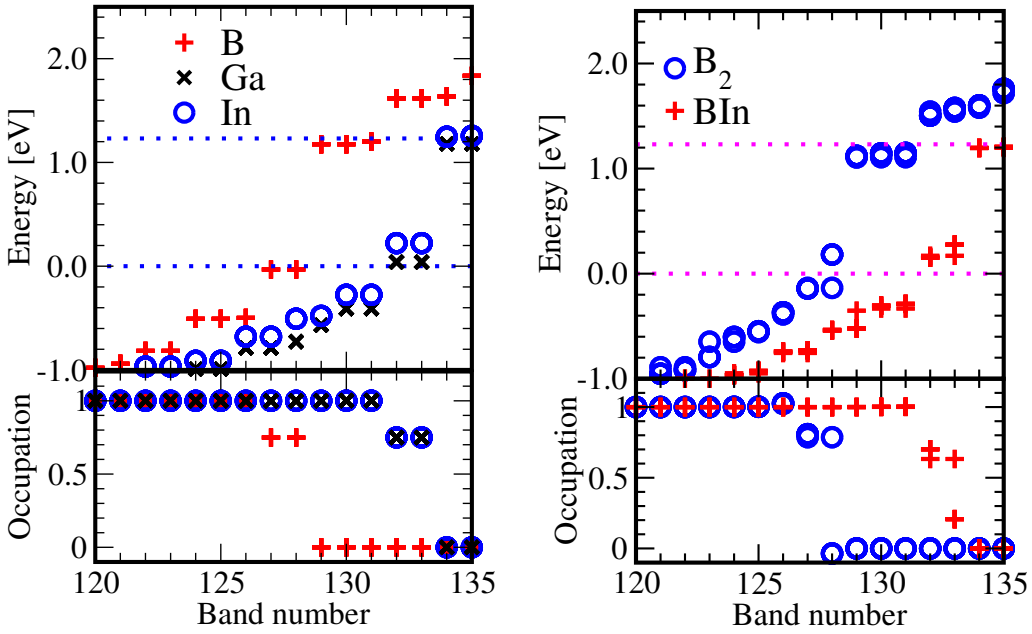

(a) Single acceptor level

(b) Acceptor pairs

Figure 5.7: Density of states of single acceptors and acceptor-acceptor pairs. In B_2, acceptor states are located below the top of the valence band maximum, but in BIn pair two holes are in deep level.

In co-doping deactivates B. Previous theoretical work by Szmulowicz *et al.* confirm that B-In pairs have a large first ionization energy [103]. However, as in the case of donor-acceptor pairing, In can be used to reduce B diffusion [92].

5.4 Summary

In conclusion, we have investigated the binding of various donor-acceptor pairs and acceptor-acceptor pairs and analyzed the resulting impact on maximum charge carrier density. Counter-doping of B with As or Sb can reduce the junction depth due to retarded B diffusivity, but the calculated pairing effect is not large enough to overcome charge compensation between opposite dopant types. Counter-doping of P with Ga

or In, however, is predicted to enhance electron concentration via pairing of multiple P atoms with a single In or Ga atom, thereby providing an increase in the maximum concentration of electrically active P which exceeds compensation via the acceptors. B-In shows a surprisingly significant attractive binding, which we attribute to localized holes overcoming expected ionized acceptor repulsion. However, B-In co-doping leads to reduced, rather than enhanced, hole density because it produces deep acceptor levels. For both donor-acceptor and acceptor-acceptor co-doping, attractive binding is also expected to lead to reduced diffusion and thus more abrupt junction formation.

Chapter 6

B DIFFUSION IN STRAINED $Si_{1-X}Ge_X$

Using an extensive series of first principles calculations, we have developed general models for the change in energy of boron migration state via interstitial mechanism as a function of local alloy configuration. The model is based on consideration of global strain compensation as well as local effects due to nearby arrangement of Ge atoms. We took a statistical average over many alloy configurations based on the change in migration energy to explain the reduced B diffusion in strained SiGe and compared our results to experimental observations. These models include significant effects due to both global stress and local Ge effects, and accurately predict the B diffusivity measured experimentally in strained $Si_{1-x}Ge_x$ on Si as a function of Ge content.

6.1 Background

There is great interest in utilizing SiGe for enhanced mobility, increased activation, and reduced contact resistance, and many authors have shown that boron diffusion is retarded in strained SiGe [45, 46, 9, 10]. However, the physical mechanism is not well understood and theoretical explanations are still controversial and even contradictory. Kuo *et al.* concluded that stress effects are not significant [45] and Lever *et al.* attributed diffusivity reduction to B-Ge pairing [46]. Later, Hattendorf *et al.* found that there is no significant binding between B and Ge using the β-NMR technique [47]. Previous ab-initio calculations by Wang *et al.* suggested that the presence of Ge increases the migration energy and reduces the concentration of Si interstitials [104]. In order to control device structures at the nanoscale, a fundamental understanding of the effects of alloy concentrations and associated strains is critical. We investigated

the B diffusion mechanism in strained $Si_{1-x}Ge_x$ to solve the controversy, considering both global strain compensation and local Ge configuration.

6.2 B diffusion mechanism

B in a Si lattice diffuses mainly via interstitial mechanism [69], and previous research indicates that boron migration occurs via a two step process: from substitutional B with neighboring tetrahedral Si (BI_{tet}) to B in one of 6 hexagonal sites (the subset of 12 hexagonal sites away from the given I_{tet} site) and then back to one of 6 substitutional sites [105, 12]. The B transition state is located between the substitutional site and a hex site along a <311> direction. Fig. 1.1 shows the migration path and corresponding energy barrier. In this work, we assume that the interstitial mediated diffusion mechanism and diffusion path are the same in strained SiGe.

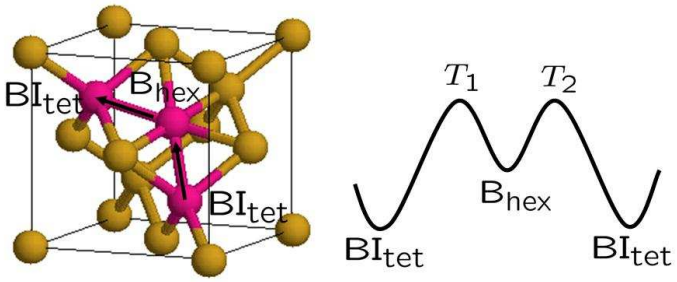

Figure 6.1: BI migration path and corresponding energy barrier. $BI_{tet} \rightarrow B_{hex} \rightarrow BI_{tet}$. B migrates from a substitutional site to one of six hexagonal sites and then one of six sites around hexagonal ring. The migration occurs along <311> directions.

6.3 B diffusivity in strained SiGe

6.3.1 Ge-induced Stress in $Si_{1-x}Ge_x$

Ge atoms in epitaxially grown SiGe layer on top of relaxed Si produce biaxial compressive stress. Although the strain level due to Ge is calculated using Vegard's law (linear interpolation of lattice constant between pure Si and Ge) in many cases, it is well known that the lattice constant of $Si_{1-x}Ge_x$ deviates from Vegard's law [8]. As has been previously observed [106], DFT-GGA overestimates the equilibrium lattice constant for Ge. However, the calculations accurately reproduce the experimental consensus of the negative deviation from Vegard's law, as shown in Fig. 1.2.

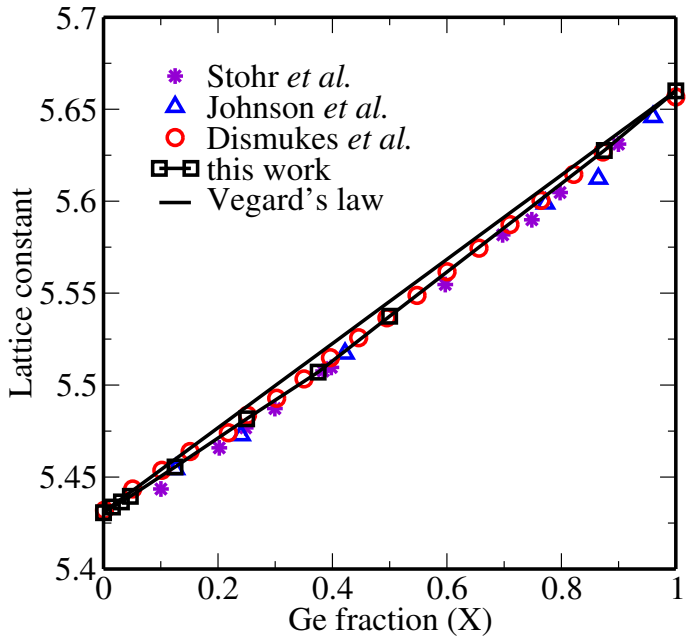

Figure 6.2: Lattice constant of $Si_{1-x}Ge_x$. Ge shows a negative deviation from Vegard's law. DFT-GGA overestimates the lattice constant for Ge so the endpoint values are normalized to experimental values [6, 7, 8] for comparison to intermediate compositions.

The calculated lattice constant of relaxed $Si_{1-x}Ge_x$ is given by

$$a(x) = a_0 + 0.194x + 0.035x^2, \tag{6.1}$$

where a_0 is the equilibrium Si lattice constant of 5.431. In fully strained $Si_{1-x}Ge_x$ on top of relaxed Si, the in-plane lattice constant of $Si_{1-x}Ge_x$ is the same as that of Si and the out-of-plane lattice constant is determined by the biaxial Poisson ratio ($\nu = 2C_{12}/C11$). Then, the applied strain is determined as

$$\begin{aligned} \epsilon_{\parallel}(x) &= \frac{a_0 - a(x)}{a(x)}, \\ &= \frac{-0.194x - 0.035x^2}{5.431 + 0.194x + 0.035x^2}, \\ \epsilon_{\perp}(x) &= -\nu\epsilon_{\parallel}. \end{aligned} \tag{6.2}$$

Although the actual lattice constant at high temperature is larger than the value calculated by Eq. 1.1 due to thermal expansion, the reduced elastic constant compensates the volume expansion and thus the stress energy is nearly temperature independant. The detailed analysis is given in Section 7.3.1.

Table 6.1: Formation energy and binding energy of B-Ge at first nearest neighbor (1NN) spacing and 2NN spacing. Formation energy (E^f) is calculated at equilibrium lattice constant of pure Si and with isolated substitutional impurities as reference. Binding energy (E^b) is calculated with relaxed (lowest energy) lattice constants and thus excludes global strain compensation. Both terms are defined in Eq. 2.32. The 2NN configuration has larger binding energy than other configurations.

	BGe 1NN	BGe 2NN
E^f (eV)	-0.009	-0.038
E^b (eV)	0.016	-0.016

6.3.2 B migration energy in $Si_{1-x}Ge_x$

When B is introduced into a $Si_{1-x}Ge_x$ lattice, B may interact with Ge. In fact, Lever *et al.* proposed B-Ge pairing to explain retarded B diffusion. However, our DFT results show that the B-Ge interaction is minimal (Table 1.1), and B-Ge interaction is even repulsive at 1NN in contrast to Lever's assumption. Thus Lever's scenario can be discarded.

Table 6.2: The induced strains of substitutional B and BI transition state. In BI transition state, the lattice expands in the dominant coordinate of hop.

	B	BI_{trans}
$\Delta\vec{\epsilon}$	(-0.302, -0.302, -0.302)	(0.288, -0.036, -0.036)

Table 6.3: The formation energy difference of the transition state for B diffusion in $Si_{63}Ge$ relative to pure silicon. As Ge moves away from the final destination of B, the formation energy difference decreases. 0NN refers to an interstitial B atom displacing a substitutional Ge to a tetrahedral site (or the reverse process).

1 Ge atom	0NN	1NN	2NN	3NN
ΔE^f (eV)	0.10	0.099	0.047	0.020

Table 6.4: The formation energy change of the transition state for B diffusion with 2 Ge atoms in a hex ring relative to pure silicon. Note that increase in energy of transition state is greatest for the two Ge atoms at 1NN. In *a* configuration, there is a Ge-Ge bond (Fig. 1.4 (c)). But there is no Ge-Ge bond in *b* configuration (Fig. 1.4 (b)).

2 Ge atoms	0-1NN	0-2NN	0-3NN	1-1NN	1-2NN	1-3NN	2-2NN	2-3NN
ΔE^f (eV)	0.28	0.16	0.17	0.48	0.16^a 0.25^b	0.14	0.12	0.11

Table 6.5: The formation energy change of the transition state for B diffusion with 3 Ge atoms in a hex ring relative to pure silicon. In *a* configuration, there is a Ge-Ge bond between 1NN and 2NN, but the 2NN is at the diagonal position to 1NN in *b* configuration.

3 Ge atoms	0-1-1NN	0-1-2NN	0-1-3NN	0-2-2NN	0-2-3NN
ΔE^f	0.53	0.32^a 0.34^b	0.36	0.16	0.24
3 Ge atoms	1-1-2NN	1-1-3NN	1-2-3NN[a]	1-2-2NN	2-2-3NN
ΔE^f	0.53	0.48	0.25^a 0.29^b	0.31	0.19

Table 6.6: The formation energy change of the transition state for B diffusion with 4 Ge atoms in a hex ring relative to pure silicon. In *a* configuration, there is a Ge-Ge bond between 1NN and 2NN, but the 2NN is at the diagonal position to 1NN in *b* configuration.

4 Ge atoms	0-1-1-2NN	0-1-1-3NN	0-1-2-2NN	0-1-2-3NN
ΔE^f	0.53	0.42	0.40	0.36^a 0.38^b
4 Ge atoms	0-2-2-3NN	1-1-2-2NN	1-1-2-3NN	1-2-2-3NN
ΔE^f	0.32	0.52	0.54	0.36

The stress effect on B diffusivity was studied using *ab-initio* methods by Diebel [12]. They reported strong anisotropic diffusivity due to asymmetric induced strain of BI_{trans}. Another possible factor for retarded B diffusion in $Si_{1-x}Ge_x$ is the change in BI_{trans} formation energy due to nearby Ge. To test this proposition, we performed extensive DFT calculations for various local Ge configurations. We find that indeed the BI_{trans} formation energy changes when Ge is closely located, and the dominant effect is due to Ge within the 6-membered ring surrounding target hexagonal site. Figs. 1.3, 1.4, and 1.5 illustrate how the energy barrier changes with different configuration of nearby Ge. Tables 1.3-1.6 summarize the changes in BI_{trans} formation energy when Ge atoms are present in the hexagonal ring where BI migration occurs. When

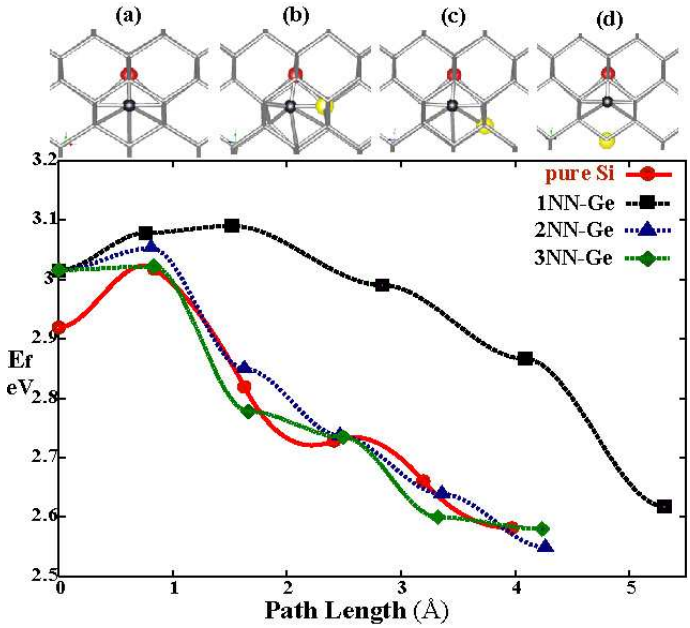

Figure 6.3: The energy along one step of the boron diffusion path ($B_i^{hex} \rightarrow BI^{tet}$) in pure Si and $Si_{63}Ge$. The highest barrier is for Ge at the 0^{th} nearest neighbor (0NN) site (not plotted). 0NN refers to BGe_i^{tet} in which Ge is displaced to a tetrahedral site by B. As Ge moves away from the final B destination, the barrier decreases to the value in pure Si. Note that although the energy of the transition state for Ge in the 3NN site is almost the same as for pure Si, a higher barrier would have been required for B to have initially come from any substitutional site in the hexagonal ring other than the final site in its previous hop.

there is one Ge in a hexagonal ring, the B migration path to 0NN has the highest formation energy. But the path to 1NN has the nearly same formation energy, and the transition state energy approaches that in relaxed Si as the final B position moves away, When there are two Ge atoms in the ring, the total effect is stronger than the sum of individual effects except the 2NN-3NN case. The migration along 1NN-1NN path has the highest formation energy. This trend remains true for three or four Ge atoms in the ring. These results indicate that B prefers the migration paths away from Ge. We calculated the changes in the transition state formation energies for the case of four or less Ge atoms in a ring, and set the values 0.4 eV regardless of the

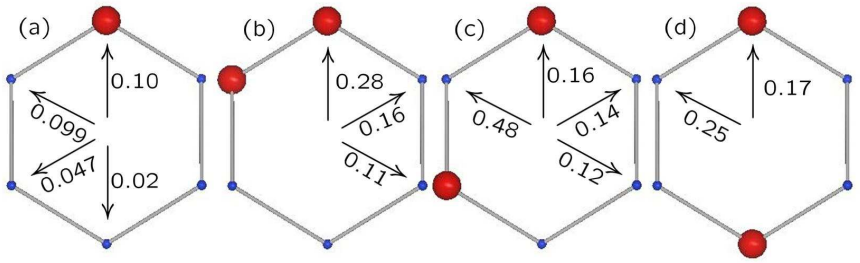

Figure 6.4: The boron diffusion paths and the corresponding changes in formation energies at the transition state with one or two Ge atoms in a hex ring. The farther the final B destination from Ge atoms, the lower the transition state energy is. The change in the formation energy is the highest (left arrow in (c)) with two Ge-atoms at 1NN, and the 2NN-3NN configuration (bottom arrow in (b)) has the lowest energy.

detailed Ge location for other configurations: five or six Ge atoms in a ring. Varying this number doesn't affect the final result because these configurations are rare in the lattice up to 50% Ge concentration and the local Ge configuration effects are weaker than stress effects. We confirmed that the changes in B diffusivity are invariant with any formation energy from 0 eV to 1eV when five or more Ge atoms are in a ring.

The changes in formation energies in the tables include stress energy due to Ge. To separate the local Ge effect from the stress effect, we subtracted the $-V_0\Delta(\vec{\epsilon}_{BI_{trans}} - \Delta\vec{\epsilon}_B)\cdot\mathbf{C}\cdot\vec{\epsilon}(x)$ term from the values in Table 1.3-1.6. Separate calculations confirm that induced strains in SiGeB systems are additive, independent of atomic configuration. The induced strains are listed in Table 1.2.

6.3.3 B diffusion in $Si_{1-x}Ge_x$

In pure Si, the stress-dependent B diffusivity is given by,

$$D_{pq}(\vec{\epsilon}) = \sum_{i=1}^{12}\sum_{j=1}^{6} \nu_0 \exp\left(-\frac{E_i^{f_1}(\vec{\epsilon})}{kT}\right) \frac{\nu_0 \exp\left(-\frac{E_{ij}^{f_2}(\vec{\epsilon})}{kT}\right)}{\sum_{k=1}^{6} \nu_0 \exp\left(-\frac{E_{ik}^{f_2}(\vec{\epsilon})}{kT}\right)} \Delta X_{ij}^p \Delta X_{ij}^q, \qquad (6.3)$$

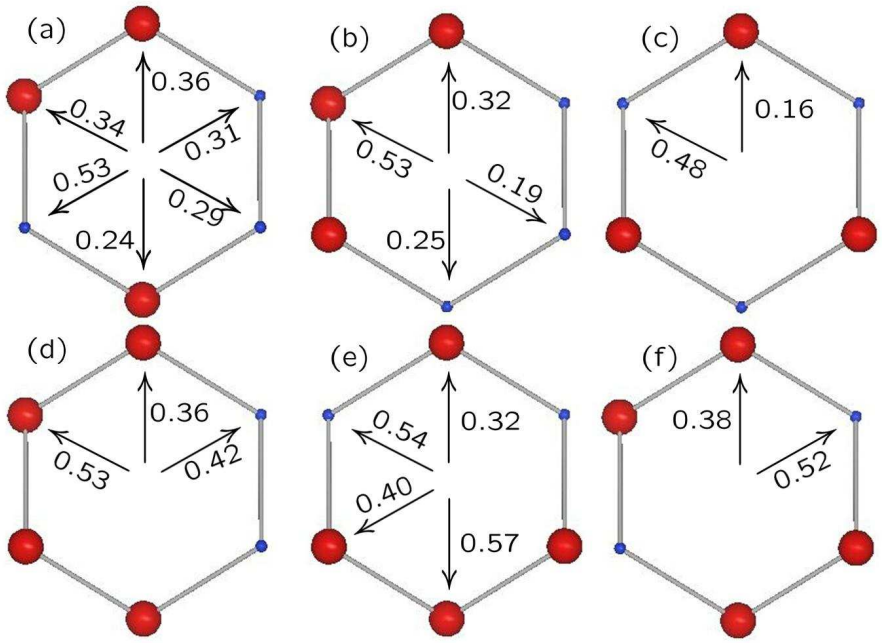

Figure 6.5: The boron diffusion paths and corresponding changes in formation energies at the transition state with three or four Ge atoms in a hex ring. As in the case of two Ge in a ring, whenever two Ge atoms are at 1NN, the migration barrier is the highest in each configuration.

where ν_0 is the attempt frequency, $E_i^{f_1}$ is the formation energy of the first transition state to the i^{th} hexagonal site, $E_{ij}^{f_2}$ is the formation energy of the second transition state to the j^{th} lattice site around the hex site, and ΔX_{ij}^p is the p^{th} component of hopping vector. As for diffusion of B in pure Si [12], we find that all the off-diagonal elements of D_{pq} are all zero.

In Chapter 3, based on this type of equation, we performed KLMC simulations to predict stress effects on dopant diffusivity in Si. However, performing KLMC in an alloy material like $\mathrm{Si}_{1-x}\mathrm{Ge}_x$ is technically more complicated than in pure material since the local alloy configurations and various initial Ge distributions should be taken into account. To make it simple, instead of performing KLMC (tracking the

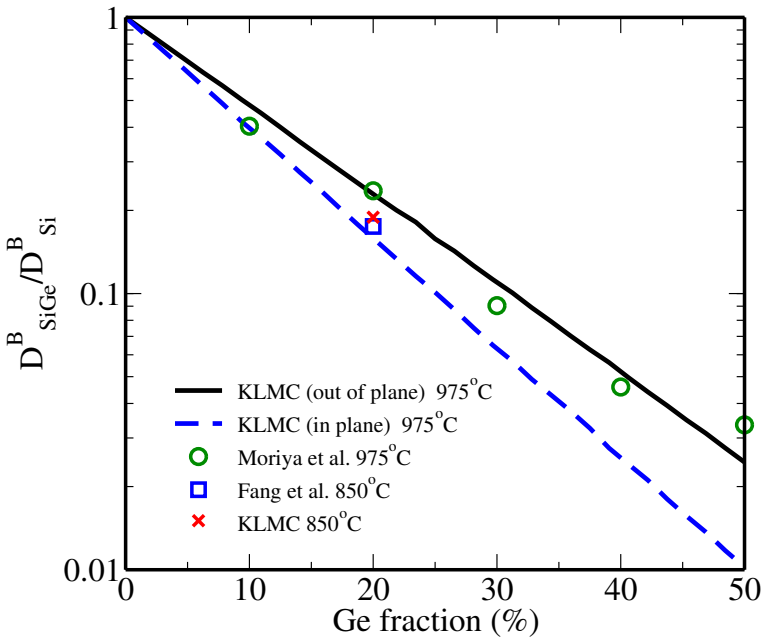

Figure 6.6: B diffusivity in strained SiGe. Note that appropriate comparison for data from Moriya *et al.* is with out-of-plane diffusivity, since diffusion was measured in vertical direction only. Model predictions (out-of-plane) and data were both normalized to 20% Ge result since Moriya reported only relative diffusivity [9]. It can be seen that the calculations do an excellent job of predicting change in B diffusion with Ge fraction. Fang's data at 20% Ge (□) also agrees well with our prediction (**x**) [10].

consecutive hops in the large lattice), we took the statistical average of the diffusivity calculated analytically at every lattice site in a small volume of lattice subject to periodic boundary condition. This is equivalent to KLMC since the main contribution originates from stress effects and the correlation between consecutive hops is weak.

The averaged change in diffusivity is obtained by

$$\frac{\overline{D}^{SiGe}_{pq}(x)}{\overline{D}^{Si}_{pq}} = \frac{\sum_{u=1}^{N_{\text{sample}}} \sum_{v=1}^{64} D^{SiGe}_{uv,pq}(x)}{N_{\text{sample}} \times 64 \times D^{Si}_{pq}(0)}, \tag{6.4}$$

where N_{sample} is the number of samples for different Ge configurations and 64 accounts

for the possible occupation sites of B in a 64-atom supercell. In $Si_{1-x}Ge_x$, the applied strain $\vec{\epsilon}$ is determined by the Ge fraction x (see Eq. 1.2) and the fraction x also determines the local Ge effects on the average. Therefore, the parameter $\vec{\epsilon}$ in Eq. 1.3 changes to x in Eq. 1.4.

When biaxial stress is applied, 4 paths out of the 12 possible paths to nearby hex sites are an out-of-plane transition and the others are an in-plane transition. For the second transition to substitutional sites, 2 paths out of 6 are out-of-plane and the others are in-plane. Then Eq. 1.3 becomes

$$\begin{aligned}
\frac{D_{pq}(x)}{D_{pq}(0)} &= \sum_{i=1}^{4} \frac{\exp\left(-\dfrac{\Delta E_{i,out}^{f_1}(x)}{kT}\right)}{\displaystyle\sum_{k=1}^{6} \exp\left(-\frac{\Delta E_{ik}^{f_2}(x)}{kT}\right)} \left[\sum_{j=1}^{2} \exp\left(-\frac{\Delta E_{ij,out}^{f_2}(x)}{kT}\right) \Delta X_{ij}^{p} \Delta X_{ij}^{q} \right. \\
&\qquad \left. + \sum_{j=3}^{6} \exp\left(-\frac{\Delta E_{i,out}^{f_2}(x)}{kT}\right) \Delta X_{ij}^{p} \Delta X_{ij}^{q}\right] \\
&+ \sum_{i=5}^{12} \frac{\exp\left(-\dfrac{\Delta E_{i,in}^{f_1}(x)}{kT}\right)}{\displaystyle\sum_{k=1}^{6} \exp\left(-\frac{\Delta E_{ik}^{f_2}(x)}{kT}\right)} \left[\sum_{j=1}^{2} \exp\left(-\frac{\Delta E_{ij,out}^{f_2}(x)}{kT}\right) \Delta X_{ij}^{p} \Delta X_{ij}^{q} \right. \\
&\qquad \left. + \sum_{j=3}^{6} \exp\left(-\frac{\Delta E_{i,out}^{f_2}(x)}{kT}\right) \Delta X_{ij}^{p} \Delta X_{ij}^{q}\right]. \quad (6.5)
\end{aligned}$$

Here we assumed the attempt frequency ν_0 is same in both Si and $Si_{1-x}Ge_x$.

Based on Eq. 1.4 and 1.5, we calculated $\overline{D}_{33}$ (out-of-plane) and $\overline{D}_{11}$ (in-plane) since biaxial stress produces anisotropic diffusion. The results were compared with experimental data by Moriya *et al.* [9] and Fang *et al.* [10], shown in Fig. 1.6. The change in in-plane diffusivity is stronger than that of out-of-plane diffusivity, which is consistent with Diebel's prediction [12]. We matched out-of-plane diffusivity with Moriya's at 20% Ge since their data was given in arbitrary units. The theoretical values are in agreement with the experimental results and give an excellent prediction

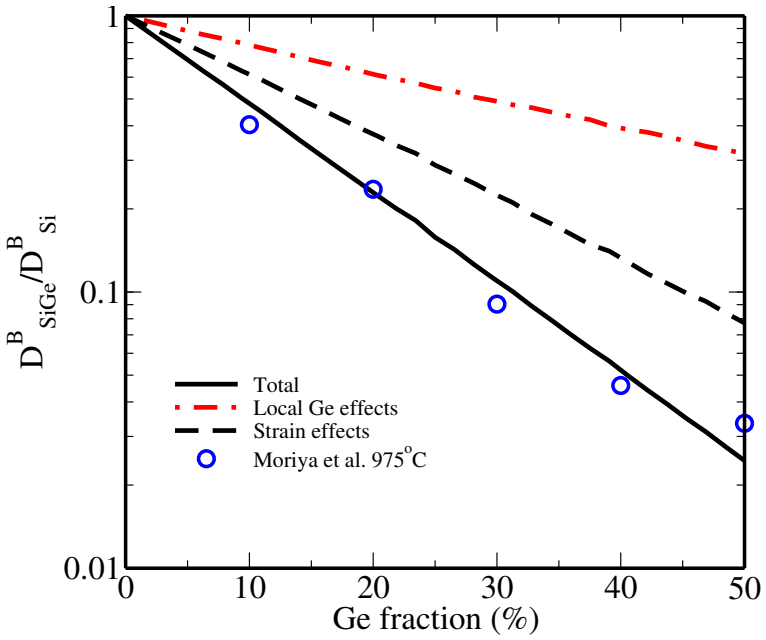

Figure 6.7: Out-of-plane B diffusivity in strained SiGe. The broken line is the Ge effect and the dotted line is the stress effect. Stress effect is somewhat stronger than Ge effect, but both produce significant change in B diffusivity.

of change in diffusivities in strained $Si_{1-x}Ge_x$. Both strain effects and chemical effects are important. However, the chemical effects appear weaker than suggested by data of Kuo *et al.* [45] who varied both composition and strain independently. Similarly the strain effects appear stronger than those extracted by Kuo *et al.* [45], but weaker than those obtained from similar experiments of Zangenberg *et al.* [32]. This may be due to changes in dislocation structure of relaxed SiGe modifying the point defect concentrations in the experiments.

6.4 Summary

We analyzed the complicated B diffusion in strained $Si_{1-x}Ge_x$ alloys using extensive DFT calculations. We found from DFT results that while there is no binding between substitutional B and Ge, Ge in the proximity of B can increase the B migration

barrier. By separating strain and local Ge effects, we developed a predictive model for retarded B diffusion in strained SiGe and found that the B transition state energy depends on local Ge configurations as well as global strain compensation. While both stress effects and local Ge effects are significant, strain effects are somewhat stronger than local Ge effects. B diffusion is strongly anisotropic in strained-$Si_{1-x}Ge_x$ due to the asymmetric transition state. Thus the impact of Ge on out-of-plane diffusivity is weaker than that on in-plane diffusivity.

Chapter 7

DOPANT SEGREGATION AT STRAINED-$Si_{1-X}Ge_X$/Si INTERFACES

In this chapter, dopant (B, P and As) segregation at strained-$Si_{1-x}Ge_x$/Si interfaces is discussed by equilibrating chemical potentials of dopants and electrons on each side of the interface. The theoretical results are then compared with existing experimental data. Our calculations include changes in effective density of states (EDS), with particular attention to high temperature hole effective mass, band gap narrowing due to Ge and temperature, and lattice constant. We find that strong B segregation is dominated by stress effects, while moderate P or As segregation is dominated by changes in electronic properties. We also observe that calculated stress energy is nearly temperature independent.

7.1 Background

In modern ULSI technology, strain engineering is becoming an essential tool to help scale metal oxide field effect transistor (MOSFET) devices, and strained Si has been used in commercial products to enhance the carrier mobility since the 90 nm node [38]. One of the important strain sources is an $Si_{1-x}Ge_x$ expitaxial layer in the source/drain regions of a p-MOSFET.

At the Si/$Si_{1-x}Ge_x$ interface, it has been reported that B segregates into the $Si_{1-x}Ge_x$ region [107, 108, 109, 46, 110, 10] and P or As segregates into Si [108, 2, 111]. To our best knowledge, however, detailed calculations including all the terms required to predict segregation (as in Eqs. 9 and 11 in Ref. [109]) have not been reported. In our previous analysis [40], for example, B segregation was explained based on solely

strain compensation. However, this analysis was oversimplified, and there are other effects arising from changes in electronic properties and entropy of mixing. In this chapter, we investigates segregation ratio quantitatively at the interface of strained-$Si_{1-x}Ge_x$/Si, leading to corrections to a similar previous analysis by Hu [107, 109].

7.2 Free energy and chemical potential

Dopant segregation occurs until the chemical potential μ reaches the same value on both sides of the interface. The segregation ratio k_{seg} is given as a solution of the equation:

$$\mu(k_{seg}N)_{Si_{1-x}Ge_x} = \mu(N)_{Si}, \tag{7.1}$$

where N is dopant concentration. Hu separated the chemical potential into two separate parts: atomic and electronic. In the atomic part, dopant atoms were introduced into Si or $Si_{1-x}Ge_x$ with charge carriers at the intrinsic Fermi level. However, the defect level (donor or acceptor level) is the more proper level in which to introduce charge carriers, and is consistent with subtracting the ionized fraction of dopants in the electronic step. Low temperature behavior further supports this idea, as some charges still remain at the defect level (not at the intrinsic level).

The total free energy of N dopant atoms is given by

$$G \;=\; Nu - V_0 N \Delta\vec{\epsilon}\cdot\mathbf{C}\cdot\vec{\epsilon}(N_{Ge}) - kT\ln(\Omega_a\Omega_e), \tag{7.2}$$

where Nu is the total internal energy of dopants, V_0 is one lattice volume of relaxed $Si_{1-x}Ge_x$, $\mathbf{C}$ is the elastic stiffness tensor, $\Delta\vec{\epsilon}$ is the normalized induced strain due to the dopant, $\vec{\epsilon}(N_{Ge})$ is the applied strain, and Ω_a (Ω_e) is increase in the number of possible configurations of atoms (electrons) due to the dopant. The second term is the generalized stress energy ($\theta\beta\beta_{Ge}NN_{Ge}$ in Refs. [107, 108, 109]) under normal stress

conditions. For simplicity, we will describe it as NE^s. $\Delta\vec{\epsilon}$ values for various dopants are listed in Table 7.2, and the applied strain is determined assuming pseudomorphic growth conditions. The internal energy is the sum of electric potential energies of ions and free charge carriers, and binding energies:

$$Nu = -fNZe\psi + N\bar{E}^b + (1-f)NE_d + (n-n_i)E_c - (p-p_i)E_v, \quad (7.3)$$

where ψ is electric potential, f is the ionized fraction of the dopant, Z is the charge state of the dopant, n_i and p_i are intrinsic carrier concentrations, $\bar{E}^b$ ($\sim E^b N^{paired}/N$) is the averaged binding energy of dopant-Ge pairs, n (p) is the electron (hole) concentration, and E_c (E_v) is the conduction band minimum (valence band maximum). Averaged binding energy rather than direct binding energy should be used since the pairing probability is less than 1. In Eq. 7.3, the first term is the electric potential energy of the ion, and the last three terms are electron energy.

The number of possible configurations is given by

$$\begin{aligned}
\Omega_a &= \frac{\Omega_a^{Total}(N)}{\Omega_a(0)} \\
&= \begin{cases} \dfrac{N_L!}{N!N_{Ge}!(N_L-N_{Ge}-N)!}\dfrac{(N_L-N_{Ge})!N_{Ge}!}{N_L!} & \text{for B;} \\ \dfrac{N_L!}{N!(N_L-N)!}\dfrac{(N_L-N_{Ge})!N_{Ge}!}{N_L!} & \text{for P and As,} \end{cases} \quad (7.4) \\
\Omega_e &= \frac{\Omega_e^{Total}(N)}{\Omega_e(0)} \\
&= \frac{N_c!}{n!(N_c-n)!}\frac{N_v!}{p!(N_v-p)!}\frac{N!}{(fN)![(1-f)N]!} \times g^{Z(1-f)N} \\
&\qquad \times \frac{n_i!(N_c-n_i)!}{N_c!}\frac{p_i!(N_v-p_i)!}{N_v!}, \quad (7.5)
\end{aligned}$$

where N_L is the lattice concentration, N_{Ge} is Ge concentration, N_c (N_v) is the electron (hole) effective density of states, and g is the electron spin degeneracy. In counting the number of possible atomic configurations in Eq. 7.4, we assumed that B can replace

only Si not Ge, which is supported by highly suppressed BI complex formation with Ge [39]. Conversely, P or As diffusivity in strained $Si_{1-x}Ge_x$ is slightly higher than in Si [77, 2], which implies that dopants can replace Ge sites without restriction. To account for this, we introduced $\tilde{Z} = (1-Z)/2$. When charge neutrality ($n-p-ZfN = 0$) and full ionization ($f = 1$) are assumed within Maxwell-Boltzmann statistics, then

$$nE_c - pE_v + kT \ln \Omega_e^{Total}(N) = NE_F, \tag{7.6}$$

where E_F is the Fermi energy. When $N = 0$, $n_i E_c - p_i E_v + kT \ln \Omega_e(0) = 0$. Thus Eq. 7.2 is simplified to

$$G = N \left(-Ze\psi + ZE_F + \bar{E^b} + E^s + kT \ln \frac{N}{N_L - \tilde{Z} N_{Ge}} \right). \tag{7.7}$$

Finally, the electrochemical potential of the dopant is given as the derivative of G with respect to N:

$$\begin{aligned} \mu &= -Ze\psi - NZe\psi' + ZE_F + ZNE_F' + \bar{E^b} + E^s \\ &\qquad + kT \ln \frac{N}{N_L - \tilde{Z} N_{Ge}} + kT \qquad (7.8) \\ &= -Ze\psi + ZE_F + \bar{E^b} + E^s + kT \ln \frac{N}{N_L - \tilde{Z} N_{Ge}} + kT. \qquad (7.9) \end{aligned}$$

In Eq. 7.8, the derivative of built-in potential cancels out the derivative of the Fermi energy.

7.3 Segregation ratio

7.3.1 Derivation of segregation ratio

Selecting a reference energy is important in using Eq. 7.9 in Eq. 7.1. Although Hu [108] used undoped low temperature $Si_{1-x}Ge_x$/Si heterostructure band alignment (Fig. 7.1 (a)) to account for a part of the difference in electron energy, the electron energy is a

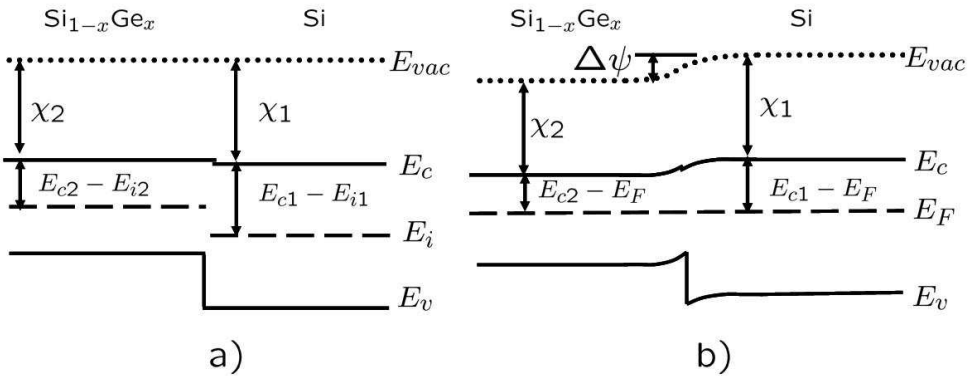

Figure 7.1: Band alignment at strained-$Si_{1-x}Ge_x$/Si interface without band bending (a), and with band bending (b). Charge neutrality breaks down near the junction due to different work functions in each side unless all the charges are frozen. This builds up an electric potential and causes a band bending across the junction.

constant across the interface because band bending occurs to match the Fermi level in both regions within the order of the Debye length $\sqrt{\epsilon_{\rm Si} kT/q^2 N}$. Within a short distance on the order of the Debye length from the interface, charge neutrality does not hold, and thus Eq. 7.6 is not valid. However, the Debye length is only on the order of 1 nm at 900°C and 5×10^{19} cm^{-3}, which is the experimental condition in Hu *et al.* [108] and Moriya *et al.* [110]. Thus Fig. 7.1 (b) is the proper band alignment and our description of electron energy is valid.

Eqs. 7.1 and 7.9 can be combined to yield the segregation ratio:

$$k_{seg} = (1 - \tilde{Z}x) \exp\left(\frac{Ze\Delta\psi - \Delta\bar{E}^b - \Delta E^s}{kT}\right), \tag{7.10}$$

where x is the Ge fraction. Δ indicates the difference between region 2 ($Si_{1-x}Ge_x$) and 1 (Si) throughout this chapter with the exception of $\Delta\epsilon$. The built-in potential term $e\Delta\psi$ is an implicit function of k_{seg} and it is given by

$$e\Delta\psi = \Delta\chi + \Delta(E_c - E_F) = \Delta\chi + kT \ln \frac{N_{c2}}{n_2}\frac{n_1}{N_{c1}}, \tag{7.11}$$

where χ is the electron affinity.

We use a numerical solution of Eq. 7.10 to compare our calculations with experiments. However, the two limiting cases determined by the ratio between dopant concentration and intrinsic carrier density provide a guide for the range of segregation ratios. Under intrinsic conditions $n \sim p \sim n_i = \sqrt{N_c N_v \exp(-E_g/kT)}$. Therefore, the intrinsic segregation ratio is given as

$$k_{seg} = (1-\tilde{Z}x)\left(\frac{N_{c2}N_{v1}}{N_{c1}N_{v2}}\right)^{Z/2} \exp\left(\frac{Z\Delta\chi - \Delta\bar{E}^b - \Delta E^s + Z\Delta E_g/2}{kT}\right). \quad (7.12)$$

Under extrinsic conditions, n_1/n_2 becomes $1/k_{seg}$ for n-type or $k_{seg}\times N_{c1}N_{v1}/(N_{c2}N_{v2})\times \exp(\Delta E_g/kT)$ for p-type combined with $n_i^2 = np$. Applying these results in Eq. 7.10 yields the extrinsic segregation ratio:

$$k_{seg} = \begin{cases} \sqrt{(1-\tilde{Z}x)\dfrac{N_{c2}}{N_{c1}}}\exp\left(\dfrac{Z\Delta\chi - \Delta\bar{E}^b - \Delta E^s - \tilde{Z}\Delta E_g}{2kT}\right) & \mathrm{n-type} \\ \sqrt{(1-\tilde{Z}x)\dfrac{N_{v2}}{N_{v1}}}\exp\left(\dfrac{Z\Delta\chi - \Delta\bar{E}^b - \Delta E^s - \tilde{Z}\Delta E_g}{2kT}\right) & \mathrm{p-type,} \end{cases} \quad (7.13)$$

For p-type material N_v replaces N_c in Eq. 7.13. Note that $\tilde{Z}\Delta E_g$ is used instead of $Z\Delta E_g$ in extrinsic case.

7.3.2 Effective density of states

The first significant factor in segregation is the change in EDS (N_c and N_v). As more Ge is incorporated, EDS decreases since Ge-induced strain removes degeneracy of the band structure. When compressive biaxial stress is applied, the electron density of states at room temperature rapidly decreases to 2/3 of the unstressed value because compressive biaxial stress lowers the energy of 4 out of 6 conduction band minima.

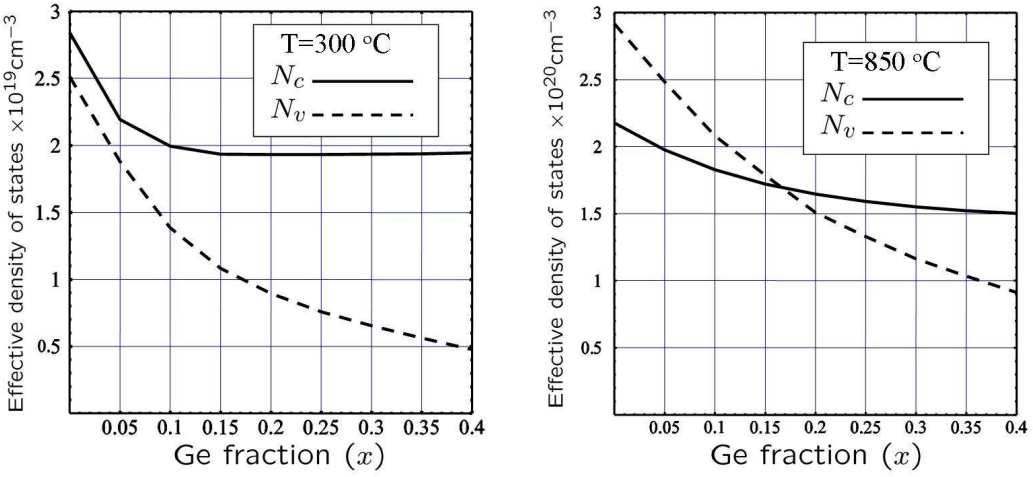

(a) EDS at room temperature

(b) EDS at 850°C

Figure 7.2: Effective density of states in $Si_{1-x}Ge_x$. Biaxial compressive stress reduces 6-fold degeneracy of conduction band minima to 4-fold degeneracy, thus electron EDS of $Si_{1-x}Ge_x$ is roughly 2/3 of pure Si. However, hole EDS decreases continually as more Ge is added. High temperature electron EDS decreases slower than the room temperature value due to thermal smearing.

We calculated high temperature N_c value based on Eq. 22 and Table 1 in Ref. [44]:

$$N_c = 2 \times \left[g_1 + g_2 \exp\left(-\frac{\Delta E_{c,split}}{kT} \right) \right] \times \left(\frac{mkT}{2\pi\hbar^2} \right)^{\frac{3}{2}}, \tag{7.14}$$

where g_1 (g_2) is the degeneracy of the lowered (raised) conduction band minima. In compressively strained $Si_{1-x}Ge_x$, g_1=4 and g_2=2. Since the electron density of states (DOS) mass is almost constant with varying Ge fraction [112] and temperature [113], Eq. 7.14 is still valid in $Si_{1-x}Ge_x$ at high temperature. $\Delta E_{c,split}$ is the energy splitting of the conduction band at the Δ valley. It can be determined by the uniaxial

deformation potential Ξ_u [114]:

$$\begin{aligned}
\Delta E_{c,split} &= \Delta E_c^{001} - \Delta E_c^{100,010} && (7.15)\\
&= \frac{2}{3}\Xi_u^{\Delta}(\epsilon_\perp - \epsilon_\parallel) - \left(-\frac{1}{3}\Xi_u^{\Delta}(\epsilon_\perp - \epsilon_\parallel)\right) && (7.16)\\
&= \Xi_u^{\Delta}(\epsilon_\perp - \epsilon_\parallel). && (7.17)
\end{aligned}$$

The hole EDS, N_v, can be obtained in a similar way to N_c:

$$N_v = 2 \times \left[m_r^{3/2} + m_l^{3/2} \exp\left(-\frac{\Delta E_{v,split}}{kT}\right)\right] \times \left(\frac{kT}{2\pi\hbar^2}\right)^{\frac{3}{2}}, \qquad (7.18)$$

where m_r (m_l) is the hole EDS mass of the raised (lowered) bands, and $\Delta E_{v,split}$ is the valence band splitting at the Γ point:

$$\begin{aligned}
\Delta E_{v,split} &= \Delta E_{v2} - \Delta E_{v1} && (7.19)\\
&= \left[\frac{1}{3}\Delta_0 - \frac{1}{2}\delta E\right] \\
&\quad - \left[-\frac{1}{6}\Delta_0 + \frac{1}{4}\delta E + \frac{1}{2}\left[\Delta_0^2 + \Delta_0\delta E + \frac{9}{4}(\delta E)^2\right]^{\frac{1}{2}}\right] && (7.20)\\
&= \frac{1}{2}\Delta_0 - \frac{3}{4}\delta E - \frac{1}{2}\left[\Delta_0^2 + \Delta_0\delta E + \frac{9}{4}(\delta E)^2\right]^{\frac{1}{2}}, && (7.21)
\end{aligned}$$

where Δ_0 is the spin-orbit splitting, and $\delta E = 2b(\epsilon_\perp - \epsilon_\parallel)$ with the uniaxial deformation potential b. The $v2$ band is a pure $|\frac{3}{2}, \frac{3}{2}>$ state and the $v1$ band is the mixture of $|\frac{3}{2}, \frac{3}{2}>$ and $|\frac{1}{2}, \frac{1}{2}>$ states. The parameters used in the calculations are summarized in Table 7.1.

The hole EDS equation (Eq. 7.18) looks similar to the electron EDS equation (Eq. 7.14). However, the hole EDS varies in a more complicated way due to non-parabolicity of the bands. Since no hole EDS data has been reported at high temperature, we calculated high temperature hole EDS by integrating the density of states

Table 7.1: The parameters used to calculate effective density of states.

	Si	Ge
Ξ_u [114]	9.16	9.42
Δ_0 [114]	0.04	0.3
b [115, 44]	-1.5	-2.2

(DOS) mass provided by Fu *et al.* [116].

$$E = \frac{\hbar^2 k^2}{2m_{DOS}(E)} \tag{7.22}$$

$$m^{3/2} = \frac{1}{(kT)^{3/2}F_{1/2}(\frac{E_F}{kT})}\int_0^\infty \frac{m_{DOS}^{3/2}(E)E^{1/2}}{1+\exp\left(\frac{E-E_F}{kT}\right)}dE, \tag{7.23}$$

where m_{DOS} is the density of states effective mass, and $F_{1/2}$ is the Fermi integral of order 1/2. In Eq. 7.18, m_r and m_l are defined in a way to include the non-parabolicity. The results are plotted in Fig. 7.2. At both room and high temperatures, the hole EDS varies across a wider range than the electron EDS. As expected, the electron EDS converges to 2/3 of the unstrained value at a high Ge fraction.

7.3.3 Band gap narrowing

The second significant factor in the segregation equations (Eqs. 7.12 and 7.13) is the band gap narrowing in strained $Si_{1-x}Ge_x$. There have been many experimental measurements of the band gap in strained-$Si_{1-x}Ge_x$ and Yang *et al.* summarized the results in Ref. [44]. When $x < 0.40$, the deviation among data is small and Yang *et al.* suggested $-0.896x + 0.396x^2$ for ΔE_g, which was used in our segregation calculations. Since the band structure of strained-$Si_{1-x}Ge_x$ is similar to that of Si and has similar temperature dependence to Si [44], ΔE_g is temperature independent at practical Ge concentrations of interest. The intrinsic carrier density can be determined as a function of Ge fraction $n_i(x)$ by combining EDS and E_g and it is plotted in

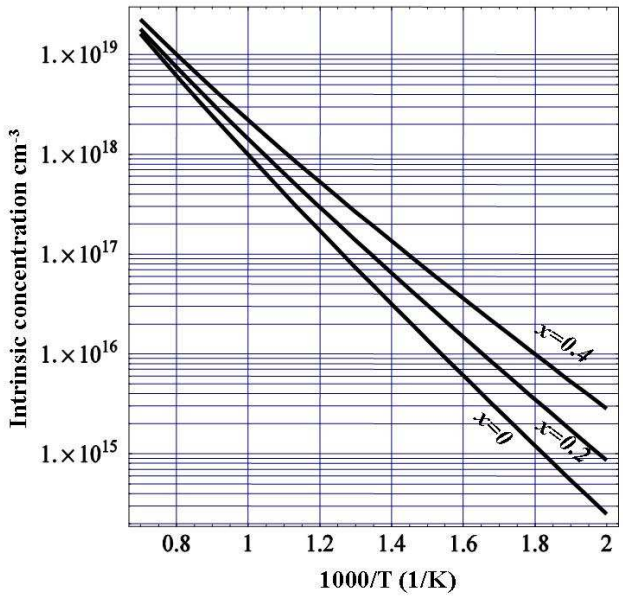

Figure 7.3: Intrinsic carrier concentration in $Si_{1-x}Ge_x$.

Fig. 7.3.

7.3.4 Stress energy

The last major factor in segregation ratio is the stress energy. The key parameter in stress energy, the induced strain $\Delta\vec{\epsilon}$, was calculated using the density functional theory (DFT) code VASP [58, 59, 60]. For B and P, the calculated values agree well with experimental data, but for As, the theoretical value has the opposite sign to the experimental value by Cargill *et al.* [18] (Table 7.2). However, the absolute difference is small and the discrepancy can be explained by the existence of As-vacancy complexes, as discussed in Section 4.3.

The applied strain in biaxially stressed $Si_{1-x}Ge_x$ is a function of the Ge fraction

Table 7.2: Induced strains due to dopants. The values in parenthesis are experimental data. [a] Ref. [19], [b] Ref. [18], [c] Ref. [20]

	P	As	B
$\Delta\epsilon$	-0.08	0.018	-0.302
$\beta(\ \times 10^{-24}\ \mathrm{cm}^3)$	-1.6 (-1.9[a])	0.36 (-0.4[b])	-6.04 (-6.3[c])

x as well as temperature, and it is given as

$$\epsilon_{\parallel}(x,T) = \frac{a_{Si}(T) - a_{Si_{1-x}Ge_x}(T)}{a_{Si_{1-x}Ge_x}(T)}, \tag{7.24}$$

$$\epsilon_{\perp}(x,T) = -2\frac{C_{12}(x,T)}{C_{11}(x,T)}\epsilon_{\parallel}(x,T), \tag{7.25}$$

where $\epsilon_{\parallel}$ ($\epsilon_{\perp}$) is in- (out-of-) plane strain, and $a(x,T)$ is the lattice constant of $Si_{1-x}Ge_x$, which is given by

$$a(x,T) = a_0(x)\left(1 + \int_{298}^{T}\alpha(x,T')dT'\right), \tag{7.26}$$

where $\alpha(x,T)$ is the linear expansion coefficient, which was taken from Ref. [117]. The room temperature lattice constant $a_0(x)$ was obtained from Ref. [118]. Combining the temperature dependence of the Si elastic constant [119] with the Ge concentration dependence [118], we also estimated elastic constants $C_{11}(x,T)$ and $C_{12}(x,T)$ as,

$$C_{11}(x,T) = (165.8 - 37.3x - 0.0128T)\mathrm{GPa}, \tag{7.27}$$

$$C_{12}(x,T) = (63.9 - 15.6x - 0.00480T)\mathrm{GPa}. \tag{7.28}$$

In previous Chapters, we calculated the stress energy ($-V_0\Delta\vec{\epsilon}\cdot\mathbf{C}\cdot\vec{\epsilon}(x)$) based on the assumption that V_0 and $\mathbf{C}$ are a constant and $\vec{\epsilon}(x)$ is independent of temperature. Although $\vec{\epsilon}$ is nearly temperature-independent because the same thermal expansion coefficient is used for a_{Si} and $a_{Si_{1-x}Ge_x}$, the lattice volume and elastic constants are

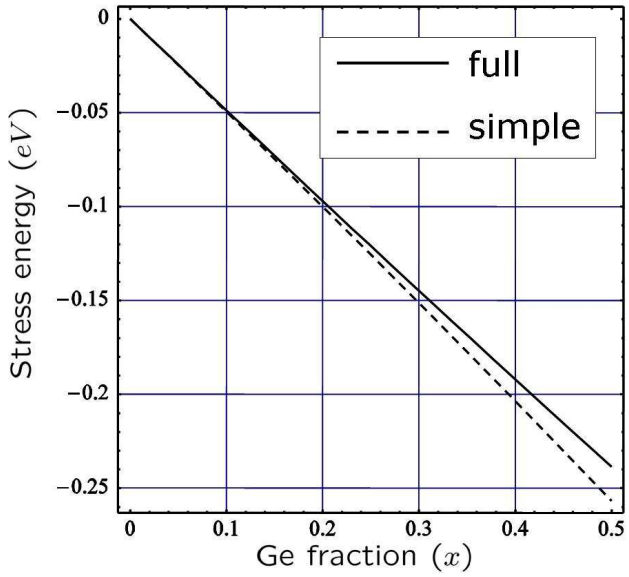

Figure 7.4: Stress energy with varying V_0 and $\mathbf{C}$ (solid line) and stress energy with constant V_0 and $\mathbf{C}$ (broken line).

subject to change with varying x and T. We tested whether the full consideration of temperature and Ge fraction for all the parameters in the stress energy equation $(-V_0(x,T)\Delta\vec{\epsilon}\cdot\mathbf{C}(x,T)\cdot\vec{\epsilon}(x,T))$ made a significant change to our previous results. Fig. 7.4 compares the stress energy from the simplified equation to the stress energy from the full equation for substitutional B. Even when the dopant produces a large induced strain as with B, the result is nearly unchanged. This indicates that the effects of increased lattice volumes compensate the effects of the reduced elastic constant. Thus all the work using the simple version of stress energy in the previous Chapters is still valid.

7.3.5 Binding energy and electron affinity

The binding energies are calculated using DFT. For all three cases (i.e., B-Ge, P-Ge, and As-Ge) the magnitude of direct binding energy was less than a couple tens of

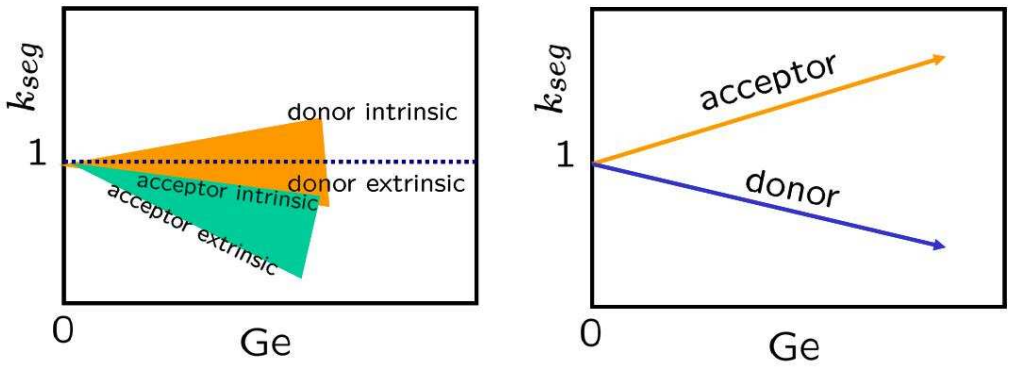

Figure 7.5: Left: Schematic plot of the effects of EDS on dopant segregation as a function of Ge fraction. The reduced EDS in $Si_{1-x}Ge_x$ always makes acceptors segregate into Si, but it depends on doping condition for donors. Right: Schematic plot of the effects of reduced bandgap on segregation ratio as a function of Ge fraction. The smaller bandgap of $Si_{1-x}Ge_x$ helps acceptors segregate into Ge, but it is the opposite for donors.

meV, and thus averaged binding energy can be ignored in our calculations.

The last factor, $\Delta\chi$, is $-\Delta E_c$ in undoped conditions as seen in Fig. 7.1(a). While theoretical calculations using $\vec{k} \cdot \vec{p}$ methods and deformation potential predicted type-I alignment when $x < 0.4$ [114, 120], there is growing evidence that strained-$Si_{1-x}Ge_x$/Si forms type-II alignment via exciton energy measurements and calculations[121, 122, 123, 124, 125]. However, regardless of the type of alignment, the magnitude is small and the impact of electron affinity on segregation is minimal. We linearly interpolated the value at $x = 0.48$ provided by Ni *et al.* [121], which is more conservative than that by Penn *et al.* [124]: $\Delta\chi(x) = -0.0625x$.

7.4 Dopant segregation

The three major factors in the segregation ratio (Eqs. 7.12 and 7.13) are effective density of states, band gap, and stress energy.

(a) Effective density of states

As shown in Fig. 7.2, the change in electron EDS is much less than that in hole EDS. This difference causes B (P and As) to segregate out of (into) strained $Si_{1-x}Ge_x$ under intrinsic doping conditions (Eq. 7.12). Under extrinsic conditions, changes in EDS cause both types of dopants to segregate out of strained $Si_{1-x}Ge_x$, but the effect is weaker for donors due to slowly varying electron EDS.

(b) ΔE_g

The electric field due to the reduced band gap of $Si_{1-x}Ge_x$ results in the opposite type of intrinsic segregation for donors and acceptors, and it has the strongest effect on intrinsic donor segregation into Si. However, the band gap difference makes a minimal impact on extrinsic donor segregation due to aligned conduction band. For acceptors, a large built-in potential is formed since band alignment occurs at the valence band maximum, and thus it causes B segregation into $Si_{1-x}Ge_x$.

(c) Stress energy

Unlike the two factors above, strain compensation is dependent on not only the type of dopant, but the dopant size. Consequently, it is the largest factor for the small B atom due to a large negative induced strain (Table 7.2), and it causes B to segregate into the Ge rich region. On the other hand, strain compensation is much weaker for P and As and electric field effects overwhelm stress effects and result in segregation into Si.

7.4.1 Donor segregation

The atomic size of P is smaller than that of Si, thus P can release stress energy in strained-$Si_{1-x}Ge_x$. However, strain compensation is not strong enough to overcome the other effects. Fig. 7.6 shows a comparison between our calculations and

experimental results for P segregation. The calculated segregation ratio predicts segregation out of strained SiGe, as seen in experiments, but underestimates the extent of segregation. At least some of this difference may be due to issues related to the experiments. In particular, we can note that differences between Christensen *et al.* and our intrinsic value become larger as the Ge fraction increases. If partial relaxation had occurred as they reported [2], stress energy would be reduced and stronger segregation into Si would be expected. In addition, a Si capping layer on top of partially relaxed $Si_{1-x}Ge_x$ experiences lattice expansion, thus the strained-$Si_{1-x}Ge_x$/Si description should be shifted somewhat toward strained-Si/relaxed-$Si_{1-x}Ge_x$. In the latter case, the electron affinity increase due to conduction band lowering [44, 126] overwhelms smaller difference in the band gap in Eq. 7.12, and the prefactor in Eq. 7.12 is lowered as compared with the former case.

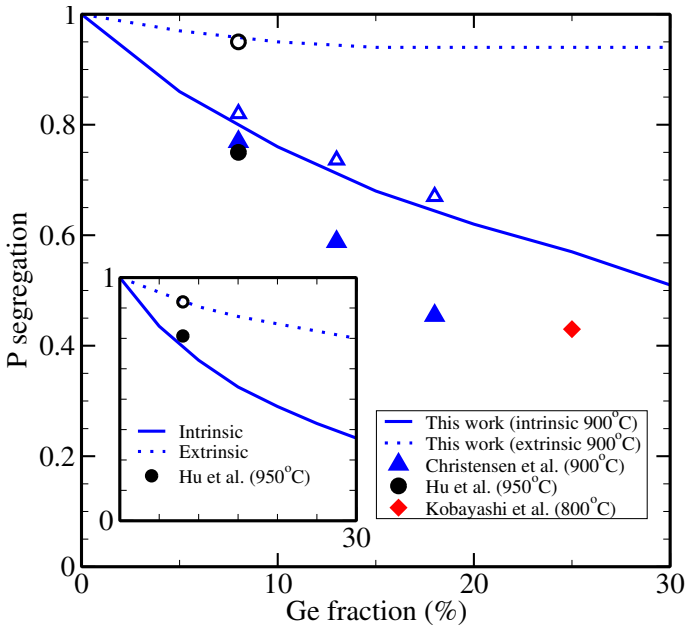

Figure 7.6: P segregation ratio at strained-$Si_{1-x}Ge_x$/Si interface. Filled symbols represent experimental values and open symbols represent corresponding theoretical values. The predicted value for Kobayashi *et al.* is not given because their experimental conditions were beyond the Maxwell-Boltzmann regime. Inset shows As segregation ratio at 950°C.

Hu's extrinsic data is even lower than Christensen's intrinsic result and looks inconsistent with the trend [108]. Combined with higher P diffusivity in strained $Si_{1-x}Ge_x$ [2], the strong gradient in the P concentration can enhance uncertainty in segregation measurements. Kobayashi's result deviates greatly from the theoretical calculation and this can be attributed to partial lattice relaxation in such a thick (160−400 nm) $Si_{0.75}Ge_{0.25}$ layer and a slow chemical potential increase due to partial activation in the Si layer. Partial activation arises when N is near $2 \times 10^{20}\text{cm}^{-3}$ [4] and it reduces the chemical potential with the fractional contribution of the electric potential energy of the ion (see Eq. 7.9). However, quantitative analysis is beyond the scope of this work since Maxwell-Boltzmann statistics already fail when $N \sim n \sim N_{c1}$. In inset of Fig. 7.6, we also compared the As segregation ratio with Hu *et al.* [108]. The measured value is lower than the calculated value possibly due to ignoring the higher As diffusivity in strained $Si_{1-x}Ge_x$ [77] than in Si. Due to the small induced strain of As, minimal strain compensation and thus stronger segregation than P is expected.

7.4.2 Acceptor segregation

In acceptor-doped semiconductors, the majority charge carriers are holes, thus Z is changed to -1. Combined with large stress effects, the result is B segregation into the $Si_{1-x}Ge_x$ layer. Fig. 7.7 shows a comparison between our prediction and measured values for B segregation. Overall, the prediction appears quite good, with the calculations generally predicting slightly more segregation into the strained SiGe than observed experimentally. The largest difference is for Fang's result with a low B concentration ($C_B \sim 3 \times 10^{17}\text{cm}^{-3}$ in Si region), which is much smaller than our calculation. This large difference is partially due to the narrowness of the $Si_{1-x}Ge_x$ layer. In their experiment, the Debye length is about 11 nm, but the half width of the $Si_{1-x}Ge_x$ layer is 15 nm. Therefore, the band is not flat even at the center of the $Si_{1-x}Ge_x$ layer and the built-in potential is not fully developed accordingly.

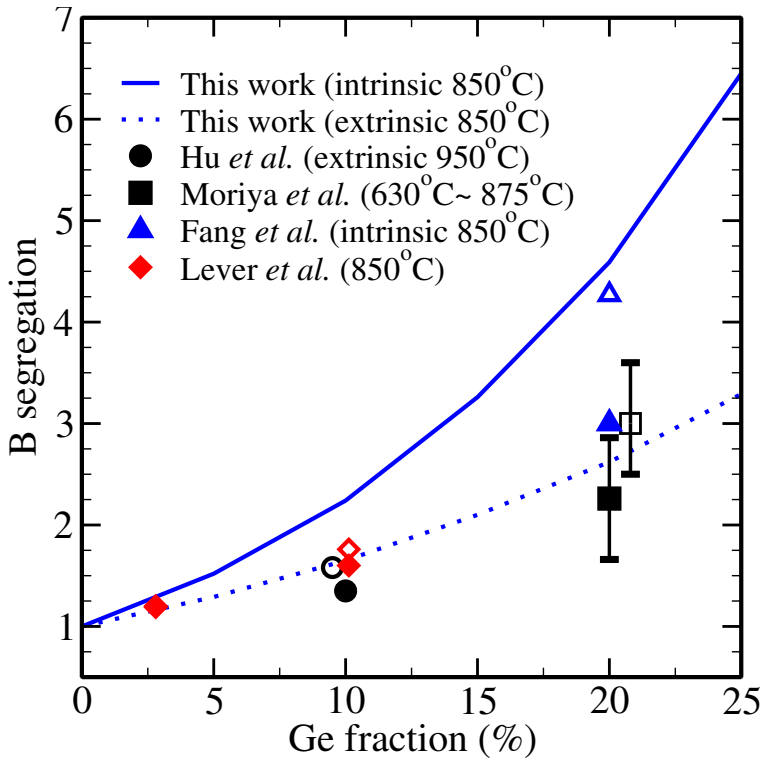

Figure 7.7: B segregation ratio at strained-$Si_{1-x}Ge_x$/Si interface. Filled (open) symbols represent measured (predicted) values. At low Ge concentration (3% Ge), Lever's data and predicted value overlap. The error bar with open square is for comparison to Moriya's data at various temperatures. For better visibility, predicted values for Hu and Moriya are plotted with a small offset in Ge concentration.

Under such conditions, a $Si_{1-x}Ge_x$ epi-layer that is several times thicker is desirable for segregation measurement.

The B concentration in Lever *et al.* is comparable to the intrinsic carrier density, thus the segregation ratio is between the intrinsic and extrinsic curves. Hu's result shows quite good agreement with our prediction [108]. Since Moriya *et al.* measured segregation at various temperatures in $Si_{0.8}Ge_{0.2}$, their data is shown as an error bar in Fig. 7.7. For better visibility, we plotted the theoretical prediction for Moriya *et al.* and Hu *et al.* with small offset on the x axis. In B segregation, stress effects are

dominant, but the change in the band structure still has a significant effect.

7.5 Summary

In summary, we calculated the dopant segregation ratio at strained-$Si_{1-x}Ge_x$/Si interface by considering band alignment, band gap narrowing due to biaxial compressive stress, effective density of states, and stress energy as a function of Ge fraction and temperature. The stress effect is the dominant factor for B segregation, while electronic effects, such as change in band structure and entropy of mixing, are dominant for P and As. A detailed consideration of the temperature dependence of the elastic constant and lattice constant produces a minimal impact on stress energy. To achieve better results, we suggest a similar experiment to Fang *et al.* with a $Si_{1-x}Ge_x$ layer that is several times thicker.

Chapter 8

SUMMARY AND SUGGESTIONS FOR FUTURE WORK

In this dissertation, we explored various promising techniques to enhance ultra shallow junction (USJ) formation. Based on key parameters (induced strain and binding energy) obtained by using *ab-initio* methods, we predicted stress effects on dopant diffusivity and activation, and calculated the pairing coefficient between co-dopants and the segregation ratio at the interface of Si/strained-$Si_{1-x}Ge_x$. Extensive DFT calculations were used to explain retarded B diffusion in strained $Si_{1-x}Ge_x$, which has been a controversial issue for more than a decade. In this chapter, we summarize the work presented in this dissertation, and conclude with suggestions for future work.

8.1 Summary

This dissertation contributes to the advancement of Si technology in three main areas: stress effects on dopant diffusion/activation, codoping effects, and dopant behavior in SiGe. In the following sections, our primary achievements are summarized by topic.

8.1.1 Stress effects on dopant diffusion and activation

(a) Vacancy mediated As diffusion has a stronger stress dependence than interstitial mediated As diffusion, and thus As diffusivity undergoes an enhancement under biaxial compressive stress but little change under tensile stress.

(b) It was confirmed that the lowest energy PI structure is the X_2 named by Liu *et al.* [11]. P diffusion requires two distinct migration paths: inter-ring

transition (0.1 eV) and intra-ring transition (0.2 eV). Asymmetric PI transition states result in anisotropic diffusion under biaxial stress.

(c) Stress effects on dopant-vacancy pairs are universal due to the similarity in transition states and the additive nature of induced strains.

(d) Ga and In have similar diffusion paths, and the stress effects on diffusivity are isotropic even under anisotropic stress.

8.1.2 Dopant-dopant interaction

(a) The attractive binding of B-In pairs originates from localized holes and it is detrimental to dopant activation.

(b) Strong binding between P and In/Ga can enhance the solubility of both dopants, and the large pairing coefficient between P-In/Ga suggests an enhancement in dopant activation via multiple binding.

8.1.3 Dopant diffusion and segregation in SiGe

(a) Retarded B diffusion in strained SiGe is due to global stress effects and local Ge effects. The latter is weaker than the former, but still significant.

(b) The dopant segregation ratio equation at the interface of Si/strained-SiGe was derived by considering the detailed electronic properties of strained SiGe. The three main contributions are effective density of states, band gap, and stress energy.

(c) Acceptors segregate into SiGe and donors out of SiGe.

8.2 Suggestions for future work

In this work, we mainly focused on point defect and small clusters. However, extended defects (e.g., {311} defects and dislocation loops) can be created during process near end of range (EOR) regions or highly stressed regions. These defects are detrimental to MOSFET scaling since they degrade the performance and reliability of devices. As computing power grows rapidly in accordance with the advance in silicon technology, the accessible system sizes and time scales for DFT calculations are continually expanding. As a consequence, large defects such as {311} defects and dislocation loops come into the scope of DFT calculations. The stress energy model we used in this work can be extended to these defects. In this case, induced strains have shear components and thus we should treat the stress energy equation as a full tensor equation. Preliminary work on extended defects found that {311} defects are favored over dislocation loops when a small number of interstitials are involved and there is a crossover point as the number of interstitials increases. It would be of great interest to perform KLMC simulations of comprehensive defect evolution models including small I/V clusters, {311} defects, and dislocation loops.

As shown in Chapter 4, the active As concentration is different from the total chemical As concentration at high doping conditions and it is limited by As-V clustering. Another n-type dopant, P, also shows a similar active vs. total P concentration curve [4]. Combined, the similar P-V biding energy to As-V binding energy suggests that both As and P deactivation kinetics are alike. However, the significant negative induced strain due to P is expected to enhance P activation under compressive stress. The B diffusion model in SiGe we developed in Chapter 6 can be applied to other elements like P or As. Extending the model to a comprehensive KLMC model including dopant-defect formation kinetics would be of great interest because the annealing process usually stops before the system reaches equilibrium. We also suggest a more dedicated segregation experiment with particular attention given to the thickness of

the strained layer and lattice relaxation.

8.3 Final Conclusion

In this dissertation, we demonstrated how DFT calculations can be used to improve our understanding of complicated dopant/defect behavior in Si. DFT has become an essential tool in studying material properties and atomic behavior of dopants/defects in Si, and is making an important contribution to the development of silicon technology. Likewise, faster microprocessors in turn improve the predictive capability of DFT. Based on an optimistic outlook, advances in chip fabrication technology accompanied by the improvement of computing power may eventually lead to fully atomic-scale simulations of devices.

BIBLIOGRAPHY

[1] J. Foggiato and W. Yoo, Mater. Sci. Engineering. B **124**, 219 (2005).

[2] J. S. Christensen, H. H. Radamson, A. Y. Kuznetsov, and B. G. Svensson, J. Appl. Phys. **94**, 6533 (2005).

[3] A. N. Larsen, N. Zangenberg, and J. Fage-Pedersen, Mater. Sci. Eng. B **124-125**, 241 (2005).

[4] S. Solmi, A. Parisini, R. Angelucci, A. Armigliato, D. Nobili, and L. Moro, Phys. Rev. B **53**, 7836 (1996).

[5] M. Derdour, D. Nobili, and S. Solmi, J. Electrochem. Soc. **138**, 857 (1991).

[6] H. Stohr and W. Klemm, Z. anorg. allgem. Chem. **241**, 313 (1939).

[7] E. R. Johnson and S. M. Christian, Phys. Rev. **95**, 560 (1954).

[8] J. Dismukes, L. Ekstrom, and R. Pfaff, J. Phys. Chem. **68**, 3021 (1964).

[9] N. Moriya, L. C. Feldman, H. S. Luftman, C. A. King, J. Bevk, and B. Freer, Phys. Rev. Lett. **71**, 883 (1993).

[10] T. T. Fang, W. T. C. Fang, P. B. Griffin, and J. D. Plummer, Appl. Phys. Lett. **68**, 791 (1996).

[11] X. Liu, W. Windl, K. M. Beardmore, and M. P. Masquelier, Appl. Phys. Lett. **82** (2004).

[12] M. Diebel, Ph.D. thesis, University of Washington, Seattle, U.S.A. (2004).

[13] *International Technology Roadmap of Semiconductors*, SEMATECH (2006), URL `http://www.itrs.net/`.

[14] J. Hafner, C. Wolverton, and G. Ceder, MRS Bulletin **31**, 659 (2006).

[15] P. E. Blöchl, Phys. Rev. B **50**, 17953 (1994).

[16] O. K. Andersen, Phys. Rev. B **12**, 3060 (1975).

[17] A. Ural, P. B. Griffin, and J. D. Plummer, Phys. Rev. Lett. **83**, 3454 (1999).

[18] G. S. Cargill III, J. Angilello, and K. L. Kavanagh, Phys. Rev. Lett. **61**, 1748 (1988).

[19] A. Fukuhara and Y. Takano, Acta Cryst. A **33**, 137 (1977).

[20] M. R. Sardela, H. H. Radamson, J. O. Ekberg, J.-E. Sundgren, and G. V. Hansson, Semicond. Sci. Technol. **9**, 1272 (1994).

[21] N. Marzari, MRS Bulletin **31**, 681 (2006).

[22] H. Ikehata, N. Nagasako, S. Kuramoto, and T. Saito, MRS Bulletin **31**, 688 (2006).

[23] M. Sugihara, V. Buss, P. Entel, and J. Hafner, J. Phys. Chem. B **108**, 3673 (2004).

[24] J. P. Brodholt and L. Vocadlo, MRS Bulletin **31**, 675 (2006).

[25] P. Kuo, J. L. Hoyt, J. F. Gibbons, J. E. Turner, R. D. Jacowitz, and T. I. Kamins, Appl. Phys. Lett. **62**, 612 (1993).

[26] N. E. B. Cowern, P. C. Zalm, P. van der Sluis, D. J. Gravesteijn, and W. B. de Boer, Phys. Rev. Lett. **72**, 2585 (1994).

[27] M. J. Aziz, Appl. Phys. Lett. **70**, 2810 (1997).

[28] Y. Zhao, M. J. Aziz, H.-J. Gossmann, S. Mitha, and D. Schiferl, Appl. Phys. Lett. **75**, 941 (1999).

[29] Y. Zhao, M. J. Aziz, H.-J. Gossmann, S. Mitha, and D. Schiferl, Appl. Physics Lett. **74**, 31 (1999).

[30] M. J. Aziz, Materials Science in Semiconductor Processing **4**, 397 (2001).

[31] B. Sadigh, T. J. Lenosky, M.-J. Caturla, A. A. Quong, L. X. Benedict, T. Diaz de la Rubia, M. M. Giles, M. Foad, C. D. Spataru, and S. G. Louie, Appl. Phys. Lett. **80**, 4738 (2002).

[32] N. R. Zangenberg, J. Fage-Pedersen, J. Lundsgaard Hansen, and A. Nylandsted Larsen, J. Appl. Phys. **94**, 3883 (2003).

[33] H. Jónsson, G. Mills, and K. W. Jacobsen, *Classical and Quantum Dynamics in Condensed Phase Simulations* (World Scientific, Singapore, 1998), p. 385.

[34] G. Henkelman and H. Jónsson, J. Chem. Phys. **111**, 7010 (1999).

[35] G. Henkelman and H. Jónsson, J. Chem. Phys. **113**, 9978 (2000).

[36] G. Henkelman, B. P. Uberuaga, and H. Jónsson, J. Chem. Phys. **113**, 9901 (2000).

[37] *TCAD Sentaurus*, Synopsys (2006), URL `http://www.synopsys.com/`.

[38] S. E. Thompson *et al.*, IEEE Trans. Electron Devices **51**, 1790 (2004).

[39] C. Ahn, J. Song, and S. T. Dunham, Mater. Res. Soc. Symp. Proc. **913**, 179 (2006).

[40] C. Ahn and S. T. Dunham, J. Vac. Sci. Technol. B **24**, 700 (2006).

[41] E. Ganin, B. Davari, D. Harame, G. Scilla, and G. A. Sai-Halasz, Appl. Phys. Lett. **54**, 2127 (1989).

[42] S. Kwon, H. Kim, and J. Lee, Jap. J. Appl. Phys. **29**, L2326 (1990).

[43] S. Solmi, J. Appl. Phys. **83**, 1742 (1998).

[44] L. Yang, J. R. Watling, R. C. W. Wilkins, M. Borici, J. R. Barker, A. Asenov, and S. Roy, Semicond. Sci. Technol. **19**, 1174 (2004).

[45] P. Kuo, J. L. Hoyt, J. F. Gibbons, J. E. Turner, and D. Lefforge, Appl. Phys. Lett. **66**, 580 (1995).

[46] R. F. Lever, J. M. Bonar, and A. F. W. Willoughby, J. Appl. Phys. **83**, 1988 (1998).

[47] J. Hattendorf, W.-D. Zeitz, W. Schröder, and N. Abrosimov, Physica B **340-342**, 858 (2003).

[48] W. Kohn and L. J. Sham, Phys. Rev. **140**, A1133 (1965).

[49] J. P. Perdew and W. Yue, Phys. Rev. B **33**, 8800 (1986).

[50] J. P. Perdew, K. Burke, and M. Ernzerhof, Phys. Rev. Lett. **77**, 3865 (1996).

[51] J. P. Perdew, J. A. Chevary, S. H. Vosko, K. A. Jackson, M. R. Pederson, D. J. Singh, and C. Fiolhais, Phys. Rev. B **46**, 6671 (1992).

[52] C. Lee, W. Yang, and R. G. Parr, Phys. Rev. B **37**, 785 (1988).

[53] A. D. Becke, Phys. Rev. A **38**, 3098 (1988).

[54] Gaussian NEWS **5**, 2 (1994).

[55] A. D. Becke, J. Chem. Phys. **98**, 1372 (1993).

[56] C. Adamo and V. Barone, J. Chem. Phys. **110**, 6158 (1999).

[57] J. P. Perdew and A. Zunger, Phys. Rev. B **23**, 5048 (1981).

[58] G. Kresse and J. Hafner, Phys. Rev. B **47**, 558 (1993).

[59] G. Kresse and J. Furthmüller, Phys. Rev. B **54**, 11169 (1996).

[60] *VASP the GUIDE*, Institut für Materialphysik. Universität Wien (2001), URL `http://cms.mpi.univie.ac.at/vasp/`.

[61] R. P. Feynman, Phys. Rev. **56**, 340 (1939).

[62] B. M. DEB, Rev. Mod. Phys. **45**, 22 (1973).

[63] A. Baldereschi, Phys. Rev. B **7**, 5212 (1973).

[64] D. J. Chadi and M. L. Cohen, Phys. Rev. B **8**, 5747 (1973).

[65] H. J. Monkhorst and J. D. Pack, Phys. Rev. B **13**, 5188 (1976).

[66] J. Lento, J.-L. Mozos, and R. Nieminen, J. Phys.: Condensed Matter **14**, 2637 (2002).

[67] R. Godby and M. Schlüter, Phys. Rev. Lett. **56**, 2415 (1986).

[68] P. M. Fahey, P. B. Griffin, and J. D. Plummer, Rev. Mod. Phys. **61**, 289 (1989).

[69] A. Ural, P. B. Griffin, and J. D. Plummer, J. Appl. Phys. **85**, 6440 (1999).

[70] O. Sugino and A. Oshiyama, Phys. Rev. B **46**, 12335 (1992).

[71] K. C. Pandey, A. Erbil, G. S. Cargill, R. F. Boehme, and D. Vanderbilt, Phys. Rev. Lett. **61**, 1282 (1988).

[72] M. A. Berding, A. Sher, and M. van Schilfgaarde, Appl. Phys. Lett. **72**, 1492 (1998).

[73] D. W. Lawther, U. Myler, P. J. Simpson, P. M. Rousseau, P. B. Griffin, and J. Plummer, Appl. Phys. Lett. **67**, 3575 (1995).

[74] J. Xie and S. P. Chen, J. Phys. D **32**, 1252 (1999).

[75] E. Nygren, M. J. Aziz, D. Turnbull, J. M. Poate, D. C. Jacobson, and R. Hull, Appl. Phys. Lett. **47**, 105 (1982).

[76] N. Sugii, S. Irieda, J. Morioka, and T. Inada, J. Appl. Phys. **96**, 261 (2004).

[77] S. Uppal, J. Z. J. M. Bonar, and A. F. W. Willoughby, Mater. Sci. Engineering **114**, 349 (2004).

[78] P. Laitinen, I. Riihimäki, and J. Räisänen, Phys. Rev. B **68**, 155209 (2003).

[79] J. Slotte, S.-L. Sihto, J. Lento, E. Monakhov, A. Kuznetsov, K. Saarinen, and G. Svensson, Physica B **340-342**, 849 (2003).

[80] A. N. Larsen, P. Kringhøj, J. L. Hansen, and S. Y. Shiryaev, J. Appl. Phys. **81**, 2173 (1997).

[81] P. Fahey, S. S. Iyer, and G. J. Scilla, Appl. Phys. Lett. **54**, 843 (1988).

[82] P. Griffin, M. Cao, P. Vande Voorde, Y.-L. Chan, and W. Greene, Appl. Phys. Lett. **73**, 2986 (1998).

[83] C. Melis, G. M. Lopez, and V. Fiorentini, Appl. Phys. Lett. **85**, 4902 (2004).

[84] P. Alippi, A. L. Magna, S. Scalese, and V. Privitera, Phys. Rev. B **69**, 085213 (2004).

[85] E. R. Batista, J. H. Richard, G. Hennig, B. P. Uberuaga, R. L. M. amd G. E. Scuseria, C. J. Umrigar, and J. W. Wilkins, Phys. Rev. B **74**, 121102 (2006).

[86] V. Ranki, J. Nissilä, and K. Saarinen, Phys. Rev. Lett. **88**, 105506 (2002).

[87] A. Erbil, W. Weber, G. S. Cargill III, and R. F. Boehme, Phys. Rev. B **34**, R1392 (1986).

[88] V. Koteski, N. Ivanovic, H. Haas, E. Holub-Krappe, and H.-E. Mahnke, Nucl. Instr. and Meth. in Phys. Res. B **200**, 60 (2003).

[89] A. Parisini, A. Bourret, A. Armigliato, M. Servidori, S. Solmi, R. Fabbri, J. R. Regnard, and J. L. Allain, J. Appl. Phys. **87**, 2320 (1990).

[90] A. Herrera-Gomez, P. M. Rousseau, J. C. Woicik, T. Kendelewicz, J. Plummer, and W. E. Spicer, J. Appl. Phys. **85**, 1429 (1999).

[91] S. Wei, H. Oyanagi, H. Kawanami, K. Sakamoto, T. Sakamoto, K. Tamura, N. L. Saini, and K. Uosaki, J. Appl. Phys. **82**, 4810 (1997).

[92] H. Li, T. Kirichenko, P. Kohli, S. Banerjee, R. Tichy, and P. Zeitzoff, IEEE Elec. Dev. Lett. **23**, 646 (2002).

[93] S. Solmi, S. Valmorri, and R. Canteri, J. Appl. Phys. **77**, 2400 (1995).

[94] C. Revenant-Brizard, J. R. Regnard, S. Solmi, A. Armigliato, S. Valmorri, C. Cellini, and F. Romanato, J. Appl. Phys. **79**, 9037 (1996).

[95] N. E. B. Cowern, Appl. Phys. Lett. **54**, 703 (1989).

[96] S. Scalese, M. I. S. Grasso, V. Privitera, J. S. Christensen, and G. G. Svensson, J. Appl. Phys. **99**, 113516 (2006).

[97] D. Vanderbilt, Phys. Rev. B **41**, 7892 (1990).

[98] D. K. Sadana, A. Acovic, B. Davari, D. Grutzmacher, H. Hanafi, and F. Cardone, Appl. Phys. Lett. **61**, 3038 (1992).

[99] K. Yokota, M. Ochi, T. Hirao, Y. Ando, and K. Matsuda, J. Appl. Phys. **69**, 2975 (1991).

[100] M. Rudan and G. Perroni, Semicond. Sci. Technol. **19**, S82 (2004).

[101] E. Atoro, Y. Ohama, and Y. Hayafuji, Appl. Phys. Lett. **83**, 3051 (2003).

[102] S. Solmi, A. Parisini, M. Bersani, D. Giubertoni, V. Soncini, G. Garnevale, A. Benvenuti, and A. Marmiroli, J. Appl. Phys. **92**, 1361 (2002).

[103] F. Szmulowicz, J. Wendeln, and S. Slaton, J. Appl. Phys. **55**, 2945 (1984).

[104] L. Wang, P. Clancy, and C. S. Murthy, Phys. Rev. B **70**, 165206 (2004).

[105] W. Windl, M. M. Bunea, R. Stumpf, S. T. Dunham, and M. P. Masquelier, Phys. Rev. Lett. **83** (1999).

[106] S. Lee, J. Kang, and M. Kang, J. Korean Phys. Soc. **31**, 811 (1997).

[107] S. M. Hu, Phys. Rev. Lett. **63**, 2492 (1989).

[108] S. M. Hu, D. C. Ahlgren, P. A. Ronsheim, and J. Chu, Phys. Rev. Lett. **67**, 1450 (1991).

[109] S. M. Hu, Phys. Rev. B **45**, 4498 (1992).

[110] N. Moriya, L. C. Feldman, S. W. Downey, C. A. King, and A. B. Emerson, Phys. Rev. Lett. **75**, 1981 (1995).

[111] S. Kobayashi, M. Iizuka, T. Aoki, and N. Mikoshiba, J. Appl. Phys. **86**, 5480 (1999).

[112] M. V. Fischetti and S. E. Laux, J. Appl. Phys. **80**, 2234 (1996).

[113] M. A. Green, J. Appl. Phys. **67**, 2944 (1990).

[114] C.G. Van de Walle and R. M. Martin, Phys. Rev. B **34**, 5621 (1986).

[115] J. D. Wiley, Sold State Commun. **8**, 1865 (1970).

[116] Y. Fu, S. C. Jain, M. Willander, and J. J. Loferski, J. Appl. Phys. **74**, 402 (1993).

[117] Y. Okada and Y. Tokumaru, J. Appl. Phys. **56**, 314 (1984).

[118] F. Schäffler, *Properties of Advanced Semiconductor Materials GaN, AlN, InN, BN, SiC, SiGe* (John Wiley & Sons, Inc., New York, 2001), pp. 149–188.

[119] S. Nikanorov, Y. Burenkov, and A. Stepanov, Soviet Physics-Solid state **13**, 2516 (1971).

[120] M. E. Kurdi, S. Sauvage, G. Fishman, and P. Boucaud, Phys. Rev. B **73**, 195327 (2006).

[121] W. X. Ni, J. Knall, and G. V. Hansson, Phys. Rev. B **36**, 7744 (1987).

[122] T. Baier, U. Mantz, K. Thonke, R. Sauer, F. Schäffler, and H.-J. Herzog, Phys. Rev. B **50**, 15191 (1994).

[123] M. L. W. Thewalt, D. A. Harrison, C. F. Reinhart, J. A. Wolk, and H. Lafontaine, Phys. Rev. Lett. **79**, 269 (1997).

[124] C. Penn, F. Schäffler, G. Bauer, and S. Glutsch, Phys. Rev. B **59**, 13314 (1999).

[125] H. H. Cheng, S. T. Yen, and R. J. Nicholas, Phys. Rev. B **62**, 4638 (2000).

[126] R. Arghavani, N. Derhacobian, V. Banthia, M. Balseanu, N. Ingle, H. M'Saad, S. Venkataraman, E. Yieh, Z. Yuan, L.-O. Xia, et al., IEEE Trans. Electron Devices, **54**, 362 (2007).

Appendix A

DEVELOPMENT HISTORY OF DFT POTENTIALS

Although the Hohenberg-Kohn and Kohn-Sham theories were published in 1964 and 1965, respectively, there had been earlier attempts to make the exchange energy term local. The first attempt was made in Slater's paper: "*A Simplification of the Hartree-Fock Method.*" (Phys. Rev. **81**, 385 (1950)). Even in the 1920's, Thomas and Fermi described the energy of homogeneous electron systems using the local kinetic energy functional. Those early attempts were not very successful and DFT became useful only after LDA was available in 1970's. LDA provides qualitatively correct descriptions, however, it still lacks accuracy in describing the energetics of chemical reactions. The accuracy is much improved in GGA, developed in 1980's, but it is still far from the chemists' goal (1 kcal/mol$\approx$43.4 meV/atom). Therefore, more sophisticated functionals (e.g., meta-GGA and hybrid functionals) have been developed to achieve the goal (see Fig. 2.2). Table A.1 provides the development history of these functionals.

Table A.1: The development history of DFT functionals. The most common names in the literature are used and popular functionals are written in *italics*. This table was made by Mark E. Casida, and is presented with the author's permission.

Name	Year	Reference	Comments
Exchange-correlation functionals, E_{xc}			
CAM-B3LYP	2004	T.Yanai *et al.*, Chem. Phys. Lett. **393, 51**	xc, hybrid, "Coulomb attenuated method":short range DFT + long range HF
TPSSh	2003	V. Staroverov *et al.*, J. Chem. Phys. **119**, 12129	xc, meta-GGA-hybrid
TPSS	2003	J. Tao *et al.*, Phys. Rev. Lett. **91**, 146401	xc, meta-GGA , *ab-initio*
mPBE	2002	C. Adamo *et al.*, J. Chem. Phys. **116**, 5933	xc
OPTX	2001	N. Handy *et al.*, Mol. Phys. **99**, 403	x, GGA
LC	2001	H. Iikura *et al.*, J. Chem. Phys. **115**, 3540	xc , "Long range correction": short range DFT + long range HF
PCS00	2000	E. Proynov *et al.*, J. Chem. Phys. **113**, 10013	xc, meta-GGA
B00	2000	A. Becke, J. Chem. Phys. **112**, 4020	xc, meta-GGA
PBE0	1999	C. Adamo *et al.*, J. Chem. Phys. **110**, 6158	xc, hybrid, more or less *ab-initio*
PKZB	1999	J. Perdew *et al.*, Phys. Rev. Lett. **82**, 2544	meta-GGA
SAOP	1999	O. Gritsenko *et al.*, Chem. Phys. Lett. **302**, 199	xc, OEP-like GGA, orbital-dependent
tauPBE	1999	M. Ernzerhof *et al.*, J. Chem. Phys. **111**, 911	xc, meta-GGA, based on PBE GGA

Continued on next page

Table A.1 – continued from previous page

Name	Year	Reference	Comments
RPBE	1999	B. Hammer *et al.*, Phys. Rev. B **59**, 7413	xc, GGA, based on PBE GGA
EDF1	1998	R. Adamson *et al.*, Chem. Phys. Lett. **284**, 6	xc, GGA, semiempirical basis-set dependent fit to G2 data
mPW1, 3PW	1998	C. Adamo *et al.*, J. Chem. Phys. **108**, 664	
ZY98	1998	Y. Zhang *et al.*, J. Chem. Phys. **109**, 2604	not a new functional, but points out a problem with the old ones.
VSXC	1998	T. Voorhis *et al.*, J. Chem. Phys. **109**, 400	xc, meta-GGA
SB98b	1998	H. Schmider *et al.*, J. Chem. Phys. **109**, 8188	
SB98a	1998	H. Schmider *et al.*, J. Chem. Phys. **108**, 9624	
B98	1998	A. Becke, J. Chem. Phys. **109**, 2092	
HCTH	1998	H. Hamprecht *et al.*, J. Chem. Phys. **109**, 6264	xc, GGA, semiempirical
GCRA98	1998	O. Gritsenko *et. al.*, Chem. Phys. Lett. **296**, 307	WDA + gradient correction
revPBE	1998	Y. Zhang *et. al.*, Phys. Rev. Lett. **80**, 890	xc, GGA, a modification of PBE that has been used successfully with surface calculations
K2-BVWN	1998	S. Kafafi, J. Phys. Chem. A **102**, 10404	xc, hybrid, interesting results, but unclear (or incorrect)
HFS-BVWN	1998	S. Kafafi *et al.*, J. Phys. Chem. A **102**, 3202	
FT98	1998	M. Filatov *et al.*, Phys. Rev. A **57**, 189	
FT97	1997	M. Filatov *et al.*, Mol. Phys. **91**, 847	

Continued on next page

Table A.1 – continued from previous page

Name	Year	Reference	Comments
B97	1997	A. Becke, J. Chem. Phys. **107**, 8554	
PBE	1996	J. Perdew *et. al*, Phys. Rev. Lett. **77**, 3865	xc, GGA, constructed nonempirically, exact for the uniform electron gas and very useful for solids.
ACM	1995	J. Baker *et al.*, J. Chem. Phys. **102**, 2063	
LAP	1995	E. Proynov *et al.*, Phys. Lett. **230**, 419	c, meta-GGA, includes the Laplacian of the charge density
PVS	1994	E. Proynov *et al.*, Phys. Rev. B **49** 7874	c, local
B3LYP	1994	Gaussian Inc., Gaussian NEWS, **5**, 2	xc, hybrid
B3P	1993	A. Becke, J. Chem. Phys. **98**, 5648	xc, hybrid
1/2&1/2	1993	A. Becke, J. Chem. Phys. **98**, 1372	xc, hybrid, the original hybrid functional
PW91	1991	J. Perdew *et al.*, Phys. Rev. B **46**, 6671	xc, GGA, constructed nonempirically, exact for the uniform gas, and very useful for solids. Note that this GGA is very unusual in that it was widely incorporated in many DFT programs significantly before any report appeared in the literature.
WL90	1990	L.Wilson *et al.*, Phys. Rev. B **41**, 12930	c, GGA, simple GGA satisfying certain coordinate scaling requirements.
BR89	1989	A. Becke *et al.*, Phys. Rev. A **39**, 3761	xc, meta-GGA
LYP	1988	C. Lee *et al.*, Phys. Rev. B **37**, 785	x, GGA, used in the B3LYP hybrid

Continued on next page

Table A.1 – continued from previous page

Name	Year	Reference	Comments
B	1988	A. Becke, Phys. Rev. A **38**, 3098	x, GGA, asymptotically correct energy density
DK87	1987	A. DePristo *et al.*, J. Chem. Phys. **86**, 1425	
PW86	1986	J. Perdew *et al.*, Phys. Rev. B **33**, 8800	x,GGA
LM83	1983	D. Langreth *et al.*, Phys. Rev. B **28**, 1809	c,GGA, essentially the first GGA
SIC	1981	J. Perdew*et al.*, Phys. Rev. B **23**, 5048	xc, SIC, the most popular self-interaction correction containing an important parameterization of the LDA
LP80	1980	D. Langreth *et al.*, Phys. Rev. B **21**, 5469	GGA, critical seminal paper for GGAs
SMW80i	1980	C. Shih *et al.*, J. Chem. Phys. **73**, 1340	Xalpha, beta , semiempirical
LDA	1965	W. Kohn *et al.*, Phys. Rev. **140**, A1133	xc, local
DFT	1964	P. Hohenberg *et al.*, Phys. Rev. **136**, B864	the founding formal paper of modern density-functional theory
Xalpha	1974	J. Slater, *The Self-Consistent Field for Molecules and Solids*, McGraw-Hill, New York, x, local, an LDA-like functional	
Model exchange-correlation potentials, v_{xc}			
GRAC	2001	M. Grüning *et al.*, J. Chem. Phys. **114**, 652	xc, model xc potential
AC	1998	M. Casida *et al.*, J. Quant. Chem. **70**, 933	xc, GGA, asymptotically corrected potential
LRC95	1995	A. Lembarki *et al.*, Phys. Rev. A **52**, 3704	xc, GGA, asymptotically corrected potential
LB94	1994	R. van Leeuwen *et al.*, Phys. Rev. A **49**, 2421	xc, GGA, asymptotically corrected potential

Continued on next page

Table A.1 – continued from previous page

Name	Year	Reference	Comments
KLI	1990	J. Krieger *et al.*, Phys. Lett. A **146**, 256	x, rung 4 (see Fig. 2.2)
ALT81	1981	K. Aashamar *et al.*, Molec. Phys. **14**, 803	xc, OEP from MCSCF
ALT79	1979	K. Aashamar *et al.*, Molec. Phys. **12**, 3455	xc, OEP from MCSCF
PT78b	1978	M. Pant *et al.*, Phys. Lett. A **68**, 154	x, OEPx
PT78b	1978	M. Pant *et al.*, Phys. Rev. A **17**, 1819	x, OEPx
TS76	1976	J. Talman *et al.*, Phys. Rev. A **14**, 36	x, The first computations of the OEP (exchange-only)
SH55	1955	R. Sharp *et al.*, Phys. Rev. **90**, 317	x, the first formulation of the optimized effective potential (OEP)
S50	1950	J. Slater, Phys. Rev. **81**, 385	x, the first concept of a localized exchange potential
Kinetic energy functionals, T_s			
WGC99	1999	Y. Wang *et al.*, Phys. Rev. B **60**, 16350	
W97	1997	T. Wesolowski *et al.*, J. Chem. Phys. **106**, 8516	GGA
W	1935	C. Weizsäcker *et al.*, Z. Phys. **96**, 451	gradient-correction, the first gradient-corrected T_s
TF	1927	L. Thomas, Proc. Cambridge Philos. Soc. **23**, 542; E. Fermi, Rend. Accad, Lincei **6**, 602	LDA, the first kinetic energy functional

Appendix B

INTERSTITIAL STRUCTURES IN Si LATTICE

There are various high symmetry interstitial structures in the silicon lattice and they play an important role in atomic transitions. Usually, a dopant/defect migrates from a high symmetry position to another, and it often corresponds to extrema in the energy surface. A typical example is the GaI transition: Ge_i^{tet} (Fig. B.5) is the minimum energy structure and $GaI_{<110>}$ split (Fig. B.1) is the transition state. Thus, in the study of dopant diffusion using *ab-initio* method, the first step is finding the formation energy of these structures. Here we present simple dopant-defect pair structures.

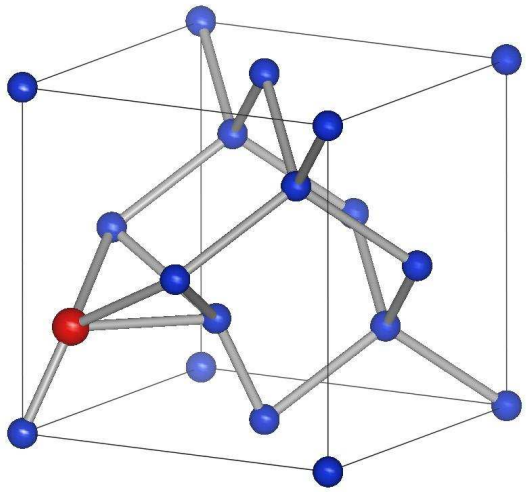

Figure B.1: [110] split structure. Si (self-interstitial) and As have the minimum energy at this position.

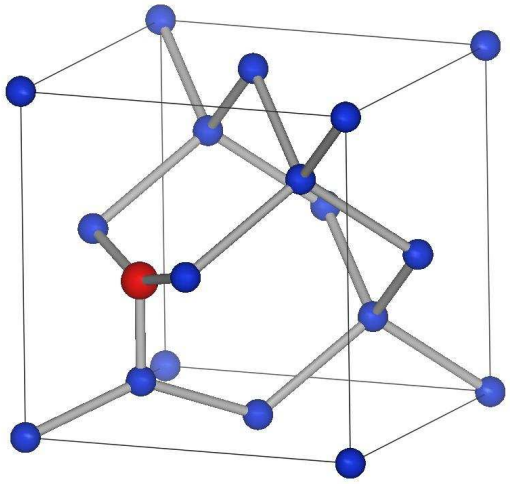

Figure B.2: [001] split structure. It is the minimum energy structure for C.

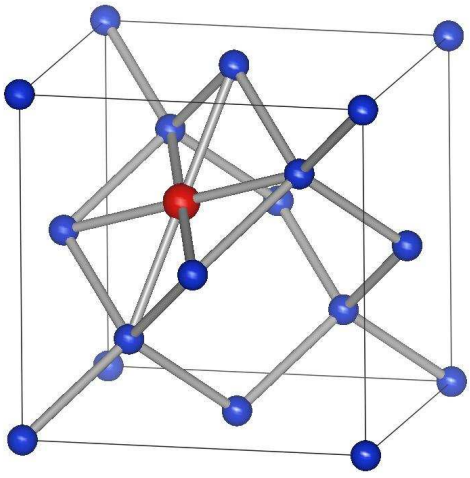

Figure B.3: A^{hex} structure. The interstitial atom is at the center of a hexagonal ring. It is the minimum energy state for P^+ [11], the transition state for As (see Chapter 3), and the meta-stable state for B transition.

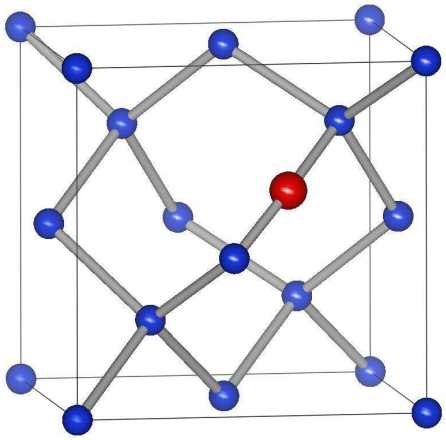

Figure B.4: Bond-centered structure. It is the minimum energy state for F^+ [12].

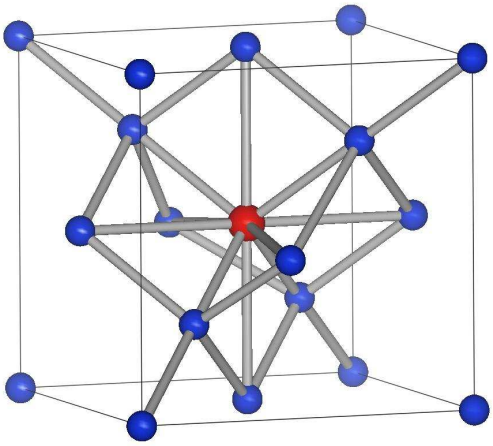

Figure B.5: A_i^{tet} structure. A dopant atom is at the most open and symmetric position in the lattice. It is the minimum energy state for Ga (see Chapter 3).

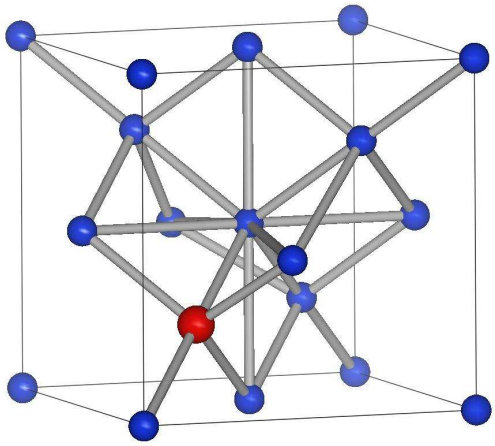

Figure B.6: AI^{tet} structure. Unlike the A_i^{tet}, the dopant atom is at a substitutional site and a Si atom is at one of the four nearby tetrahedral sites. It is the minimum energy state for B (see Chapter 1) and In (see Chapter 3).

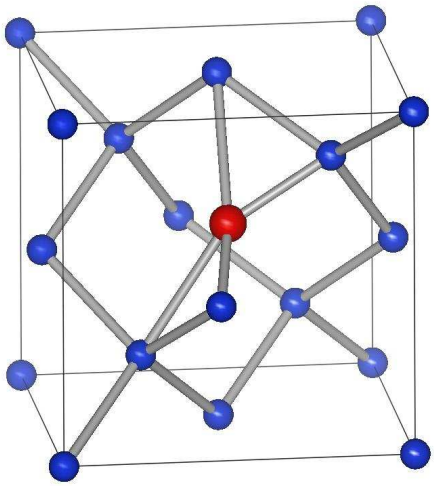

Figure B.7: X_2 structure. The PI formation energy is the lowest at this structure (see Chapter 3).

Appendix C

KLMC CODE FOR PI DIFFUSION

In Chaper 3, we performed KLMC simulations for P, Ga, and In diffusion. Here we provide the C code used for P diffusion.

```
#include <stdlib.h>
#include <time.h>
#include <math.h>
#include <stdio.h>

const T=1173; /*temperature */
double k=8.617385e-5, V=2.03e-29, J2eV=1.6e-19; /*physical constants and a lattice volume */
double C11=156e9, C12=55e9; /*Elastic stiffness tensor. DFT values */
double BC ;/*C11+(1-2*C12/C11)*C12, C matrix part under biaxial stress*/
double ISin=-0.05, ISout=0.96; /*Induced strain intra-ring transition*/
double ISsub=-0.08; /*Induced strain of substitutional P*/
double ISpi=0.36; /*Induced strain of PI (ISpi, ISpi, 0) */
double ISHin=0.272, ISHout=0.251; /*Induced strain inter-ring transition */
double MB1=0.2, MB2=0.1; /*Migration barrier */
const Step=20000, Sample=20000; /*Number of samples and steps */

//determine sign of input.
int sign(int n)
{
return n >0?1:(n<0?-1:0);
}

main()
{
  int i,j,k; /* dummy index */
  int rd_int;
  int RA, RB, RH1; /*probability of a hop to each direction */
  int A[3], B[3], H[3]; /* three lattice sites determining an interstitial position */
  int Abuff[3], Bbuff[3], Hbuff1[3], Hbuff2[3]; /* all possible hopping positions */
  int DA[3], DB[3], DH1[3], DH2[3]; /*displacement between the original position and the new available position. */
  int HA[3], HB[3], HAB[3]; /*displacement between H and A/B/(A+B/2) */
```

```
  float PI[3], PF[3]; /*initial and final interstitial positions */
  double x[i]; /*applied strain */
  double GA, GB, GH1, GH2, GT; /*transition rate of a hop to each direction*/
  double TT; /*total time for one sample */
  double sumTT[9], sumDxx[9], sumDyy[9], sumDzz[9] ; /*grand total of time and displacement */
  double avTT[9], avDxx[9], avDyy[9], avDzz[9]; /*average of time and displacement */
  double eA[3], eB[3], eH1[3], eH2[3]; /*induced strain vectors of transition states */
  double ePI[3]; /*induced strain vector of a interstitial state */
  double Cin[9], Cout[9], Ctotal[9]; /*interstitial concentrations */
  double din[9], dout[9], Din[9], Dout[9]; /*microscopic and macroscopic diffusivities */

  printf("# Temperature : %f C \ n",T-273. );
  BC=C11+(1-2*C12/C11)*C12;
  for(i=0; i < 9 ; i++){
// Applied strain.
    x[i]=0.0025*(i-4);
// Initialize values.
    sumTT[i]=0.0; avTT[i]=0.0;
    sumDxx[i]=0.0; sumDyY[I]=0.0; sumDzz[i]=0.0;
    avDxx[i]=0.0; avDyy[i]=0.0; avDzz[i]=0.0;
    for(j=0; j < Sample; j++){
//Initialize PI position, it is uniquely determined by three lattice sites (A, B and a nearby hex).
      A[0]=2;A[1]=2;A[2]=2;
      B[0]=4;B[1]=0;B[2]=4;
      H[0]=3;H[1]=3;H[2]=5;
// Initial PI position it is like (A+B+H)/3.
    PI[0]=(A[0]+B[0]+H[0])/3.0; PI[1]=(A[1]+B[1]+H[1])/3.0; PI[2]=(A[2]+B[2]+H[2])/3.0;
// Initialization of Total time for a sample
      TT=0;
// 'Step' step random walk.
      for(k=0; k<Step; k++){
        HA[0]=H[0]-A[0]; HA[1]=H[1]-A[1]; HA[2]=H[2]-A[2];
        HB[0]=H[0]-B[0]; HB[1]=H[1]-B[1]; HB[2]=H[2]-B[2];
// Abuff (Bbuff) is the neighbor of B (A) in the hex-ring shared by A, B and H.
        Abuff[0]=sign(HA[0])*2+B[0];
        Abuff[1]=sign(HA[1])*2+B[1];
        Abuff[2]=sign(HA[2])*2+B[2];
        Bbuff[0]=sign(HB[0])*2+A[0];
        Bbuff[1]=sign(HB[1])*2+A[1];
        Bbuff[2]=sign(HB[2])*2+A[2];
// Displacement to two nearby hex sites sharing A-B sites.
        DH1[0]=-sign(HA[0])*fmod(abs(HA[0]),3)*2;
```

```
        DH1[1]=-sign(HA[1])*fmod(abs(HA[1]),3)*2;
        DH1[2]=-sign(HA[2])*fmod(abs(HA[2]),3)*2;
        DH2[0]=-sign(HB[0])*fmod(abs(HB[0]),3)*2;
        DH2[1]=-sign(HB[1])*fmod(abs(HB[1]),3)*2;
        DH2[2]=-sign(HB[2])*fmod(abs(HB[2]),3)*2;
// Displacement between A(B) and Abuff(Bbuff)
        DA[0]=A[0]-Abuff[0]; DA[1]=A[1]-Abuff[1]; DA[2]=A[2]-Abuff[2];
        DB[0]=B[0]-Bbuff[0]; DB[1]=B[1]-Bbuff[1]; DB[2]=B[2]-Bbuff[2];
//Determine induced strain of PI state.
// HAB is the direction vector to the hex site from the PI.
// If HAB[z]=0, in-plane. Otherwise, out-of-plane : 1/3 in-plane, 2/3 out-of-plane.
        HAB[0]=H[0]-(A[0]+B[0])/2;
        HAB[1]=H[1]-(A[1]+B[1])/2;
        HAB[2]=H[2]-(A[2]+B[2])/2;
        ePI[0]=HAB[0]==0?0:ISpi;
        ePI[1]=HAB[1]==0?0:ISpi;
        ePI[2]=HAB[2]==0?0:ISpi;
// Determine Induced strain of transition state for hopping
// Volume expansion is minimal along the moving direction and maximal to the normal
direction.
// ISout > ISin
// In-plane migration -> no Z variation -> induced strain (ISin, ISin, ISout)
        eA[0]=(DA[0]==0?ISout:ISin);
        eA[1]=(DA[1]==0?ISout:ISin);
        eA[2]=(DA[2]==0?ISout:ISin);
        eB[0]=(DB[0]==0?ISout:ISin);
        eB[1]=(DB[1]==0?ISout:ISin);
        eB[2]=(DB[2]==0?ISout:ISin);
        eH1[0]=(DH1[0]==0?ISHout:ISHin);
        eH1[1]=(DH1[1]==0?ISHout:ISHin);
        eH1[2]=(DH1[2]==0?ISHout:ISHin);
        eH2[0]=(DH2[0]==0?ISHout:ISHin);
        eH2[1]=(DH2[1]==0?ISHout:ISHin);
        eH2[2]=(DH2[2]==0?ISHout:ISHin);
// Transition rate
        GA=exp((V*(eA[0]+eA[1]-ePI[0]-ePI[1])*BC*x[i]/J2eV+MB1)/k /T);
        GB=exp((V*(eB[0]+eB[1]-ePI[0]-ePI[1])*BC*x[i]/J2eV+MB1)/k /T);
        GH1=exp((V*(eH1[0]+eH1[1]-ePI[0]-ePI[1])*BC*x[i]/J2eV+MB2) /k/T);
        GH2=exp((V*(eH2[0]+eH2[1]-ePI[0]-ePI[1])*BC*x[i]/J2eV+MB2) /k/T);
// Total transition rate at a given site for the 4 possible transitions.
        GT=GA+GB+GH1+GH2;
// Total time.
        TT=TT+1/GT;
// random number generation and probability for given transition.
```

```
        rd_int = rand();
        RA= floor(GA*RAND_MAX/GT);
        RB= floor((GA+GB)*RAND_MAX/GT);
        RH1= floor((GA+GB+GH1)*RAND_MAX/GT);
// Choose one hop direction out of 4 and update the position.
        if (rd_int < RA){
         A[0]=Abuff[0]; A[1]=Abuff[1]; A[2]=Abuff[2];}
        else if (rd_int < RB){
         B[0]=Bbuff[0]; B[1]=Bbuff[1]; B[2]=Bbuff[2];}
        else if (rd_int < RH1){
         H[0]=DH1[0]+H[0]; H[1]=DH1[1]+H[1]; H[2]=DH1[2]+H[2];}
        else {
         H[0]=DH2[0]+H[0]; H[1]=DH2[1]+H[1]; H[2]=DH2[2]+H[2];};
        };
// Final PI position.
      PF[0]=(A[0]+B[0]+H[0])/3.0;
      PF[1]=(A[1]+B[1]+H[1])/3.0;
      PF[2]=(A[2]+B[2]+H[2])/3.0;
// Grand total displacement and time of P atom for 'Sample' samples.
      sumDxx[i]=sumDxx[i]+(PI[0]-PF[0])*(PI[0]-PF[0]);
      sumDyy[i]=sumDyy[i]+(PI[1]-PF[1])*(PI[1]-PF[1]);
      sumDzz[i]=sumDzz[i]+(PI[2]-PF[2])*(PI[2]-PF[2]);
      sumTT[i]=sumTT[i]+TT;
      }
// Average value per sample.
    avDxx[i]=sumDxx[i]/Sample;
    avDyy[i]=sumDyy[i]/Sample;
    avDzz[i]=sumDzz[i]/Sample;
    avTT[i]=sumTT[i]/Sample;
    Cin[i]=exp(V*(2*ISpi-2*ISsub)*BC*x[i]/J2eV/(k*T));
    Cout[i]=exp(V*(ISpi-2*ISsub)*BC*x[i]/J2eV/(k*T));
    Ctotal[i]=Cin[i]/3.+Cout[i]*2/3.;
    din[i]=avDxx[i]/avTT[i];
    dout[i]=avDzz[i]/avTT[i];
    Din[i]=din[i]*Ctotal[i];
    Dout[i]=dout[i]*Ctotal[i];
    }
// Print normalized diffusivity and concentration.
  printf("strain din dout Din Dout Cin Cout Ctotal \ n");
  for (i=0; i<9; i++){
   printf("%f %f %f %f %f %f %f %f \ n", x[i], din[i]/din[5], dout[i]/dout[5], Din[i]/Din[5],
Dout[i]/Dout[0], Cin[i], Cout[i], Ctotal[i]);
  }
}
```

VITA

Ph.D. Physics and Nanotechnology, University of Washington, Seattle, WA (2007).

M.S. Physics, University of Washington, Seattle, WA (2003).

B.S. Physics, Korea University, Seoul, Korea (1996).